

Dissertation
submitted to the
Combined Faculty of Natural Sciences and Mathematics
of the Ruperto Carola University Heidelberg, Germany
for the degree of
Doctor of Natural Sciences

Presented by

M. Sc. Nils Kurzawa

born in Munich

Oral examination: June 7th, 2021

Computational methods for thermal stability proteomics

Referees: Dr. Wolfgang Huber
Prof. Dr. Benedikt Brors

To my parents

Abstract

In the last decades, molecular biology has transformed into a data-rich discipline. This trend is driven by developments in imaging and the continuous increase in available omics technologies which allow for high-throughput profiling of various types of molecules in a given biological system.

Classical omics approaches profile the abundance of thousands of cellular biomolecules, e.g., RNAs or proteins. Recently developed assays, such as Thermal Proteome Profiling (TPP), however, can additionally inform on biophysical states of proteins. By choosing the right experimental design or through contextualization of TPP experiments they can reveal small molecule protein engagement, protein-protein interaction (PPI) dynamics or effects of post-translational modifications (PTM). However, while experimental designs, reproducibility, amenable organisms and throughput of the TPP assay are being advanced at a fast pace, computational methods for statistical analysis of obtained data are lagging behind.

This thesis proposes a suite of computational methods to provide tools for several of the aforementioned application areas of TPP.

First, it describes a software package for analysis of TPP experiments in the context of PPIs and suggests a method for detection of differential PPIs across conditions. The application of this method to different TPP datasets revealed significantly changing PPIs during different phases of the human cell cycle and behavior of protein complexes in *Escherichia coli* within and across cellular compartments.

Second, this work addresses a specific experimental TPP setup called 2D-TPP in which

thermal stability of proteins is measured as a function of temperature and concentration of a compound of interest to find proteome-wide interactions of the compound. This was done by implementation of a curve-based hypothesis test to analyze data obtained from such experiments with false discovery rate control. The method was benchmarked on simulated data and on several real datasets. Application of the software to 2D-TPP datasets profiling epigenetic drugs revealed hitherto unknown off-targets and downstream effects of these drugs.

Third, the same computational method was applied to a 2D-TPP dataset profiling ATP and GTP in a crude cell extract. The analysis of these datasets revealed functional roles of ATP in proteome regulation ranging from allosteric binding, over protein complex assembly and condensate formation.

Last, a method for analysis of TPP experiments to profile the effect of PTMs is presented. While the application of this method led to the detection of phosphosites known to be involved in protein regulation, it also pointed out sites which appear to be involved in controlling the localization of proteins to membrane-less organelles.

Taken together, this thesis introduces and showcases computational methods for different application areas of TPP. The presented methods are implemented as open source software packages to enable long-term availability and access to the broader community.

Zusammenfassung

In den letzten Jahrzehnten hat sich das Forschungsfeld der Molekularbiologie zunehmend in eine Disziplin mit hohem Datenaufkommen entwickelt. Dieser Trend wird stark durch die Entwicklungen im Bereich der Bildgebungsverfahren und dem kontinuierlichen Zuwachs an Omics Technologien, die Hochdurchsatzmessungen von verschiedenen Biomolekülen in biologischen Systemen erlauben, vorangetrieben.

Klassische Omics Methoden erstellen ein Profil der Abundanz von tausenden zellulären Biomolekülen, wie zum Beispiel von Ribonukleinsäuren oder Proteinen. Vor Kurzem entwickelte Verfahren, wie Thermal Proteome Profiling (TPP), ermöglichen es zudem, Informationen über biophysische Zustände von Proteinen zu liefern. Durch die Wahl des passenden Versuchsaufbaus oder durch die Kontextualisierung von TPP Experimenten, können diese Interaktionen von Proteinen mit niedermolekularen Verbindungen, Protein-Protein Interaktionsdynamiken oder Auswirkungen von post-translationalen Modifikationen aufdecken. Während jedoch Verbesserungen von Versuchsaufbauten, Reproduzierbarkeit, Durchsatz und die Anzahl der Organismen, auf die das Verfahren angewendet werden kann, stetig zunehmen, fehlen die entsprechenden Methoden, um die dabei erzeugten Daten statistisch auswerten zu können.

Diese Doktorarbeit schlägt eine Reihe von computergestützten Methoden vor, um Werkzeuge für die statistische Analyse einiger der zuvor genannten Anwendungsgebiete von TPP zu liefern.

Als erstes wird ein Softwarepaket zur Analyse von TPP Experimenten mit Hinblick auf Protein-Protein Interaktionen in verschiedenen Zell- oder Behandlungszuständen

vorgelegt. Die Anwendung dieser Methode auf unterschiedliche TPP Datensätze führte dabei zur Entdeckung von signifikant unterschiedlichen Protein-Protein Interaktionen zwischen verschiedenen Phasen des menschlichen Zellzyklus. Desweiteren fanden wir unterschiedliche Ausprägungen von Protein-Komplexen in *Escherichia coli*, abhängig davon, ob sie sich innerhalb eines oder über verschiedene Zellkompartimente hinweg, ausbreiteten.

Zweitens behandelt diese Arbeit einen speziellen experimentellen Ansatz von TPP—2D-TPP. Hierbei wird das experimentelle Design so gewählt, dass die thermale Stabilität von Proteinen als Funktion von Temperatur und der Konzentration einer chemischen Verbindung proteomweit gemessen wird, um Proteine zu finden, die mit der getesteten Verbindung interagieren. Dies wurde umgesetzt, indem ein kurvenbasierter Hypothesentest zur Analyse erzeugter Daten mit Kontrolle der ‘False Discovery Rate’ implementiert wurde. Diese Methode wurde anhand von einem simulierten und mehreren echten Datensätzen getestet. Die Anwendung dieser Analysemethode auf 2D-TPP Datensätze, die zur Bestimmung von Interaktionsprofilen epigenetischer Wirkstoffe aufgenommen wurden, führte zur Entdeckung zuvor nicht bekannter, unerwünschter Interaktionspartner und indirekter Auswirkungen dieser Wirkstoffe auf zelluläre Stoffwechselwege.

Drittens wurde dieselbe statistische Methode zur Bestimmung von ATP und GTP Interaktionspartnern in mechanisch erzeugten Zellysaten, basierend auf einem dementsprechenden 2D-TPP Datensatz, angewandt. Die Analyse der dabei erhaltenen Ergebnisse ergab, dass ATP in verschiedene Regulationsprozesse des intrazellulären Proteoms, neben der bekannten Rollen als Substrat sowie auch als allosterischer Modulator, involviert ist. Diese umfassten zum Beispiel die Assemblierung von Proteinkomplexen und der Formation von Proteinkondensaten.

Als letztes wird eine Methode zur Analyse von TPP Experimenten zur Bestimmung von funktionellen post-translationalen Modifikationen vorgestellt. Die Anwendung dieser Methode konnte Phosphorylierungsstellen detektieren, deren Rollen in der Regulation von Proteinen schon bekannt waren. Darüberhinaus hob die Methode aber auch Phosphorylierungsstellen mit bisher unbekannter Funktion hervor, die in der Lokalisationsregula-

tion von Proteinen, die Teil von nicht-membranumschlossenen Organellen sind, involviert zu sein scheinen.

Zusammengefasst stellt diese Doktorarbeit verschiedene statistische Methoden zur Analyse von TPP Experimenten vor und veranschaulicht ihre Funktionsweise durch die Anwendung auf Datensätzen mit unterschiedlichen analytischen Zielen. Die vorgestellten Analysemethoden sind als Open-Source-Software Pakete implementiert, um eine langfristige Verfügbarkeit und den Zugang für die breite Forschungsgemeinschaft zu gewährleisten.

Table of Contents

Abstract	i
Zusammenfassung	iii
Acknowledgements	xi
Contributions	xiii
List of Publications	xiv
List of Abbreviations	xvii
List of Figures	xxii
List of Tables	xxiii
Summary of Thesis Chapters	xxiv
1 Introduction	1
1.1 Modern technologies to study molecular biology	2
1.2 Mass spectrometry-based proteomics	3
1.2.1 Mass analyzer	4
1.2.2 Modern high-resolution mass spectrometers	5
1.2.3 Bottom-up proteomics	7
1.2.4 Peptide database search	7

1.2.5	Quantitative proteomics to compare different conditions	8
1.2.6	Beyond measuring protein abundance	11
1.3	Statistical methods to analyze genome scale data	19
1.3.1	Linear models for differential analysis	21
1.3.2	Empirical Bayes methods	21
1.3.3	Statistical analysis of TPP experiments	23
2	Materials and Methods	29
2.1	Software and required packages	29
2.2	Publicly available datasets used in this work	31
2.3	Experimental methods	31
2.3.1	Thermal proteome profiling (TPP)	31
2.3.2	Solubility proteome profiling (SPP) experiments	36
2.3.3	ATP depletion and in-cell SPP	36
2.3.4	Phospho-TPP experiments	37
2.3.5	MS sample preparation	38
2.3.6	LC-MS/MS analysis	38
2.3.7	Fluorometric aminopeptidase assay	39
2.3.8	Differential scanning fluorometry with DHRS1	40
2.3.9	BANF1 DNA pulldown	40
2.4	Computational methods	41
2.4.1	Protein identification and quantification	41
2.4.2	Phosphopeptide identification and quantification	41
2.4.3	Analysis of temperature range thermal proteome profiling data . .	43
2.4.4	Thermal coaggregation based on melting point similarity	43
2.4.5	Thermal proximity coaggregation analysis of annotated protein pairs	44
2.4.6	Thermal proximity coaggregation analysis of annotated protein complex subunits	45
2.4.7	Differential thermal proximity coaggregation analysis	45

2.4.8	Detection of ligand-protein interactions from 2D thermal profiles	46
2.4.9	Differential Solubility Proteome Profiling analysis	50
2.4.10	Phospho-TPP data analysis	51
2.4.11	Annotation of protein features and ontologies	54
3	Thermal proteome profiling to probe protein-protein interactions and protein complexes	57
3.1	Thermal proximity coaggregation	58
3.2	An R package for analysis of PPI dynamics using TPP datasets	60
3.2.1	TPCA of datasets in a single condition	60
3.2.2	Detection of differential PPIs using TPCA	62
3.2.3	TPCA of the <i>E. coli</i> proteome	64
3.3	Conclusion	67
4	Computational detection of ligand-protein interactions from two-dimensional thermal proteome profiles	69
4.1	Data obtained from 2D-TPP experiments	70
4.2	A curve-based hypothesis testing framework for 2D-TPP analysis	70
4.3	Benchmarking DLPTP on a synthetic dataset	72
4.4	Application of DLPTP to published 2D-TPP datasets	73
4.5	Target Profiling of the HDAC8-inhibitor PCI-34051	75
4.6	DLPTP analysis of 2D-TPP experiments in rat tissues and human blood	77
4.6.1	<i>Ex vivo</i> 2D-TPP experiments in rat tissues	78
4.6.2	2D-TPP experiment in human blood	81
4.7	Conclusion	82
5	Applying thermal proteome profiling to study protein-metabolite interactions	85
5.1	2D-TPP experiments of ATP and GTP in crude lysate	86
5.2	Indirectly induced thermal stability effects by ATP	88

5.3	Profiling proteome-wide ATP-induced solubilization of insoluble subpopulations	91
5.4	ATP induced loss of solubility of a small group of proteins	99
5.5	Conclusion	101
6	Thermal profiling to identify functional post-translational modifications	103
6.1	Performing TPP of phosphorylated proteins	104
6.2	Hotspot thermal profiling	105
6.3	A revised workflow for phospho-TPP	109
6.4	A nonparametric approach for phospho-TPP analysis	117
6.5	Conclusion	121
7	Discussion	123
7.1	Tracking protein-protein interactions dynamics with TPP	123
7.2	Detection of ligand-protein interactions using TPP	126
7.2.1	FDR-controlled ligand-protein detection with DLPTP	127
7.3	TPP for detection of metabolite-protein interactions	129
7.3.1	ATP effects on protein solubility	130
7.4	Detection of functional PTMs	132
7.5	Conclusion	133
	Bibliography	135
	Appendix	a
	Sensitivity analysis of the DLPTP model	a
	Supplementary Figures	d

Acknowledgements

First of all, I would like to thank my supervisor Misha Savitski. You are a fantastic scientist with a great sense of humour. It has been an amazing time in your lab and I learned more than I could have ever imagined. Thanks for entrusting me with exciting projects and great responsibility in many aspects. It has been a pleasure to do science with you and I hope that we can continue to work together on some projects in the future. Thanks for all the climbing sessions and for showing me how to climb at Riesenstein without breaking my neck. Thanks for fantastic times with the lab such as at conferences, retreats and Christmas parties. And thanks for always being calm, positive, optimistic and relaxed, I should really try to take a leaf out of your book in this regard. Second, I would like to thank Wolfgang Huber. You are a truly inspiring scientist and I am very thankful that I could be co-supervised by you. I am deeply impressed by your knowledge, by how sharply you reason and how rigorously you do science. Your attitude towards open and reproducible science has shaped the way I want to do research and your feedback has always been extremely thorough and productive and really allowed me to grow as a scientist. Thanks for taking me to Bioconductor meetings and giving me the chance to meet all the wonderful people involved in the project and motivating me to contribute to it myself.

Thanks also to Benedikt Brors and Pedro Beltrao for supporting me as thesis advisors and investing your time into TAC meetings and discussions. Both of you always gave creative and supportive input.

Moreover, I would like to thank Marcus Bantscheff. I admire your passion for science.

Thanks for all the input, support and advice you gave. Further, I want to thank all other Cellzomers that I was lucky to collaborate with over the years. I am also very grateful to the Savitski lab as a whole. In particular, I would like to thank Sindhu: thanks for the great time working together. I learned so much from you way beyond science. It has been so much fun and I hope we will stay in touch. Thanks also to Henrik for many discussions both scientific and non-scientific, they really made me reflect a lot on me as a scientist and as a person. Thanks André, you are the most annoyingly clever colleague and friend I could have ever imagined. I learned tons of stuff from you and you supported me with countless things. I'm sure we will stay in touch and I am looking forward to seeing the fantastic science you are going to bring forward in the future! Merci Clément, it has been great fun working together. Thank you Isabelle, your organization, cakes and support really held the lab together during these years. A big thanks also to Cécile, Tomi, Johannes, Zhu, Maike, Lisa, Mira and the PCF: Per, Frank, Dominic, Mandy and Jenny.

Moreover, I would like to thank the Huber group. In particular, Simone, Mike, Constantin, Britta and Dorothee.

Apart from my colleagues, I want to thank the climbing crew at EMBL: Daya, Bernhard, Tischi and Sami. And my bouldering crew: Sophie, Konrad, Sophie, Dimitris, Jakub, Nic, Daniel and many others. Climbing is the reason I stayed sane all these years. Thanks also to the brewing club and in particular to Mathias and Jakob and to Daniel for all the beers, dinners and discussions about science, life, philosophy and what not.

Thanks to EMBL, its funders and the PhD program. I am very grateful to all who have made my time here possible. Last, but not least I want to thank Hanna and my family for their tremendous support. Without you guys I would not have made it anywhere. I love you and cannot express how much you mean to me.

Contributions

All computational methods and analyses presented in this thesis were conceptualized and performed by me, if not stated otherwise. The presented R/Bioconductor software packages `Rtpca` (<https://bioconductor.org/packages/release/bioc/html/Rtpca.html>) and `TPP2D` (<https://bioconductor.org/packages/release/bioc/html/TPP2D.html>) were conceptualized and implemented by me with input from Mike Smith, Constantin Ahlmann-Eltze, Holger Franken, Simon Anders, Wolfgang Huber and Mikhail Savitski. The NPARC-GP implementation was adapted based on code from Britta Velten.

All wet-lab experiments presented in this thesis were performed by my colleagues:

TPP experiments in *Escherichia coli* were performed by André Mateus.

2D-TPP experiments of PCI-34051 and BRD-3811 and follow-up experiments with LAP3 were performed by Isabelle Becher.

2D-TPP experiments in blood and rat liver were performed by Jessica Perrin, Thilo Werner and Anna Rutkowska.

2D-TPP and SPP experiments of ATP, GTP and AMP-PNP in Jurkat crude lysate, and ATP-depletion experiments in Jurkat cells with subsequent proteomics analysis and follow up experiments with BANF1 were performed by Sindhuja Sridharan.

Phospho-TPP experiments in HeLa cells were performed by Clément Potel, André Mateus and Isabelle Becher.

In all projects, I was involved in discussions on experimental design, decision on follow-up experiments, their realization and interpretation.

List of Publications

Thesis related

- Potel, C.#, **Kurzawa, N.#**, Becher, I.# et al. 2021. "Impact of phosphorylation on thermal stability of proteins." *Nat. Methods* accepted, preprint: <https://doi.org/10.1101/2020.01.14.903849>
- **Kurzawa, N.#**, Becher, I.# et al. 2020. "A computational method for detection of ligand-binding proteins from dose range thermal proteome profiles." *Nat. Commun.* 11, 5783. <https://doi.org/10.1038/s41467-020-19529-8>
- **Kurzawa, N.**, Mateus, A. & Savitski, M.M. 2020. "Rtpca: an R package for differential thermal proximity coaggregation analysis." *Bioinformatics* btaa682. <https://doi.org/10.1093/bioinformatics/btaa682>
- Perrin, J.#, Werner, T.#, **Kurzawa, N.#**, et al. 2020. "Identifying drug targets in tissues and whole blood by thermal shift profiling". *Nat. Biotech.* 38, 303–308. <https://doi.org/10.1038/s41587-019-0388-4>
- Sridharan, S.#, **Kurzawa, N.#** et al. 2019. "Proteome-wide thermal stability and solubility profiling reveals distinct regulatory roles for ATP" *Nat. Commun.* 10, 1155. <https://doi.org/10.1038/s41467-019-09107-y>
- Becher, I.#, Andrès-Pons, A.#, Romanov, N.#, Stein, F.#, ..., **Kurzawa, N.** et al. 2018. "Pervasive protein thermal stability variation during the cell cycle" *Cell*

173, 1495-1507.e18. <https://doi.org/10.1016/j.cell.2018.03.053>

- Mateus, A., Bobonis, J., **Kurzawa, N.**, et al. 2018. "Thermal proteome profiling in bacteria: assessing protein state in vivo". *Mol. Sys. Biol.* 14:e8242. <https://doi.org/10.15252/msb.20188242>

Reviews

- Mateus, A.#, **Kurzawa, N.#**, Becher, I., Sridharan, S., Helm, D. Stein, F., Tympas A. & Savitski, MM. 2020. "Thermal proteome profiling for interrogating protein interactions". *Mol. Sys. Biol.* 16:e9232. <https://doi.org/10.15252/msb.20199232>

Other contributions

- Jarzab, A.#, **Kurzawa, N.#**, Hopf, T. et al. 2020. "Meltome atlas: thermal stability across the tree of life." *Nat. Methods* 17, 495–503. <https://doi.org/10.1038/s41592-020-0801-4>
- Mathieson, T.#, Franken, H.#, Kosinski, J.#, **Kurzawa, N.#** et al. 2018. "Systematic analysis of protein turnover in primary cells". *Nat. Commun.* 9, 689. <https://doi.org/10.1038/s41467-018-03106-1>
- Selkrig, J.#, Stanifer, M.#, Mateus, A.#, Mitosch, K.#, Barrio-Hernandez, I.#, Rettel, M.#, ..., **Kurzawa, N.** et al. 2021. "SARS-CoV-2 infection remodels the host protein thermal stability landscape." *Mol. Sys. Biol.* accepted
- Kalxdorf, M., ..., **Kurzawa, N.** et al. 2021. "Tracking drug action on the cell surface." *Nat. Methods* 18, 84–91. <https://doi.org/10.1038/s41592-020-01022-1>
- Mateus, A., Hevler, J., Bobonis, J., **Kurzawa, N.** et al. 2020. "The functional proteome landscape of *Escherichia coli*." *Nature* 588, 473–478. <https://doi.org/10.1038/s41586-020-3002-5>

- Hoermann, B., Kokot, T., ..., **Kurzawa, N.** et al. 2020. "Dissecting the sequence determinants for dephosphorylation by the catalytic subunits of phosphatases PP1 and PP2A." *Nat. Commun.* 11, 3583. <https://doi.org/10.1038/s41467-020-17334-x>
- Määttä, T., ..., **Kurzawa, N.** et al. 2020. "Aggregation and disaggregation features of the human proteome." *Mol. Sys. Biol.* 16:e9500. <https://doi.org/10.15252/msb.20209500>

Manuscripts in preparation

- Stahl, M.[#], **Kurzawa, N.**[#], Mateus, A. et al. "Deep thermal profiling of genetically diverse ALL proteomes." *in preparation*

[#] Shared first authors.

List of Abbreviations

2DG	2-Deoxyglucose
AA	Antimycin A
ACN	Acetonitrile
AMP-PNP	Adenylyl-imidodiphosphate (non hydrolysable analogue of ATP)
ANOVA	Analysis of variance
ATP	Adenosine triphosphate
AUC	Area under the (receiver operating characteristic) curve
BET	Bromo- and extra-terminal (protein domain)
BioID	Proximity-dependent biotin identification
CETSA	Cellular thermal shift assay
DARTS	Drug affinity response target stability
DDA	Data-dependent acquisition
DIA	Data-independent acquisition
DLPTP	Detection of ligand-protein interactions from thermal profiles
DOF	Degree of freedom
ED	Euclidean distance
ESI	Electrospray ionization
FBS	Fetal bovine serum
FDR	False discovery rate
FPR	False positive rate
GO	Gene ontology

GTP	Guanosine triphosphate
HCD	High energy collision-induced dissociation
HTP	Hot spot thermal profiling
IMAC	Immobilized metal ion affinity chromatography
iTRAQ	Isobaric tags for absolute and relative quantification
LiP-MS	Limited proteolysis mass spectrometry
LC	Liquid chromatography
MLE	Maximum likelihood estimation
MS	Mass spectrometry
MS1	Mass spectrometry scan of intact ions
MS2	Mass spectrometry scan of fragmented ions
MS/MS	Tandem mass spectrometry analysis
m/z	Mass to charge ratio
NADP	Nicotinamide adenine dinucleotide phosphate
NPARC	Nonparametric analysis of response curves
NPARC-GP	Nonparametric analysis of response curves with Gaussian processes
PCR	Polymerase chain reaction
PBS	Phosphate buffered saline
pEC ₅₀	Half maximal effective stabilization concentration
pESC ₅₀	Half maximal effective solubilization concentration
PPI	Protein-protein interaction
ppm	Parts per million
PSM	Peptide spectrum match
PTM	Post-translational modification
ROC	Receiver operating characteristic
RSS	Residual sum of squares
SDS	Sodium dodecyl sulfate
SEC	Size exclusion chromatography

SILAC	Stabile isotope labeling of amino acids in cell culture
SPP	Solubility proteome profiling
SPROX	Stability of proteins from rates of oxidation
TF	Transcription factor
TMT	Tandem mass tags
TPCA	Thermal proximity coaggregation
TPP	Thermal proteome profiling
TPP-CCR	Compound concentration range thermal proteome profiling
TPP-TR	Temperature range thermal proteome profiling
TPR	True positive rate

List of Figures

1.1	Illustration of an Orbitrap mass analyzer.	5
1.2	Schematic of a modern Orbitrap mass spectrometer.	6
1.3	Standard workflow for bottom-up proteomics.	9
1.4	Workflow to perform quantitative proteomics using chemical labeling for multiplexing.	11
1.5	Illustration of the experimental TPP-TR workflow.	17
1.6	Illustration of the experimental 2D-TPP workflow.	18
1.7	Illustration of the <i>t</i> -test and the ANOVA.	20
1.8	Illustration of how linear models can account for covariate structure. . . .	22
1.9	Empirical Bayesian variance estimation by sharing of information across proteins	23
1.10	Analysis strategies for TPP-TR experiments.	25
1.11	Analysis strategy for 2D-TPP experiments.	27
3.1	Assessing coaggregation by melting point similarity.	58
3.2	The concept of thermal proximity coaggregation analysis	59
3.3	PPI and complex predictive performance of TPP datasets of different cell cycle stages.	61
3.4	Results obtained from differential thermal coaggregation analysis between G1/S and M phase.	64
3.5	TPCA of protein complexes in <i>E. coli</i>	66

4.1	Illustration of data obtained from 2D-TPP experiments and design of DLPTP’s nested models.	71
4.2	A benchmark of DLPTP with a synthetic dataset confirms FDR control and improved sensitivity compared to the threshold-based approach. . . .	73
4.3	DLPTP recovers known drug-binding proteins based on published datasets.	74
4.4	Target profiling with 2D-TPP of the HDAC8 inhibitor PCI-34051 and its analog BRD-3811.	76
4.5	DLPTP analysis of 2D-TPP experiments performed in rat tissues.	80
4.6	DLPTP analysis results for 2D-TPP datasets obtained with human blood.	82
5.1	DLPTP analysis results for the 2D-TPP experiments profiling ATP and GTP in crude lysate.	87
5.2	Co-stabilization of complex subunits by ATP.	89
5.3	Exemplary heatmaps of ATP and GTP induced stability fold changes at different temperatures.	90
5.4	Schematic of the experimental workflow for Solubility Proteome Profiling.	92
5.5	SPP experiments inform on insoluble subpopulation and solubilizing effect of ATP.	93
5.6	Susceptibility for solubilization by ATP varies across membrane-less organelles.	95
5.7	SPP experiments in intact cells with depleted ATP levels.	97
5.8	Proteins which loose solubility in the presence of high ATP concentrations.	100
6.1	Scatterplot of estimated melting points for proteoforms with specific phosphites and corresponding unmodified proteins from the data of Huang et al.	105
6.2	Melting point reproducibility for phosphorylated proteoforms from the HTP data.	106
6.3	Schematic of the HTP and our revised phospho-TPP workflow.	108
6.4	Comparison of raw and normalized unmodified protein melting profiles. . .	110

6.5	Comparison of raw and normalized phosphopeptide melting profiles. . . .	111
6.6	The revised phospho-TPP workflow improves comparability between ob- tained melting points for phosphorylated and unmodified proteins. . . .	113
6.7	Comparison of distribution of functional scores by Ochoa et al. (2020) between shifted vs. non-shifted phosphosites.	115
6.8	Examples of phosphosites found to significantly shift thermal stability of proteins.	116
6.9	Examples of non-sigmoidal thermal profiles.	118
6.10	NPARC-GP results obtained for the phospho-TPP dataset.	120
6.11	Examples of unusual melting profiles captured by NPARC-GP.	121
S1	Sensitivity analysis based on the example of BRD4 in the JQ1 lysate dataset.	b
S2	Sensitivity analysis based on the example of the HDAC6 in the Panobino- stat in-cell dataset.	c
S3	Chemical structures of Panobinostat and some of its metabolized forms. . .	e
S4	Chemical structures of further small molecules used in this work.	f
S5	Chemical structures of metabolites and metabolite analogs used in this work.	g
S6	Control experiments to confirm ATP's effect on insoluble proteins is not driven by ATP hydrolysis.	h
S7	Intracellular ATP levels after depletion with D1 and D2.	i
S8	Comparison of melting point estimates obtained from different replicates of unmodified proteins.	j
S9	Comparison of melting point estimates obtained from different replicates of phosphopeptides.	k
S10	Calibration of obtained NPARC-GP results of phospho-TPP data	l

List of Tables

2.1	R environment and session info	29
2.2	Summary of R packages and their versions	30
2.3	Overview of publicly available datasets used in this work.	32
2.4	Database search parameters for standard peptide identification.	42
2.5	Database search parameters for phosphopeptide identification.	42

Summary of Thesis Chapters

Chapter 1 – Introduction

In this chapter, the basics of applying high throughput methods to study molecular biology are introduced. Special emphasis is placed on the fundamentals of mass spectrometry-based proteomics and on different methods, which are based on this technology, to measure protein abundance, post-translational modifications and biophysical states of proteins. In this context the underlying principles of thermal proteome profiling (TPP) for detection of ligand-protein interactions are introduced. Further, statistical methods for genome-scale analysis of datasets obtained with high throughput technologies are introduced.

Chapter 2 – Materials and Methods

This chapter comprises tables of utilized software and publicly available datasets and detailed descriptions of experimental and computational methods used in this work.

Chapter 3 – Thermal proteome profiling to probe protein-protein interactions and protein complexes

This part of the thesis focuses on the detection of protein-protein interactions (PPIs) and association of protein complex subunits based on TPP datasets. An R/Bioconductor package Rtpca which was implemented for this task is presented. Moreover, a method for

detection of differential PPIs is suggested. This method is applied to find differential PPIs between interphase and mitosis in human cells. Additionally, association of subunits of protein complexes in *E. coli* is analyzed based on a TPP dataset. Based on this it is found that subunits of complexes in the same compartment showed more similar coaggregation as subunits in different compartments.

Chapter 4 – Computational detection of ligand-protein interactions from two-dimensional thermal proteome profiles

In this chapter, a computational method termed DLPTP for false discovery rate-controlled detection of ligand-protein interactions from 2D-TPP datasets is presented. The approach is benchmarked on a synthetic dataset and applied to several real datasets. This leads to the discovery of LAP3 as an off-target of the HDAC8 inhibitor PCI-34051. Moreover, the method is applied to 2D-TPP experiments performed *ex vivo*—in rat tissues—and reveals engagement of different drugs with expected targets, but also induction of cellular downstream processes.

Chapter 5 – Applying thermal proteome profiling to study protein-metabolite interactions

This part presents the application of DLPTP to analyze a 2D-TPP dataset profiling protein interaction with the nucleotides ATP and GTP in mechanically disrupted cells. It is shown that the method recovers known and previously unannotated interactors of the two metabolites. Further, it is found that ATP affects interactions of proteins to which it binds. In addition to the effects on thermal stability, ATP also appears to affect solubility of subsets of proteins. Additional experiments dedicated to further characterize these solubility effects are presented and they showed that, independent of its hydrolysis, ATP appears to predominantly affect solubility of protein localizing to membrane-less organelles.

Chapter 6 – Thermal profiling to identify functional post-translational modifications

This chapter starts by the re-evaluation of a recently published method which uses a combination of phosphopeptide enrichment and thermal proteome profiling. It is shown that this method suffers from poor reproducibility and that the obtained results are misleading. Through further analysis of the underlying problems of the approach and implementation of revised experimental and computational analyses, it is possible to identify functional phosphorylation sites. Further analysis of the data obtained with this revised method leads to the discovery of phosphorylation sites which induce non-sigmoid melting curves of corresponding proteoforms. A computational analysis is devised which can account for such cases and applied to the dataset. Based on the example of a protein, which is part of ribonucleosomes, it is shown that patterns of such non-sigmoid melting curves can be indicative of phosphorylation sites regulating the localization of proteins to insoluble subpopulations.

Chapter 7 – Discussion

In this part of the thesis, the results obtained in the previous chapters are revisited and discussed in light of the current literature.

Chapter 1

Introduction

“We still don’t know one thousandth of one percentage of what nature has revealed to us.”

— Albert Einstein

All living organisms are built up of cells. Each of which constitutes a spatially constrained compartment which usually contains the organism’s genetic material in form of DNA, other nucleic acids such as RNAs, proteins, sugars, lipids and other organic molecules (Alberts et al., 2007, pp. 1–10, 54–64). According to the central dogma of molecular biology the DNA of most genes is transcribed to messenger RNA which, in turn, is translated into proteins (Alberts et al., 2007, pp. 331–339, 366–382). This simplified model of gene expression illustrates how the genetic material can be converted into functional gene products, that can perform a variety of functions, including catalysis of chemical reactions or modulation of cellular morphology and appearance. By restricting expression to a subset of genes, organisms can use their genetic material to create phenotypically distinct cells which can perform diverse tasks (Alberts et al., 2007, pp. 454–466).

The field of systems biology is concerned with understanding how cells and organisms operate by making use of their genetic inventory (Kirschner, 2005). In this context, it has been a long-standing problem to understand functions of gene products, how they

are regulated and how they work together under different conditions. While much has been learned from experiments dedicated to one or a handful of gene products, it has been increasingly realized that most processes and their underlying actors inside cells are highly interconnected and thus difficult to study in isolation. Therefore, there have been efforts to find means of quantitatively measuring many or even all detectable elements of a type of biological molecule in different organisms and conditions to gain a more holistic view of cellular states and the interconnected changes upon perturbation.

However, even with a quantitative readout of a large proportion of biomolecules in hand, researchers often struggle to infer the underlying biological mechanisms which lead to observed effects in response to varying conditions or perturbations. Thus, in the last years, methods have been developed that do not only inform on the abundance, but also on the functional state of biomolecules and their interactions among each others. The statistical analysis of such datasets, however, entails several novel challenges, some of which are approached within this thesis.

1.1 Modern technologies to study molecular biology

In the last 30 years the development of methods to interrogate molecules inside biological systems has drastically accelerated. The development of DNA microarray technologies, which consist of glass plates with spotted DNA fragments, that allow for fluorophore-mediated readout of hybridization events of complementary DNA strings, for the first time allowed the simultaneous measurement of hundreds to thousands of transcript levels in cellular samples (Schena et al., 1995).

A few years later sequencing-based approaches entered the stage. Sequencing of nucleic acids had been established before (Maxam & Gilbert, 1977; Sanger et al., 1977), however the costs and throughput involved in the classical sequencing approaches did not allow to run these experiments at a large scale. The establishment of next-generation short read sequencing (Bentley et al., 2008), i.e., massively parallel sequencing by synthesis on flow cells using dye-labeled nucleotides, whose incorporation is recorded optically, soon

overcame this limitation. At that time, the technology developed was strongly driven by the great interest in genome sequencing, but through parallel assay development based on this sequencing technology, profiling of transcripts levels (Nagalakshmi et al., 2008), probing presence of epigenetic modifications at specific genomic loci (Cokus et al., 2008) and detection of binding events of transcriptions factors (Johnson et al., 2007; Robertson et al., 2007) all joined the toolbox of accessible technologies to profile living organisms. All sequencing-based methods have in common that they rely on sequencing of DNA fragments, mapping back the sequenced reads to the genome and counting the occurrence of events of interest, e.g., observation of reads with a genomic variant, an epigenetic modification or of a certain transcript.

1.2 Mass spectrometry-based proteomics

A long time before approaches to profile nucleic acids were developed, a technology termed mass spectrometry (MS) was developed, with the aim to measure the mass to charge ratio (m/z) of ions. However, the scope of the original method developed by John Thomson was by no means to measure biomolecules, but rather the structure of atoms to begin with (Thomson, 1913).

Decades later, a breakthrough discovery by John Fenn and colleagues, who developed a universal method for *in vacuo* ionization of large biomolecules in solution, termed electrospray ionization (ESI) (Fenn et al., 1989), paved the way for its application in molecular biology.

Nowadays, MS finds application in the fields of *proteomics*, *metabolomics* and *lipidomics*. Moreover, in proteomics, it is applied in many different ways. The most common are i) to quantify expression of all detectable proteins in complex samples by measurement of representative peptides obtained from tryptic digest of extracted proteins (Bantscheff et al., 2012), ii) to measure the abundance of a targeted part of the proteome (Shi et al., 2016), iii) to analyze different proteoforms, i.e., the same protein with, e.g., different post-translational modifications, of intact proteins (Donnelly et al., 2019), and iv) to measure

three-dimensional constraints of protein residues in complexes using cross-linkers to aid structural biology approaches (O'Reilly & Rappsilber, 2018).

1.2.1 Mass analyzer

At the heart of each mass spectrometer lies its mass analyzer. This component represents the actual tool capable of measuring m/z of ions. Different types of mass analyzers exist and are based on different principles.

Time of flight instruments

Time of flight (TOF) mass analyzers exploit the fact that the speed at which ionized molecules travel in an electric field depends on mass and charge of the particle. Typically, such instruments consist of a tube into which ions are injected with a controlled energy and travel from one end to the other towards a detector. Given the known length of the tube and the strength of the electric field, the m/z of a given particle can be determined by measuring its time of flight. The longer the distance traveled by the molecule, the more precisely the mass to charge ratio of particles can be measured (Cotter, 1999).

Ion traps

A different approach to measuring the m/z of an ionized molecule is to capture, i.e., to *trap* it in an electric field, e.g., by switching the polarity of its surrounding electrodes. By measuring the oscillation of the trapped ion in such a system, one can infer its m/z . Different types of ion traps exist with an important one represented by the *Orbitrap* (Figure 1.1): a trap in which ions are forced onto an orbit around a spindle and its characteristic oscillations in z -direction are used to infer its m/z . This instrument was developed by Alexander Makarov and offers high mass resolution and speed (Hu et al., 2005; Makarov, 2000).

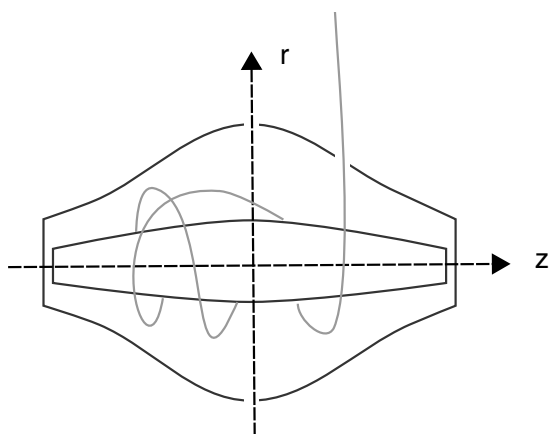


Figure 1.1: Illustration of an Orbitrap mass analyzer. Ions are injected orthogonally to the z -axis and forced onto an orbit around the axial electrode by an electric field. The frequency of harmonic oscillations along the z -axis are inversely proportional to the square root of m/z and can be converted into spectra by fast Fourier transformation (Makarov, 2000). The spectrum intensity is thereby indicative of the ion's abundance. Schematic drawn based on Fig. 1 by Hu et al. (2005).

1.2.2 Modern high-resolution mass spectrometers

Mass spectrometers, however, do not only consist of mass analyzers. Several components are pre-connected in front of the mass analyzer to focus and filter the ion beam to enable successful m/z measurement (Figure 1.2). By successively selecting specific m/z ranges of ions, eluted at a certain time point, it is possible to measure a substantial fraction of proteins extracted from a biological source, e.g., 5,000 - 10,000 for human samples (Bantscheff et al., 2012).

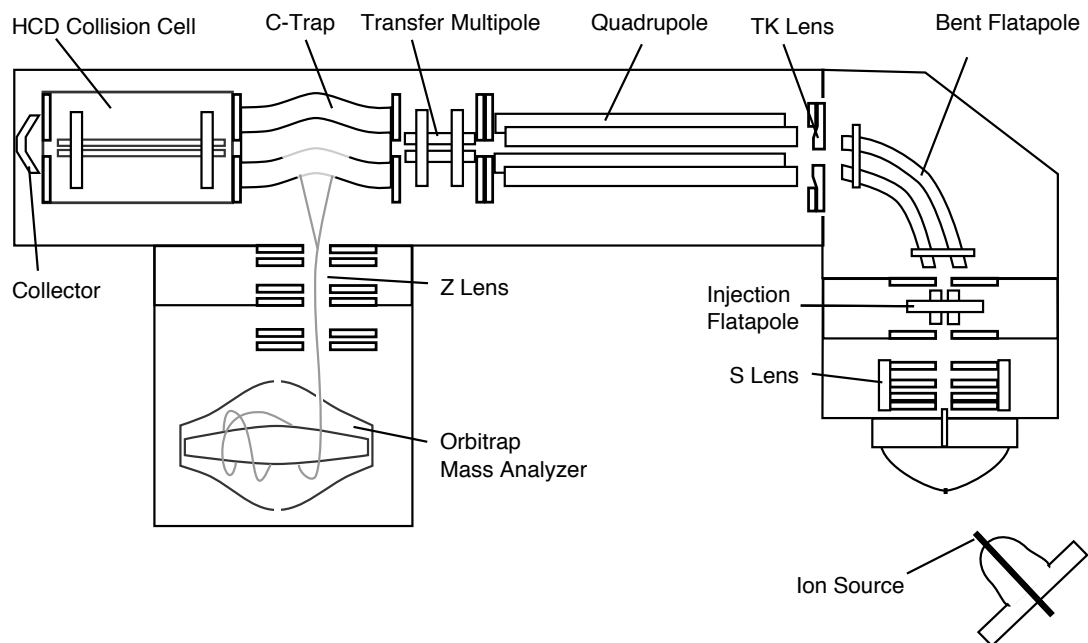


Figure 1.2: Schematic of a modern orbitrap mass spectrometer. After online separation of peptides by liquid chromatography and ionization, positively charged peptides are injected into the instrument. The ion beam is focused by the S lens and forwarded into the bent flatapole which leads charged particles along the curvature, whereas uncharged ones collide. Ions are then injected into the quadrupole, where they are filtered for a certain m/z range and forwarded to the C-trap. In the C-trap filtered ions are gathered before they are injected through the Z lens into the Orbitrap. While a first MS spectrum (MS1) is recorded, ions of selected m/z ranges are sent into the collision cell in which they are fragmented through high energy induced gas collisions (HCD). Resulting fragments are then transported back into the C-trap and injected into the Orbitrap to record a second MS spectrum (MS2). By subsequently measuring MS1 scans for several m/z ranges and triggering MS2 scans in case the measured signal in the first recording fulfills certain criteria, a large fraction of the peptides present in a complex sample can be measured. Schematic drawn based on Fig. 2 by Michalski et al. (2011).

1.2.3 Bottom-up proteomics

Over the years, an approach termed *bottom-up* proteomics has emerged as the standard workflow to quantify an, as large as possible, fraction of an organism's proteome (Figure 1.3). The term 'bottom-up' refers to the principle of digesting proteins into small peptides, measuring the abundance of these peptides and mapping them back to proteins and thus estimating the abundance of proteins. The digestion of proteins to peptides is typically performed by proteases with a defined cleavage pattern, such as trypsin, which cuts only C-terminal of lysine or arginine. Samples are then desalted and online fractionated by high pressure reverse phase liquid chromatography (LC), which elutes polar peptides first and hydrophobic peptides last, before samples are ionized using ESI and injected into the mass spectrometer. In modern Orbitrap instruments (Figure 1.2), ions are focused and systematically filtered for different mass to charge ranges using quadrupoles and are subsequently measured in tandem (MS/MS) (Michalski et al., 2011). This means that first a spectrum of a certain mass range of a given peptide sample is recorded and then selected mass ranges of these ions are transported into a collision cell where they are collided with gas atoms and thereby fragmented preferentially at their peptide bonds. These peptide fragments are then transported to the mass analyzer, where a second scan is performed and a fragment ion spectrum is obtained. Based on the parent ion mass and the fragmentation pattern, peptides can be identified by searching against a database generated by *in silico* synthesis of all possible spectra expected for a certain organism. Quantification of identified peptides can then be performed using different strategies outlined in Section 1.2.5: "Quantitative proteomics to compare different conditions".

1.2.4 Peptide database search

In order to identify peptides based on their measured mass and fragmentation spectrum, a database, specific to the organism, from which the sample has been obtained from, is created *in silico*. This includes computationally digesting all protein sequences with the chosen protease, calculating expected m/z ratios for differently charged peptide sequences

and fragmenting those sequences and determining theoretically expected spectra. Peptide measurements are then compared with possible matching theoretical spectra obtained in this way and a score, based on how likely a combination of observed spectral matches would randomly occur for a given query based on a binomial model, is computed (Cox et al., 2011). In order to control for false positives, the same approach is in parallel performed with all reversed protein sequences, a so called *decoy* database (Elias & Gygi, 2007). Typically, at a false discovery rate (FDR) of 1%, determined as the highest score at which 1% of the total observed peptides spectrum matches (PSMs) are found with the reversed sequence database, PSMs are accepted and used to quantify peptides and subsequently proteins (Elias & Gygi, 2010).

When inferring proteins from identified peptides accepted at a certain FDR, however, one needs to consider that there remains a higher risk of finding false positive proteins than at the accepted peptide-level FDR. Hence, a protein-level FDR procedure is typically performed. The *picked approach* uses all forward and reverse peptides identified at a given FDR cutoff. For each protein, forward and reverse, the score of its highest scoring peptide is set. Then for each pair of forward and reverse proteins the one with the lower score is removed and the remaining list is sorted by score and the same FDR procedure as for peptides is applied (Savitski et al., 2015). Protein FDR is usually also set to be below 1%.

1.2.5 Quantitative proteomics to compare different conditions

Different strategies to perform comparative proteomics experiments have been developed. First, so called label-free experiments were performed, which usually quantify proteins based on their MS1 spectrum. This approach relies on performing fully independent MS experiments for each replicate of a biological condition that is to be compared. Challenges associated with this approach are that individual MS experiments are never simply comparable, but have to be normalized by means such as by aligning LC elution profiles (Cox et al., 2014). However, even with application of appropriate normalization proce-

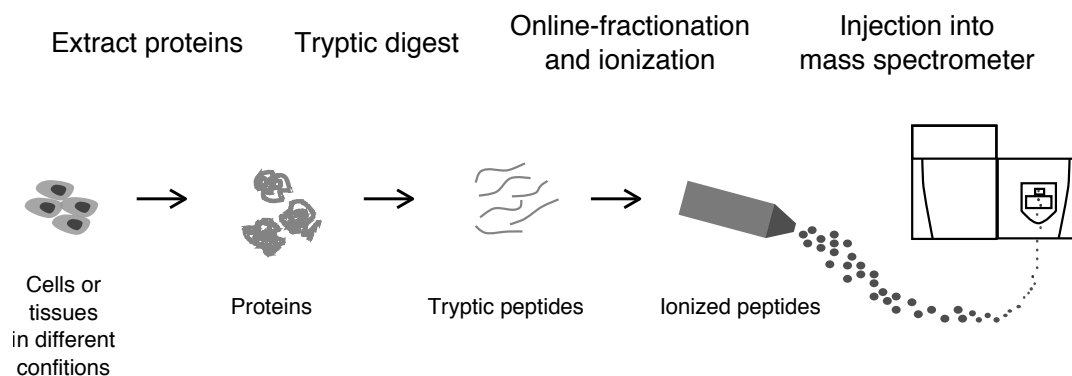


Figure 1.3: Standard workflow for bottom-up proteomics. Proteins are extracted from the sample, digested into peptides using the enzyme trypsin, fractionated via C-18 solid phase liquid chromatography, ionized and injected into the mass spectrometer.

dures, inference of accurate fold changes between conditions remains challenging. Second, strategies evolved that made use of stable heavy isotope-labeling of amino acids in cell culture (SILAC). This approach requires cells to be grown in culture. It is then made use of differentially heavy isotope-labeled amino acids, e.g. deuterium-labeled heavy L-leucine vs. normal L-leucine, which are exclusively present in this form in the sample medium of cells in a specific condition (Ong et al., 2002). By growing in such labeled media, the cells successively replace all endogenous amino acids in their proteins with labeled ones. Following extraction of the proteins from both conditions, pooling and performing an MS experiment, the peptides retrieved from the isotope labeled proteins containing a leucine have a shifted mass and can thus be quantified separately for both conditions (Ong et al., 2002). Nowadays, heavy carbon labeled arginine and lysine are used instead of deuterium-labeled leucine which have several analytically favorable characteristics, such as that heavy and light proteins are co-eluted and complete coverage of the amenable proteome can be achieved (Ong et al., 2003). Third, different approaches have been developed to chemically modify peptides obtained after tryptic digest and thus encode different conditions for multiplexing. The two most

used chemical labels are isobaric tags for absolute and relative quantification (iTRAQ, up to 8 channels) (Ross et al., 2004) and tandem mass tags (TMT, up to 16 channels) (Li et al., 2020; Thompson et al., 2003; Werner et al., 2014, 2012). Isobaric tags are amine reactive molecules, designed in a way that their overall mass is the same, but upon fragmentation so called *reporter ions* are formed, which have characteristic masses that can be used to encode different conditions. This is achieved by distributing different isotopes of N and C atoms within these molecules such that the overall mass is equal, but the region forming the reporter ion fragment contains different N and C isotopes allowing for quantification on MS2 level (Pappireddi et al., 2019). Proteomics approaches making use of chemical labeling have the advantage that samples are pooled at an early stage and thus sample handling and instrument performance do not introduce additional batch effects. However, there are also limitations. The most crucial one, termed *ratio compression* (Ow et al., 2011), occurs if measured samples are too complex, i.e. too many different peptides with similar m/z elute at the same time. This phenomenon results in an underestimation of the relative fold change in abundance of a protein in two conditions, induced by the fact that quadrupoles cannot isolate a narrow mass range, leading often to co-isolation of other ions that also carry reporter tags. This co-isolation gets worse with increasing sample complexity. Thus, computational and chromatographic strategies have been developed (Savitski et al., 2013) to establish a workflow (Figure 1.4) which minimizes ratio compression and allows for accurate relative quantification, while reducing instrument time through multiplexing.

Another more recently developed approach is called data independent acquisition (DIA) (Gillet et al., 2012) as opposed to data-dependent acquisition (DDA), which is performed as described above and used by all approaches discussed so far. In DIA the selection of m/z windows, which are chosen for fragmentation, is not dependent on the data, i.e., the instrument systematically chooses windows of m/z ranges to cover all peaks and fragments the ions therein. This strategy is more time efficient than DDA, however comes with the caveat of not being able to identify measured peptides without an appropriate DDA reference measurement or an accurate *in silico* prediction (Yang et al., 2020).

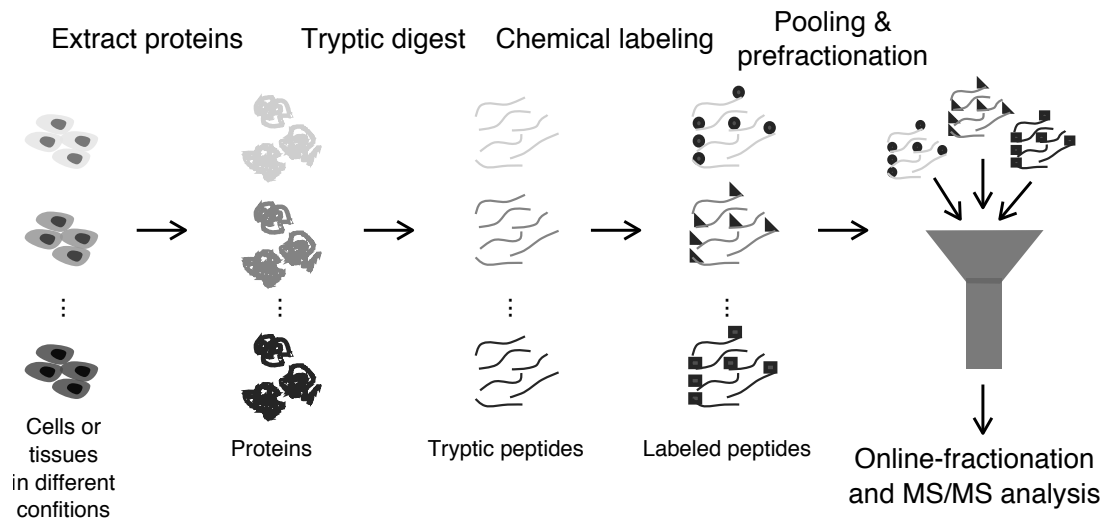


Figure 1.4: Workflow to perform quantitative proteomics using chemical labeling for multiplexing. Proteins are extracted from samples and digested with trypsin. Peptides from different conditions are then labeled with distinct isobaric tags and pooled. Obtained samples are offline pre-fractionated orthogonally to the online chromatography, e.g., at high pH. The different collected fractions are then consecutively injected into the mass spectrometer. Resulting raw files are merged by jointly being searched against the database.

1.2.6 Beyond measuring protein abundance

Apart from modulation of gene expression, cells also use other means of regulating their existing proteins. For instance, post-translational modifications (PTM) can switch proteins from active to inactive or target them for degradation (Karve & Cheema, 2011). These processes, often referred to as intracellular signalling, in many cases allow cells to respond faster to extrinsic cues compared with gene expression. Aside from modification and degradation of proteins, cellular states can also be influenced by interaction

of proteins with one another or with other biomolecules, such as organic compounds or nucleic acids. Over the last years, there has been much effort to establish technologies, which are capable of informing on these interactions on a system-wide level (Larsen et al., 2006).

Measuring post-translational modifications of proteins

The most studied PTM is the reversible modification of proteins with phosphoryl groups (Cohen, 2002). In most cases phosphorylation represents a modification of hydroxy-groups and thus occurs on serine, threonine and tyrosine, but can also be placed on histidine's imidazole ring. The enzymes which place it are termed *kinases*, whereas those which remove it are *phosphatases*. This modification is known to be the information carrier in many important signalling pathways, e.g., major metabolic processes (Linn et al., 1969) or regulation of the cell cycle (Nurse & Bissett, 1981). It has been shown that protein phosphorylation at specific sites on proteins can trigger intramolecular rearrangements often (in-)activating enzymes for signal transduction (Kimura et al., 1996; Young et al., 2001) or modulate protein-protein interactions (PPI) (Nishi et al., 2011). However, in most cases the presence of this PTM in the existing protein pool is highly substoichiometric, i.e., only a small subset of proteins will carry a phosphorylation. Thus, peptides carrying the modifications of interest need to be enriched to enable their measurement with MS. In phosphoproteomics, this is usually achieved using either TiO₂ or immobilized metal ion (usually Fe³⁺) affinity chromatography (IMAC) (Pinkse et al., 2011; Potel et al., 2018). The strongly negatively charged phosphopeptides obtained after tryptic digest, bind to the positively charged metal ions in acidic conditions, while unmodified peptides largely flow through. Phosphopeptides can then be eluted under alkaline conditions. Usually both, flow-through, i.e., unmodified peptides and enriched phosphopeptides are then subjected to MS/MS analysis. This is important to judge whether changes in phosphopeptide abundance are related to abundance changes in the protein or specific to the phosphorylated proteoform.

Other PTMs such as acetylation, SUMOylation and ubiquitination have been shown to have crucial functions within cells and are possible to study with proteomics methods as well (Andersen et al., 2009; Kim et al., 2006; Peng et al., 2003). The principle behind such proteomics methods is usually similar to phosphoproteomics, in the sense that peptides carrying modifications need to be enriched either by using antibodies attached to beads or specific columns which can bind and release respectively modified peptides in different buffers.

Determining protein turnover rates

Under normal conditions, cells actively degrade and replace their inventory of proteins on a continuous basis. This process happens at distinct rates for different proteins (Pratt et al., 2002). The modern method of choice for measuring proteome-wide turnover rates is termed *pulsed SILAC* (Schwanhäusser et al., 2011). As the name indicates, it exploits properties of the metabolic labeling strategy SILAC. This is done by initially culturing cells in *light* medium, i.e., common isotopes of the amino acids lysine and arginine, followed by a *pulse labeling*, i.e., changing the culture media to *heavy*, meaning that all contained essential amino acids lysine and arginine feature heavy carbon isotopes. When cells are now harvested at different time points after the medium change and proteins are extracted and measured by MS, proteins containing light and heavy amino acids can be distinguished due to a shift in m/z . The temporal change in intensity ratio between light to heavy-labeled proteins can then be used to compute protein turnover rates (inverse: protein half-life) (Mathieson et al., 2018; Schwanhäusser et al., 2011).

Measuring protein-protein interactions

Most cellular processes are orchestrated by dynamically interacting proteins or complexes consisting of multiple proteins, which are stably associated to perform multi-faceted tasks. Thus, for many years, there has been a strong interest in studying protein-protein interactions (PPIs) and their functions. A classical approach is the yeast two-hybrid method,

which uses a split transcription factor (TF) regulating the expression of a reporter gene which only works if the two TF domains come together mediated by a PPI between a bait and a prey protein (Chien et al., 1991).

Mass spectrometry-based approaches first were introduced by taking the Western blot-based co-immunoprecipitation, which can detect an interaction between two proteins with suitable antibodies against both interactors (Phizicky & Fields, 1995), to an unbiased level enabling the identification of system-wide PPIs with bait proteins (Ewing et al., 2007; Gavin et al., 2002). Other proteomics-based methods have been developed more recently that either make use of promiscuous modification of proteins in close proximity to a bait protein fused to biotin ligase (BioID) (Roux et al., 2012) or are based on co-elution patterns of proteins when cell lysates are fractionated with size exclusion chromatography (SEC) (Dong et al., 2008; Heusel et al., 2019).

In recent years, it has been realized that due to the stoichiometric abundance of protein complex members, protein abundance measurements across different samples and perturbations also allow to recapitulate annotated PPIs and protein complexes and even can allow to discover new interactions (Ori et al., 2016). Similarly, we have been able to show that the same holds true for protein turnover, i.e., subunits of protein complexes are turned over at a rate more similar than expected by chance (Mathieson et al., 2018).

Biophysical methods to study protein-ligand interactions

Detection of proteins bound by ligands is an important challenge in biomedical but also basic research. It is crucial for understanding the regulation of fundamental biological processes and functions of associated proteins, but also especially in the context of drug discovery, where there is a need to rationalize drug effects by determining which molecular targets and potentially off-targets are engaged by a molecule of interest (Simon et al., 2013).

One of the first biophysical proteomics methods to approach this problem translated an

assay termed Stability of Proteins from Rates of Oxidation (SPROX) (West et al., 2008) to a proteome-wide scale using MS (West et al., 2010). This technique makes use of chemical denaturation of proteins in the presence of hydrogen peroxide which leads to oxidation of the protein in a denaturant dose-dependent manner. This process can be used to deduct the thermodynamics of proteins' denaturation and their modulation in the presence of a ligand (West et al., 2008). Limitations of this approach are that the observation of protein denaturation is limited to putative oxidation sites and that it can only be performed in very specific chemical conditions which are very different to the intracellular milieu.

A different approach is taken by methods such as Drug Affinity Response Target Stability (DARTS) (Lomenick et al., 2009) and Limited Proteolysis coupled to mass spectrometry (LiP-MS) (Feng et al., 2014). These methods are based on the principle that incubation of proteins with an unspecific protease, such as Proteinase K, will lead to a characteristic cleavage pattern, since the most accessible peptide bonds will be most likely to be cleaved. If a protein undergoes conformational change or is bound by a ligand this can be reflected in a change of its characteristic cleavage pattern, since certain cleavage sites might be freed up or blocked by such an event (Feng et al., 2014; Lomenick et al., 2009). The strength of this technology is that it gives hints on which sites of the protein are affected by a conformational change of ligand-binding. However, due to the unspecific protease digestion the associated database search becomes increasingly difficult with the complexity of the proteome this technique is applied to. Also these approaches are limited to cellular lysates and do not inform on *in situ* events.

The most recently developed technology which applies biophysical proteomics to detect protein-ligand interactions is called Thermal proteome profiling (TPP) (Savitski et al., 2014). TPP works by implementing the Cellular Thermal Shift Assay (CETSA) (Martinez Molina et al., 2013) on a proteome-wide level using TMT-labeling multiplexed MS (Franken et al., 2015; Savitski et al., 2014). In the original version of the method, cells are cultured in two different conditions, e.g., the presence of absence of a drug. The cells from both conditions are split into 10 aliquots and heated to a temperature range

between 37 and 65°C (for human samples) for 3 minutes. Subsequently, aggregating proteins are removed by centrifugation or filtration and the remaining soluble proteins are digested with trypsin and all aliquots per conditions and replicate are labeled with one set of TMT reagents, subjected to sample preparation and analyzed by LC-MS/MS (Figure 1.5) (Franken et al., 2015). Thereby, the method generates accurate, proteome-wide denaturation curves (also referred to as melting curves) as a function of temperature (temperature range TPP; TPP-TR) which can be used to compare, e.g., vehicle and drug treated cells. By comparison of melting curves of individual proteins in different conditions, thermal shifts can be used to infer ligand-protein engagement (Figure 1.5) (Childs et al., 2019; Franken et al., 2015; A. Mateus, Kurzawa, et al., 2020). A key difference compared with the methods described above, is that TPP can be performed on intact cells (Savitski et al., 2014) and meanwhile has been adapted also to intact tissues (Perrin et al., 2020). Additionally, the method can also be used to derive ligand dose-response thermal stability curves for all proteins at one temperature (ideally chosen as a temperature at which many proteins partly, but not completely unfold). This approach is termed Isothermal Compound Concentration Range TPP (TPP-CCR) (Franken et al., 2015; Savitski et al., 2014). It has the advantage that proteins, which require different doses of a compound to be affected, can be monitored, at the cost of not being able to detect effects on proteins, which either are fully denatured or not denatured at all, at the chosen temperature (A. Mateus, Kurzawa, et al., 2020).

The combination of both variants, TPP-TR and TPP-CCR, is realized in an approach termed 2D-TPP (Becher et al., 2016). By combining separate MS runs for two consecutive temperatures in which cells were treated with each n different compound concentrations, proteome thermal stability is measured as a function of both temperature and ligand concentration (Figure 1.6).

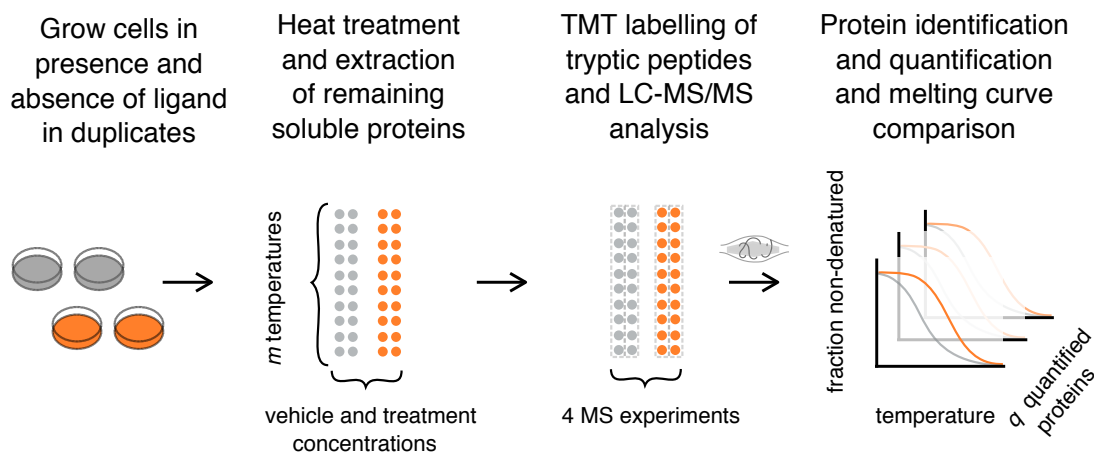


Figure 1.5: Illustration of the experimental TPP-TR workflow. Cells are grown in multiple replicates of two different conditions, e.g. the presence or absence of a compound. Each of the replicates is then divided into m aliquots and subjected to a short heat treatment at a distinct temperature (range depending on the organism used in the experiment). Cells are then lysed and remaining soluble proteins are then extracted by precipitating cell debris and denatured proteins through centrifugation or by microfiltration. Obtained proteins are then digested and labeled with TMT, before samples of each replicate are pooled and analyzed by LC-MS/MS. Proteins are identified by database search and quantitative data is analyzed by comparison of melting curves. While this approach could successfully be applied to detect (off-) targets in human cells of the pan-HDAC inhibitor Panobinostat (Becher et al., 2016) and the Bromo- and Extra-Terminal (BET) domain inhibitor JQ1 (Savitski et al., 2018) using bespoke thresholds, objectively determining which thermal proteome profiles are indicative of target engagement still remains challenging.

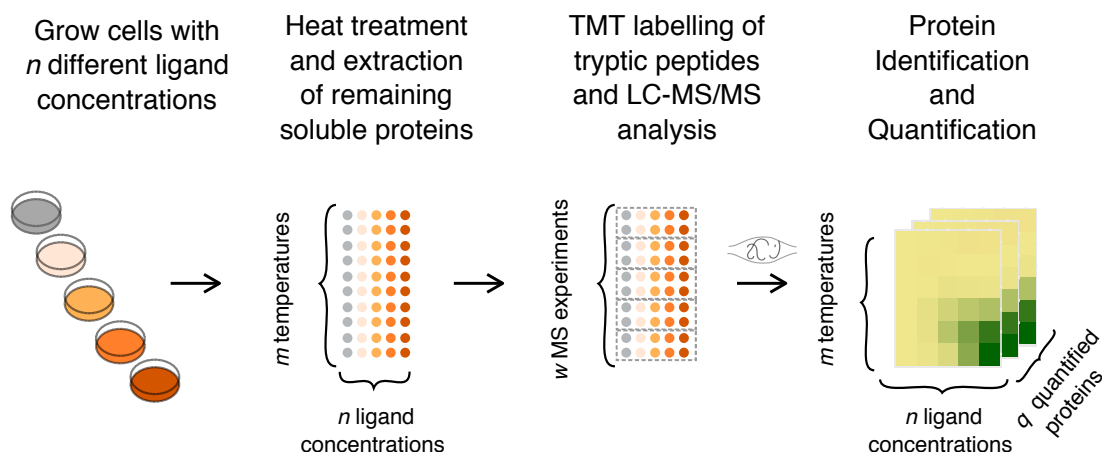


Figure 1.6: Illustration of the experimental 2D-TPP workflow. Cells are grown in the presence of n different ligand concentrations including a solvent-only condition. Each of the samples containing a specific ligand concentration is then divided into m aliquots and subjected to a short heat treatment at a distinct temperature (range depending on the organism used in the experiment). Cells are then lysed and remaining soluble proteins are then extracted by precipitating cell debris and denatured proteins through centrifugation or by microfiltration. Obtained proteins are then digested and labeled with TMT so that all conditions at two consecutive temperatures are multiplexed. All obtained samples are measured in w MS experiments. After identification and quantification, for each protein a $n \times m$ data matrix is obtained, which can contain non-randomly missing values preferentially at higher temperatures.

Lately, the 2D-TPP technology has been expanded to accommodate also the profiling of continuous or discrete cell state perturbations (Becher et al., 2018; A. Mateus, Hevler, et al., 2020; Selkrig et al., 2020). Such approaches enable the orthogonal readout of protein stability in addition to protein abundance and can thus reflect cell state changes, e.g., metabolite levels or PPIs (Becher et al., 2018; A. Mateus, Hevler, et al., 2020).

1.3 Statistical methods to analyze genome scale data

The statistical analysis of a genome-scale experiment typically involves the comparison of characteristics of many–hundreds to hundreds of thousands–genomic features between two or more groups. If one treats these comparisons as k individual tests one could consider to use hypothesis tests, such as the t -test for comparison on individual features between two groups, or an analysis of variance (ANOVA) in the case of a multi-group comparison (Figure 1.7a and b). The Welch two sample t -test compares the means of two distributions by accounting for their variances:

$$t = \frac{\bar{x}_1 - \bar{x}_2}{\sqrt{\frac{s_1^2}{n_1} + \frac{s_2^2}{n_2}}} \quad (1.1)$$

(Welch, 1947). By determining the degree of freedom of the associated t -distribution, which can be computed based on the standard deviations $s_{1/2}$ and number of observations $n_{1/2}$ of both distributions, one can obtain a p -value associated with an observed t -statistic. The ANOVA (Fisher, 1918) for comparing data obtained from more than two individual groups or conditions works by comparing two scenarios: 1) Observed data is treated as obtained from one group, the overall mean is determined and the residual sum of squares (RSS) is determined as the sum of squared errors of all data points from the overall mean. We denote it here as $\text{RSS}^{(0)}$ since it refers to the null hypothesis of no observed group difference (also referred to as total sum of squares). 2) The data is divided into different conditions and group-specific mean estimates are obtained. The sum of squared errors from the mean of all individual groups are then computed and summed to obtain $\text{RSS}^{(1)}$. Since $\text{RSS}^{(1)}$ retains less degrees of freedom, by using several mean estimates compared to one mean estimate used to determine $\text{RSS}^{(0)}$, $\text{RSS}^{(1)} \leq \text{RSS}^{(0)}$. An F -statistic can then be constructed with:

$$F_i = \frac{\text{RSS}_i^{(0)} - \text{RSS}_i^{(1)}}{\text{RSS}_i^{(1)}} \frac{d_2}{d_1}. \quad (1.2)$$

Here, d_1 describes the difference in retained degree of freedom (DOF) between the null and alternative hypothesis, e.g. if one overall mean estimate is compared with three group-specific means $d_1 = 2$. On the other hand d_2 represents the DOF under the alternative

hypothesis, i.e. $d_2 = n - \nu_1$, with n representing the total number of observations and ν_1 describing the number of groups accounted for under the alternative hypothesis. Through comparison of the obtained F -statistic with the F_{d_1, d_2} -distribution a corresponding p -value can be obtained. The obtained p -value is then indicative of whether there is evidence for a difference in the means of the groups. To identify which of the groups differ in means, a post-hoc test may be performed, such as the Tukey procedure which works similar to performing a t -test between all pairs of groups and subsequently adjusting obtained p -values for multiple testing (Tukey, 1949).

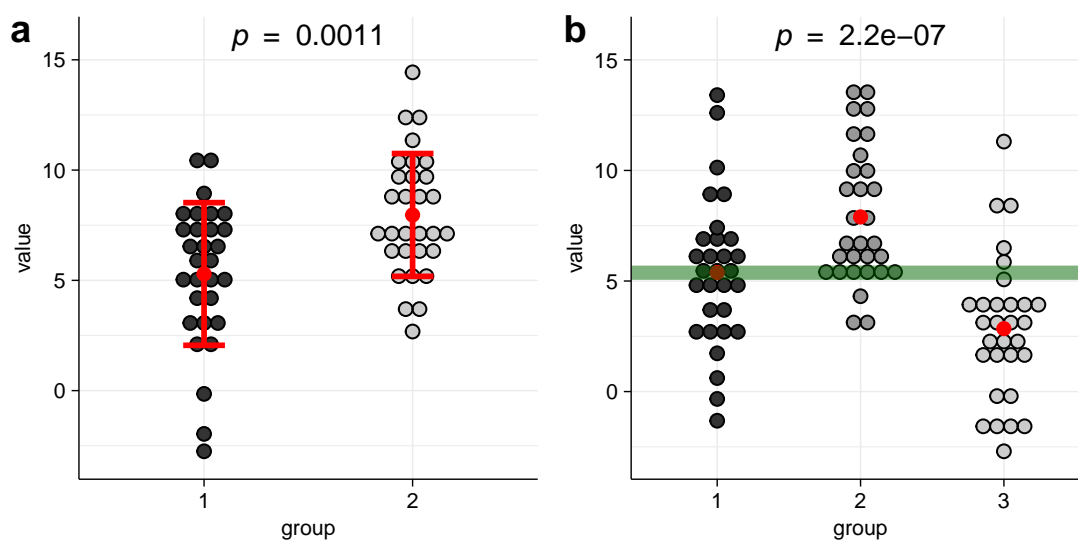


Figure 1.7: Illustration of the t -test and the ANOVA. a) The t -test compares the means (red dots) of samples obtained from two groups while accounting for their variances and number of observations. b) The ANOVA assesses how much lower the sum of obtained variances is, when mean estimates are computed per group (red dots) versus a mean estimate across all data points (green line).

However, these approaches lack flexibility to accommodate complex covariate structures, such as confounding factors and batch effects. Thus, linear models, which can consider multiple variables at the same time and test for significance of all of them simultaneously, are the preferred choice for genome-scale differential testing.

1.3.1 Linear models for differential analysis

In general terms, a linear model describes a *response variable* y_i as a linear combination, i.e., a weighted sum, of one or more *explanatory variables* $\{x_{i,1}, x_{i,2}, \dots, x_{i,n}\}$. This can be expressed as

$$y_i = \sum_k x_{i,k} \beta_k + \epsilon_i \text{ with } \epsilon_i \sim \mathcal{N}(0, \sigma^2). \quad (1.3)$$

The parameters β_k represent the weights of the different explanatory variables which are summed. These parameters are typically obtained by maximum likelihood estimation (MLE) which is in the case of Eq. 1.3 equivalent to minimizing $\sum_i \epsilon_i^2$ using ordinary least squares.

The advantage of linear models over two-sample hypothesis tests is exemplified in Figure 1.8. While the hypothesis test finds a significant difference in the means of both groups, the linear model is able to dissect that the mean differences in the two groups is due to a bias in covariate distribution, a so called *confounding variable*, but that there is no significant effect of the group variable, i.e., the intercept of the two linear models per group is more or less the same.

Linear models are not only applicable to normally distributed data as in the example. The concept of *generalized linear models* enables to similarly fit, e.g., count data, by introducing a link function which allows to perform MLE on a transformed scale (Holmes & Huber, 2018).

1.3.2 Empirical Bayes methods

The branch of statistics named after Thomas Bayes follows a different approach to data interpretation compared to frequentist statistics. Essential to Bayesian statistics is the incorporation of prior knowledge or beliefs in data analysis. In the case of linear regression for example, Bayesian inference would use MLE, which is also common in frequentist statistics, but moderate the estimated parameters by a *prior probability distribution* to obtain a *posterior distribution* of the parameters (Bishop, 2006). In many cases, how-

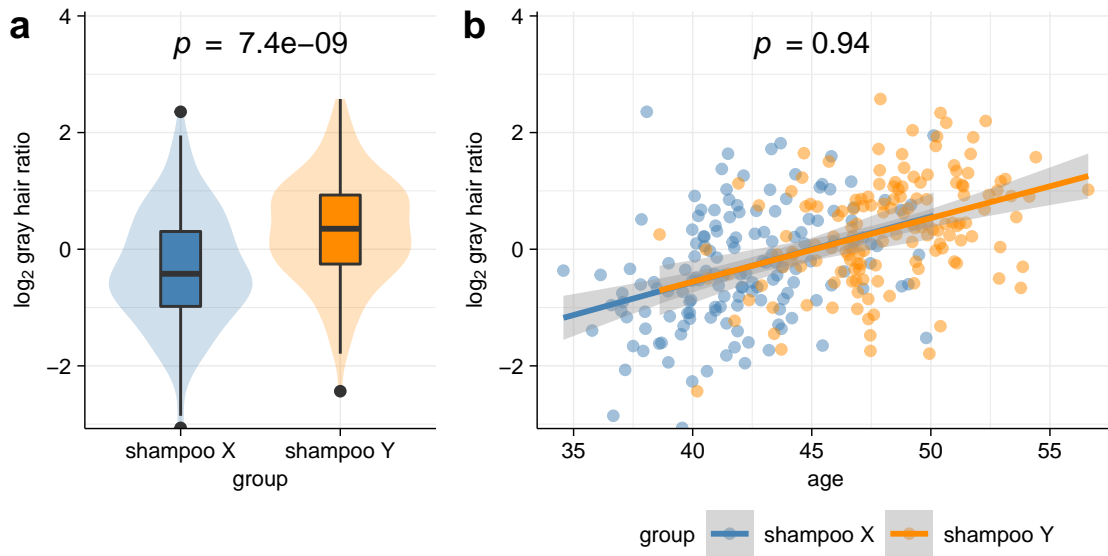


Figure 1.8: Illustration of how linear models can account for covariate structure. Example in which the effect of two different shampoos on the fraction of gray hair is measured. a) While the t -test finds a significant difference between the means of both groups, the linear model (b) infers the trend of higher fraction of gray hair with age and finds no difference in the intercepts of both groups. Age is a confounding variable in this analysis and the difference in group means observed in a) is due to a difference in mean age, but not due to a difference in mean fraction of gray hair.

ever, justifying a certain choice of the prior distribution is challenging. This problem is addressed in the *empirical Bayes* approach, which especially finds application in genome-scale experiments in which empirically determined variances across all genes or those of a certain group are used to moderate those estimated for individual genes based on few replicates (Efron, 2010).

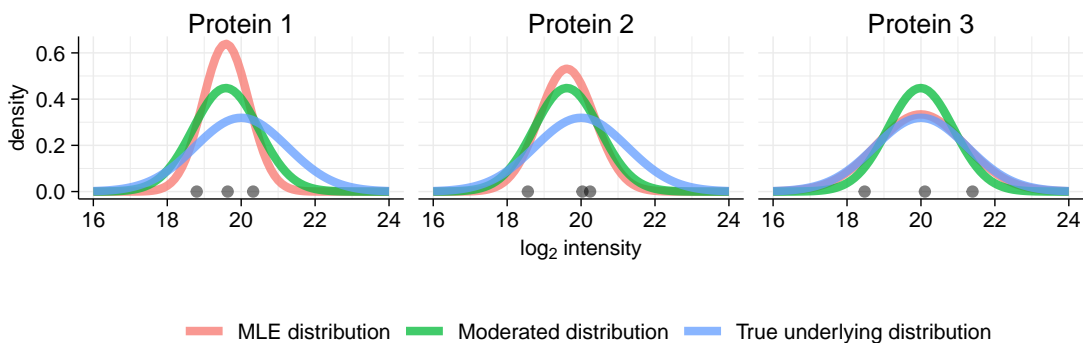


Figure 1.9: Empirical Bayesian variance estimation by sharing of information across proteins. Data on the abundance levels of three different proteins is obtained, which are taken to come from the same true underlying distribution (blue). Maximum likelihood estimation of the distribution (red) underestimates the true variance, especially for Protein 1. The empirically moderated distributions (green) less severely underestimate the true variance.

The R/Bioconductor software package `limma` implements this approach for analysis of microarray data (Ritchie et al., 2015). However, since proteomics data similarly represents log-transformed intensity signal, the package is often applied also for differential analysis of proteomics datasets (Kammers et al., 2015).

1.3.3 Statistical analysis of TPP experiments

Since different experimental designs of TPP experiments were developed, distinct methods to accommodate respective data were suggested in the last years. A common aspect of these methods is that they all fit sigmoid curves:

$$\mu(x) = c + \frac{d - c}{1 + \exp(b(x - a))}, \quad (1.4)$$

where x can either be the temperature to model a melting curve, or x can represent the compound concentration such as for TPP-CCR or 2D-TPP experiments in which dose response stabilization curves are estimated. Note: originally a slightly different sigmoid

formula was suggested, which is directly derived from denaturation thermodynamics (Brandts, 1964), however these models are equivalent and interpretation of parameters for Eq. 1.4 is more intuitive. The parameter a is the inflection point, b is the slope, c corresponds to the plateau and d is the upper limit.

Comparison of melting curves

The first method to determine thermal shifts from TPP-TR experiments is based on melting point T_m comparisons between two conditions using $\mu(T_m) = 0.5$ (Figure 1.10a) (Savitski et al., 2014). In order to accept parameter estimates for testing on melting points, the fit should fulfill $R^2 \geq 0.8$ and the plateau $c \leq 0.2$. For proteins with accepted fits, measured in at least two replicates in both conditions, $\Delta T_m = T_m^{\text{treat.}} - T_m^{\text{ctrl.}}$ are computed, ΔT_m -values are z -transformed per replicate and converted into p -values. Obtained p -values from within one replicate are adjusted for multiple testing. Proteins are considered significantly thermally shifted between the compared conditions if the ΔT_m of two replicates is associated with $p_{\text{adj.}} < 0.1$.

More recently, a method by Childs et al. (2019) has been suggested, which is termed Nonparametric Analysis of Response Curves (NPARC). The main motivation for this approach, is the fact that by aggregating the observed data to a summary parameter, such as the melting point, only a small fraction of the observed data is used for analysis. This limits the discovery of thermal shifts of proteins for which T_m can be determined and for which the thermal shift is apparent in a temperature close to T_m . NPARC works by fitting two nested models to the melting curve of each protein. First, the *null model* (Figure 1.10b) which does not distinguish between treatment conditions, then an *alternative model* (Figure 1.10c) which fits a melting curve for each treatment condition separately. By comparing the RSS of both models ($\text{RSS}^{(0)}$ for the null model and $\text{RSS}^{(1)}$ for the alternative model) and determining the respective DOFs of both models, an F -statistic can be computed (Eq. 1.2).

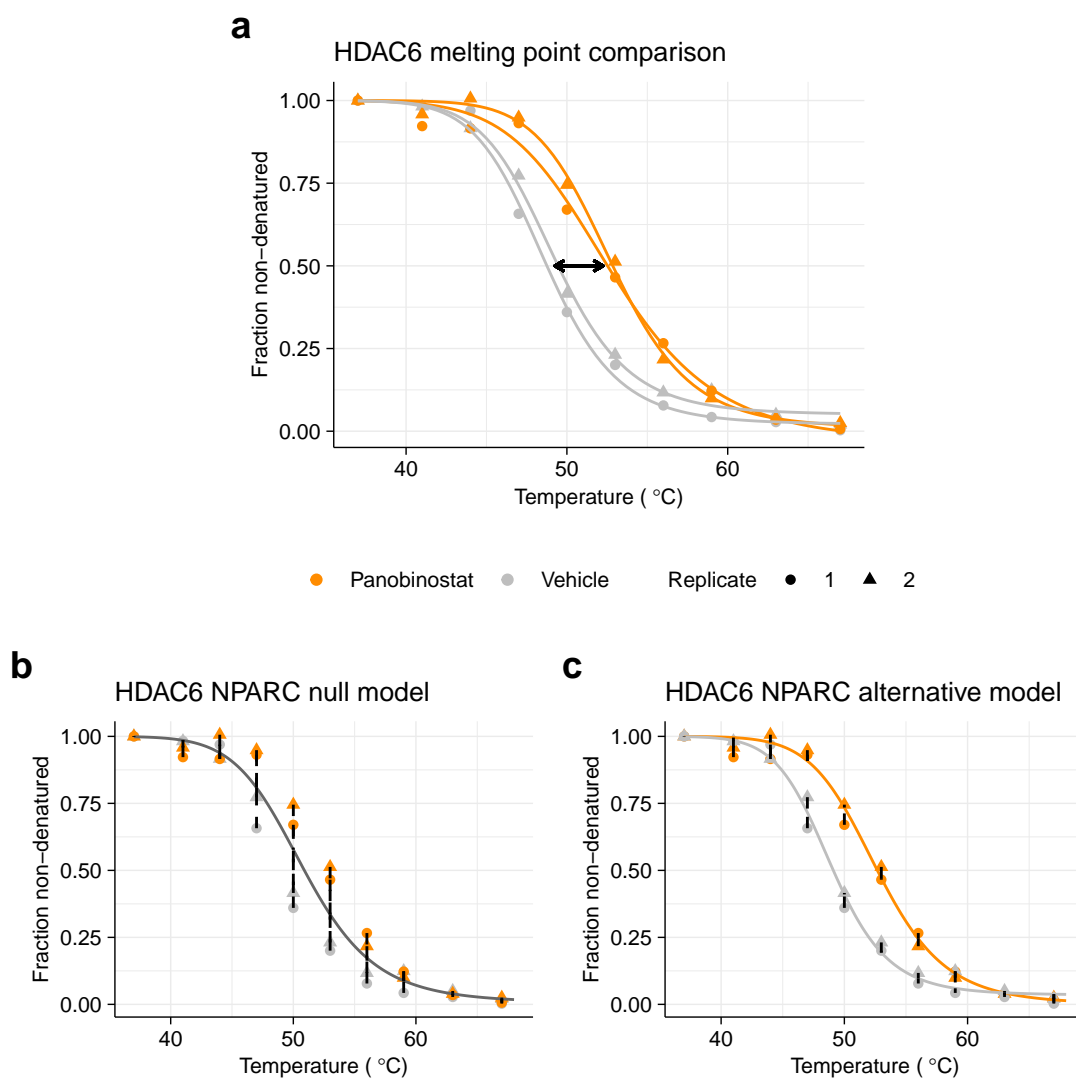


Figure 1.10: Analysis strategies for TPP-TR experiments. a) ΔT_m -based comparison by fitting of sigmoid melting curves per condition and replicate and comparison of z -scores. b,c) Curve-centric analysis of TPP-TR data, by deriving an F -statistic based on the residuals sum of squares of a null (b) and an alternative model (c) and comparison with an empirical null distribution.

The obtained distribution of F -statistics is, however, not correctly described by the theoretically derived DOFs, since in practice residuals are correlated and heteroscedastic and not independently and identically distributed as theoretically assumed. Thus, NPARC offers a method for determining an empirical null distribution to obtain well calibrated p -values for obtained F -statistics (Childs et al., 2019).

Analysis of 2D-TPP data

The first proposed analysis of 2D-TPP datasets (Becher et al., 2016) was inspired by the analysis of TPP-CCR experiments (Franken et al., 2015). This includes fitting a simplified sigmoid dose response curves to relative fold changes, which were transformed into a space where the thermal stability of a protein measured at the lowest ligand dose was forced to 0 and the highest to 1, with:

$$f(x) = \frac{1}{1 + 10^{b(a-x)}}, \quad (1.5)$$

with a representing the inflection point and b the slope (Franken et al., 2015). A TPP-CCR curve of a protein is accepted to be associated with a dose-dependent stabilization (or destabilization if $b < 0$) if $R^2 \geq 0.8$ and the non-transformed relative fold change $r_{c_{\max}} \geq 1.5$ at the highest ligand concentration condition compared to the vehicle condition.

In the case of 2D-TPP, this method is applied to within temperature transformed values for each temperature separately. It is then asked for a (de-)stabilization pattern, according to the same thresholds, to be observed at two consecutive temperatures. Figure 1.11 shows how this is done for HDAC6 for a 2D-TPP dataset profiling panobinostat. However, compared to the TPP-CCR setting in which curves are fitted to ten data points in replicates, in 2D-TPP analysis, DR curves are fitted to as few as five data points of which even the lowest and highest concentration one are fixed to either 0 or 1. This leads to surprisingly high R^2 values even for poor fits (Figure 1.11) and thus bears the risk of overinterpretation of such fits. Moreover at the same time, the fixed thresholds

inherently limited sensitivity of the approach and there is no possibility for controlling or adjusting the FDR associated with determined hits.

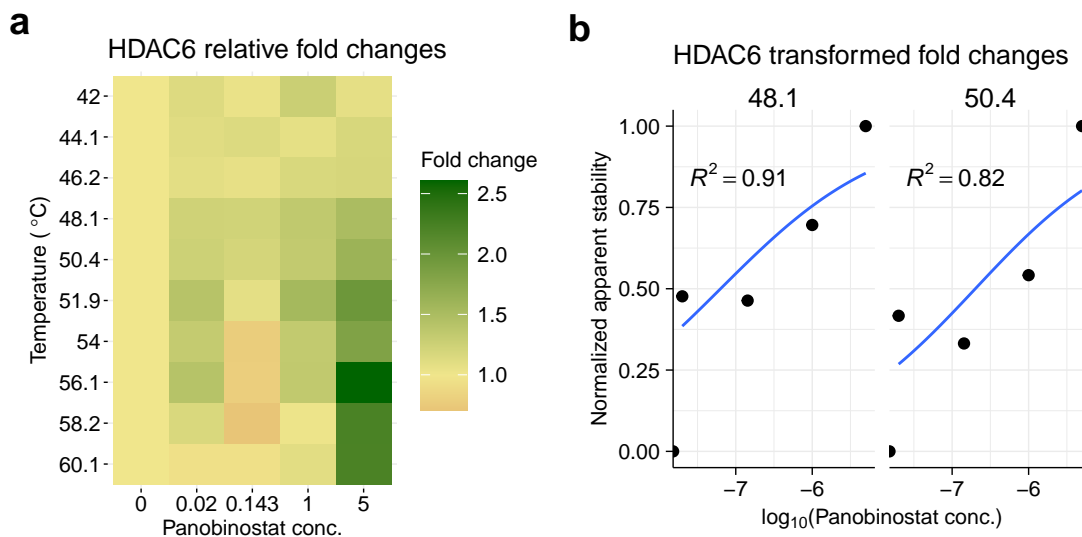


Figure 1.11: Analysis strategy for 2D-TPP experiments. a) Heatmap of relative fold changes at individual temperatures measured for HDAC6 in the presence of different concentrations of Panobinostat. At several consecutive temperature the fold change cutoff of 1.5 is surpassed including the temperatures 48.1 and 50.1. b) Sigmoid dose-response fits to transformed thermal stability fold changes of HDAC6 measured at the temperatures 48.1 and 50.1. The protein is accepted as thermally stabilized by Panobinostat since for both fits $R^2 > 0.8$ and at both temperatures $r_{c_{\max}} \geq 1.5$.

Chapter 2

Materials and Methods

2.1 Software and required packages

If not stated otherwise, all analyses presented in this work were implemented using the R language (R Core Team, 2020). Table 2.1 summarizes details on version and environment used. All R packages used in this thesis are summarized in Table 2.2. All plots were made using the `ggplot2` R package (Wickham, 2016) and arranged using `cowplot` (Wilke, 2019).

Table 2.1: R environment and session info

Setting	Value
version	R version 4.0.0 Patched (2020-05-04 r78358)
os	macOS Mojave 10.14.6
system	x86_64, darwin17.0

Table 2.2: Summary of R packages and their versions

Package	Version	Package	Version
AnnotationDbi	1.50.0	NPARC	1.1.1
bibtex	0.4.2.2	org.Hs.eg.db	3.11.4
Biobase	2.48.0	phosphoTPP	0.1.0
BiocGenerics	0.34.0	pROC	1.16.2
BiocParallel	1.22.0	purrr	0.3.4
bookdown	0.19	RColorBrewer	1.1-2
clusterProfiler	3.16.0	readr	1.3.1
cowplot	1.0.0	readxl	1.3.1
devtools	2.3.0	rmarkdown	2.2
dplyr	1.0.0	Rtpca	1.1.1
drc	3.0-1	S4Vectors	0.26.1
forcats	0.5.0	sna	2.6
GGally	2.0.0	statnet.common	4.4.1
ggplot2	3.3.2	stringr	1.4.0
ggsignif	0.6.0	tibble	3.0.1
heididown	0.1.0	tidyr	1.1.0
here	0.1	tidyverse	1.3.0
IRanges	2.22.2	TPP	3.17.0
kableExtra	1.3.1	TPP2D	1.7.3
knitr	1.28	tufte	0.6
limma	3.44.1	usethis	1.6.1
magrittr	1.5	viridis	0.5.1
MASS	7.3-51.6	viridisLite	0.3.0
network	1.16.1	vsn	3.56.0

2.2 Publicly available datasets used in this work

All publicly available datasets used in this work are summarized in Table 2.3.

2.3 Experimental methods

Note: All wet-lab experiments were performed by my colleagues who are acknowledged in the respective method descriptions.

2.3.1 Thermal proteome profiling (TPP)

TPP in *Escherichia coli*

Cultures of *Escherichia coli* strain BW25113 were grown in lysogeny broth (LB, Lennox, Sigma Aldrich, ID: L3022) overnight at 37°C and diluted 1:100 into a volume of 20 ml LB. Bacteria were grown aerobically with shaking at 37°C until an optical density of 0.5 at 578 nm (OD_{578}). Obtained cells were spun down through centrifugation for 5 min at $4,000 \times g$, washed with 10 ml phosphate buffered saline (PBS, 2.67 mM KCl, 1.5 mM KH_2PO_4 , 137 mM NaCl, and 8.1 mM NaH_2PO_4 , pH 7.4), re-suspended in PBS to an OD_{578} of 10 and 100 μ l were transferred into wells of a polymerase chain reaction (PCR) plate (Sigma Aldrich, ID: BR781378-50EA). The plate was centrifuged for 5 min at $4,000 \times g$ and 80 μ l were removed before the plate was subjected to a temperature gradient (37-87°C) in a PCR machine (Agilent SureCycler 8800) for 3 min and then incubated for 3 min at room temperature. Cell lysis was done by incubation with 30 μ l lysis buffer consisting of PBS with 50 μ g/ml lysozyme (Sigma Aldrich, ID: L687), 250 U/ml benzonase (Sigma Aldrich, ID: 9025-65-4-E8263), protease inhibitor (Roche, Sigma Aldrich, ID: P8340), 0.8% NP-40 and 1 mM $MgCl_2$ while shaking at room temperature for 20 min.

Table 2.3: Overview of publicly available datasets used in this work.

Dataset	URL	Reference
2D-TPP of JQ1 in intact HL60 lysate	http://dx.doi.org/10.1016/j.cell.2018.02.030	Savitski et al. 2018
2D-TPP of Panobinostat in intact HepG2 cells	http://dx.doi.org/10.1038/nchembio.2185	Becher et al. 2016
Annotation of human protein complexes	https://doi.org/10.1186/s13059-016-0912-5	Ori et al. 2016
D2P2 database: Predicted disorder in human proteins	http://http://d2p2.pro	Oates et al. 2013
EcoCyc database: protein complexes in <i>E. coli</i>	https://ecocyc.org	Keseler et al. 2017
Functional phosphosite score	http://doi.org/10.1038/s41587-019-0344-3	Ochoa et al. 2020
Hotspot thermal profiling data	https://doi.org/10.1038/s41592-019-0499-3	Huang et al. 2019
Meltome atlas	http://meltomeatlas.proteomics.wzw.tum.de:5003	Jarzab et al. 2020
Proteome isoelectric point database	http://http://isoelectricpointdb.org	Kozlowski et al. 2017
STEPdb 2.0: <i>E. coli</i> subcellular protein localization	https://stepdb.eu	Loos et al. 2019
STRINGdb: PPI database	http://string-db.org	Szklarczyk et al. 2019
TPP-TR of G1/S vs. M in HeLa cells	http://dx.doi.org/10.1016/j.cell.2018.03.053	Becher et al. 2018

This was followed by three cycles of freezing in liquid N₂ and thawing for 1 min at 25°C with subsequent vortexing. The PCR plate was then centrifuged for 5 min at 2,000 × g to pellet cell debris and the retained supernatant was filtered for 5 min at 500 g through a 0.45-µm 96-well filter plate (Millipore, ID: MSHVN4550) to remove residual protein aggregates. The filtrate was mixed 1:1 with sample buffer containing 180 mM Tris pH 6.8, 4% SDS, 20% glycerol and 0.1 g bromophenol blue and processed for MS/MS analysis. These experiments were performed by André Mateus (Mateus et al., 2018).

2D-TPP of PCI-34051 and BRD-3811 in HL60 cells

HL60 cells (DSMZ, ID: ACC 3) were cultured in Iscove's modified Dulbecco's medium (IMDM, GIBCO) with 10% fetal bovine serum (FBS). Cells were treated with 0, 0.04, 0.29, 2, 10 µM PCI-34051 (Sellekchem) or BRD-3811 (synthesized in-house) for 90 min at 37°C and 5% CO₂. Samples treated with each drug concentrations were split into 12 aliquots which were each heated at a different temperature in the range of 42-63.9°C for 3 min and subsequently set to room temperature for another 3 min. Then, samples were each lysed in 30 µl PBS supplemented with protease inhibitors and 0.67% NP-40, which was cooled on ice previous to lysis. Cells were frozen in liquid N₂ for 1 min followed by a short thawing step in a metal block at 25°C before being placed on ice and resuspended by pipetting. This was followed by an incubation of samples with 25 U benzonase per ml for 60 min at 4°C and subsequent centrifugation at 100,000 g for 20 min at 4°C. Finally, 30 µl of supernatant of each sample were transferred into a new tube and subjected to sample preparation for MS analysis. These experiments were performed by Isabelle Becher (Kurzawa, Becher, et al., 2020).

2D-TPP of ATP and GTP in Jurkat crude lysate

Jurkat E6-1 cells (ATCC, ID: TIB-152) were grown in Roswell Park Memorial Institute medium (RPMI, GIBCO) with 10% FBS, harvested and washed with PBS. Cells were pelleted by centrifugation at 1000 x g for 3 min and resuspended in 10-times the volume

of the pellet of PBS supplemented with protease inhibitors and 1.5 mM MgCl₂. The obtained suspension was then lysed through mechanical disruption by 20 strokes with a Dounce homogenizer. Protein concentration was adjusted to 3.5 mg/ml. Retrieved crude lysates were treated with 0, 0.005, 0.05, 0.5, and 2 mM NaATP or 0, 0.001, 0.01, 0.1, and 0.5 mM for NaGTP for 10 min at room temperature. Samples treated with each metabolite concentration were divided into 12 portions and each heated to a different temperature in the range of 42-63.9°C for 3 min. After 3 min at room temperature, protein aggregates were removed using ultracentrifugation at 100,000 × g for 20 min at 4°C. 30 µl of supernatant were transferred into a fresh tube for each sample and preparation for MS/MS analysis was performed. These experiments were performed by Sindhuja Sridharan (Sridharan et al., 2019).

2D-TPP of Vemurafenib and Panobinostat in rat tissue lysates

Rat spleen punch pieces were distributed over 48-well plates (two per well) with 600 µl of Dulbecco's modified Eagle's high glucose medium (Thermo Fisher Scientific, ID: 11965118), supplemented with 10% FBS, 10 mM HEPES (Thermo Fisher Scientific, ID: 15630056), 100 U/ml penicillin-streptomycin (Thermo Fisher Scientific, ID: 15140122) and 4.5 g/l L-glutamine. Spleen punches were then treated with different doses of Panobinostat (50, 5, 0.5 and 0.05 µM) at 37°C and 5% CO₂ for 2.5 h and were then transferred to a 96-well PCR plate with 100 µl of PBS supplemented with protease inhibitors and the respective Panobinostat concentrations.

Testis were weighed into 96-well cell culture plates with 150 µl of the same medium as for the spleen punches. Subsequently, the testis pieces were treated with different doses of Vemurafenib (40, 10, 2 and 0.4 µM) at 37°C and 5% CO₂ for 1.5 h, and were then transferred to a 96-well PCR plate, briefly centrifuged and remaining medium was discarded. A volume equivalent to the volume of the testis pieces of PBS supplemented with protease inhibitors and the respective Vemurafenib concentrations was added to each well. Samples from both tissues were then simultaneously heated to one of 12 temperatures

covering the range from 42-64°C for 3 min and then processed as described 2D-TPP experiments above.

2D-TPP of Panobinostat and JQ1 in human blood

Human blood was obtained from donations of healthy volunteers at the Institute for Clinical Transfusion Medicine and Cell Therapy in Heidelberg. 1.5-2 ml of freshly acquired heparinized blood samples were treated with 0, 0.02, 0.143, 1, and 5 μ M of Panobinostat or 0, 0.4, 2, 10, and 40 μ M of JQ1 for 1.5 h at 37°C and CO₂. Protease inhibitors were added and treated samples were transferred onto a PCR plate such that each treatment condition could be heated to 10 different temperatures (range of 44-54°C) for 3 min using the gradient-heating function of a PCR machine followed by incubation at room temperature for 3 min. Primary blood mononuclear cells (PBMCs) were obtained by density centrifugation at 1,000 \times g at room temperature for 10 min using SepMate-15 Tubes (STEMCELL, ID: 85420) and Lymphoprep density gradient medium (STEMCELL, ID: 07811) and RosetteSe Human Granulocyte Depletion Cocktail (STEMCELL, ID: 15624). Retrieved PBMCs were washed with PBS with protease inhibitors and then resuspended and the buffer was supplemented with 0.8% NP-40, 1 kU/ml benzonase and 1.5 mM MgCl₂ before incubation at 4°C for 1 h. Samples were then centrifuged at 4°C for 3 min at 500 \times g. Insoluble aggregates were removed by filtering the samples through a 384-filter plate (Thermo Fisher Scientific, ID: 10675743) and subsequently further processed for MS/MS analysis. These experiments were performed by Jessica Perrin, Thilo Werner and Anna Rutkowska (Perrin et al., 2020).

TPP experiments of in S9 rat liver lysate

Male Wistar rat liver S9 (BioIVT, ID:M00022) was used at a concentration of 2 mg/ml and treated with 10 or 100 μ M Panobinostat or one of its metabolites or with 0.4 mM NADP. Samples were simultaneously heated to 37, 47.7, 51.1, 54.2, 57.2 or 60.7°C for 3 min and then rested at room temperatures for 3 min. Cell lysis was then performed with

0.8% NP-40, supplemented with 1.5 mM MgCl₂ and 1 kU/ml benzonase at 4°C for 1 h. Protein aggregates were pelleted by ultracentrifugation at 100,000 × g for 20 min and removed, and remaining soluble samples were further processed for LC-MS/MS analysis. These experiments were performed by Jessica Perrin and Thilo Werner (Perrin et al., 2020).

2.3.2 Solubility proteome profiling (SPP) experiments

Crude lysates of Jurkat cells were prepared as described in Section “2D-TPP of ATP and GTP in Jurkat crude lysate” and split into 10 portions. Two of the aliquots were used as vehicle-treated controls, the other eight were treated for 10 min at room temperature with a range of concentrations (0.1, 0.5, 1, 2, 4, 5, 8 and 10 mM) of a small molecule (MgATP, MgAMP-PNP or MgGTP), followed by an incubation at 37°C for 3 min. NP-40 was added to one of the control and to the eight small molecule treated samples to a final concentration of 0.8%. Sodium dodecyl sulfate (SDS) was added to the other control sample to a final concentration of 1%. All 10 aliquots were then treated with 25 U benzonase per ml at 4°C for 60 min and insoluble proteins were subsequently removed by ultracentrifugation at 100,000 × g for 20 min at 4°C and discarding of pellets. Experiments were conducted by Sindhuja Sridharan (Sridharan et al., 2019).

2.3.3 ATP depletion and in-cell SPP

Jurkat cells were treated with two doses D1 and D2 of 2-deoxyglucose (2DG) dissolved in water and Antimycin-A dissolved in 96% ethanol. After washing with PBS, Jurkat cells were resuspended in RPMI media without glucose, at a density of $2 \cdot 10^6$ cells per ml and split into three portions. The first aliquot was supplemented with glucose (10 mM final concentration) and solvent of the inhibitors. The second and third aliquots were treated with 0.1 nM AA and 1 mM 2DG (D1) and 1 nM AA and 10 mM 2DG (D2), respectively. Subsequently, plates of the three conditions were incubated for 60 min at 37°C with 5%

CO₂. Two aliquots were collected from each condition and centrifuged for 3 min at 1000 × g and 80 µl of the supernatant media was removed. One aliquot each was treated with a mild lysis buffer (PBS with protease and phosphatase inhibitors, 2.1 mM MgCl₂, 1.12% NP-40 and 35 U per ml benzonase), while the other aliquot for each condition was treated with a strong lysis buffer (PBS containing protease and phosphatase inhibitors, 2.1 mM MgCl₂, 1.4% SDS and 35 U per ml benzonase). Insoluble proteins were pelleted by ultracentrifugation for 20 min at 100,000 × g at 4°C and removed. Experiments were performed by Sindhuja Sridharan (Sridharan et al., 2019).

2.3.4 Phospho-TPP experiments

HeLa Kyoto cells were grown at 37°C and 5% in Dulbecco’s modified Eagle’s medium (Sigma Aldrich, ID: D5030) supplemented with 10% FBS, 1 mM glutamine and 1 mg/ml glucose. For each of the five replicates, ten aliquots of 2×10^7 cells were prepared and heated to a temperature range between 37-66.3°C for 3 min, followed by 3 min incubation at room temperature. Cells were lysed using a PBS-based buffer with 0.8% NP-40, 1.5 mM MgCl₂, cOmplete protease inhibitors (Sigma Aldrich, ID: 11697498001), PhosSTOP (Sigma Aldrich, ID: 4906845001), benzonase, 2 mM NaF, 2 mM Na₃VO₄, 2 mM Na₄O₂P₇ at 4 °C for 1 h Protein aggregates were removed using filter plates and the soluble fraction was processed as described in “MS sample preparation”.

TMT-labeled, lyophilized peptides were resuspended in 70% ACN and 0.07% trifluoroacetic acid (TFA) and loaded for 6 min with a flow-rate of 400 µl/min onto a ProPac IMAC-10 column (Thermo Fisher Scientific, ID: 63276) which was pre-loaded with Fe³⁺ ions. The samples were washed for 6 minutes with 70% ACN and 0.07% TFA and subsequently phosphopeptides were eluted by changing the buffer to 0.3% ammonia at a flow-rate of 500 µl/min for 2 minutes. Phosphopeptide and non-bound fractions were collected lyophilised and analyzed by LC-MS/MS. These experiments were performed by Clément Potel, Isabelle Becher and André Mateus (Potel et al., 2021).

2.3.5 MS sample preparation

Sample processing was performed according to a modified SP3 protocol by Hughes et al. (2019). Protein containing samples were added to Sera-Mag Speed Bead ethanol suspension (Thermo Fisher Scientific, ID: 4515-2105-050250, 6515-2105-050250). After shaking samples for 15 min at room temperature, beads were washed four times with 70% ethanol. Then, 100 μ l protein digest buffer (30 mM chloroacetamide, 5 mM tris(2-carboxyethyl)-phosphine, 1 μ g/ μ l trypsin in 100 mM 4-(2-hydroxyethyl)-1-piperazineethanesulfonic (HEPES) with pH 8) was added to samples for on bead reduction, alkylation and digestion overnight. Resulting peptides were eluted from the beads and lyophilized. Dried peptides were reconstituted in 10 μ l water and 10 μ g of TMT10plex (8 μ g/ μ l) (Thermo Fisher Scientific) dissolved in acetonitrile (ACN). After 60 min the labeling reactions was quenched with 5 μ l of 2.5% hydroxylamine and sets of TMT-labeled peptides were pooled and vacuum dried for LC-MS/MS analysis (Sridharan et al., 2019). This step was performed by respective experimenters who had performed prior experiments.

2.3.6 LC-MS/MS analysis

Lyophilized peptides were reconstituted in 0.05% formic acid and analyzed on either a Q Exactive Plus Hybrid Quadrupol-Orbitrap or an Orbitrap Fusion Lumos Tribrid mass spectrometer (Thermo Fischer Scientific, ID: IQLAAEGAAPFALGMBDK and FETD2-10002). Before MS/MS analysis, peptides were separated using an UltiMate 3000 Nano RSLC system (Thermo Fischer Scientific, ID: 6041.7903A) featuring a trapping cartridge (Acclaim PepMap 100, C18 reversed phase, length: 15 cm, inner diameter: 300 μ m, particle size: 5 μ m, pore size: 100 Å) and an analytical column (Acclaim PepMap 100, C18 reversed phase, length: 50 cm, inner diameter: 75 μ m, particle size: 3 μ m, pore size: 100 Å). Solvent A (0.1 formic acid in MS grade water (Thermo Fisher Scientific, ID: 85189)) and solvent B (0.1 formic acid in MS grade ACN (Thermo Fisher Scientific, ID: 85188)) were used for online LC preparation and peptides were loaded onto the trap column at 30 μ l/min starting with solvent A and eluted by a gradient over 2 hours from

2 to 40 % of solvent B with 0.3 $\mu\text{l}/\text{min}$.

The Q Exactive Plus Hybrid Quadrupol-Orbitrap was operated in positive ion mode with a spray voltage of 2.3 kV and capillary temperature of 320°C. Full scan MS spectra with a mass range of 375-1200 m/z were acquired in profile mode in the Orbitrap using a resolution of 70,000 with maximum fill time of 250 ms or collecting a maximum of 3×10^6 ions using automatic gain control. MS/MS acquisition was triggered in a data-dependent mode and performed using consecutively fragmenting the top 10 MS1 peaks with charges between 2 and 4. Isolation of precursors was done using a mass-range window of 0.7 m/z and fragmentation was performed at 33 normalized collision energy.

The Orbitrap Fusion Lumos Tribrid mass spectrometer was operated in positive ion mode with a spray voltage of 2.4 kV and capillary temperature of 275°C. Full scan MS spectra with a mass range of 375-1500 m/z were acquired in profile mode in the Orbitrap using a resolution of 120,000 with maximum fill time of 50 ms or collecting a maximum of 4×10^5 ions using automatic gain control and the radio frequency lens was set to 30%. MS/MS acquisition was run in data-dependent mode with triggering fragmentation at a maximum duty cycle time of 3 s for peptide-like peaks with charge states between 2 and 7. Precursor isolation was done using a mass-range window of 0.7 m/z and fragmentation was performed at 38 normalized collision energy. Acquisition of fragment mass spectra was performed in profile mode at a resolution of 30,000 (Perrin et al., 2020; Sridharan et al., 2019).

Instruments of the EMBL proteomics core facility and Cellzome were operated by Dominic Helm and Mandy Rettel, and Thilo Werner respectively.

2.3.7 Fluorometric aminopeptidase assay

Recombinant LAP3 was acquired from (Origene, ID: NM_015907) and its activity was measured with the Leucine Aminopeptidase Activity Assay Kit (Abcam, ID: ab124627). LAP3 was dissolved in the assay buffer and either vehicle or 100 μM of PCI-34051 or BRD-3811 were added and the samples were incubated at room temperature for 10

min, before fluorescent signal (Ex/Em = 368/460 nm) was detected over 55 min. This experiment was performed by Isabelle Becher (Kurzawa, Becher, et al., 2020).

2.3.8 Differential scanning fluorometry with DHRS1

Recombinant DHRS1 (amino acids 3-262) fused to a cleavable His-Flag tag was expressed in *E. coli* was purified using Ni-Nitrilotriacetic acid affinity. A Prometheus NT.48 (NanoTemper Technologies, ID:PR001) was used to perform nano differential scanning fluorometry experiments according to manufacturer’s instructions. 100 µg/ml of recombinant DHRS1 were treated with 100 µM of Panobinostat or one of its metabolites. Analyses were performed using a temperature range of 20-90°C with a slope of 1.0 °C/min. T_{ms} of DHRS1 in the presence of the different compounds were determined as the first derivative of the fluorescence ratio at 350 nm to 330 nm. T_{ms} could not be determined if the compounds treated with were autofluorescent. These experiments were performed in duplicates by Jessica Perrin and Anna Rutkowska (Perrin et al., 2020).

2.3.9 BANF1 DNA pulldown

BANF1 fused to a cleavable His-tag was expressed from a codon-optimized plasmid in *E. coli*. The recombinant protein was purified using Ni-Nitrilotriacetic acid affinity and subsequent gel filtration chromatography using a Superdex-75 column (GE Healthcare). Purity of BANF1 was confirmed using intact mass analysis on a Q-TOF mass spectrometer. The purified protein was then incubated at a 1:1 ratio with a synthetic double stranded DNA oligo (FW-5'-Biotin-GTGTGGAAAATCTCTAGCAGTAAAAAAAAAAA-3' and RV-5'-TTTTTTTTTTTACTGCTAGAGATTTTCCACAC-3', annealed at 95°C for 5 min followed by a step-wise cool down to 4°C) together with 0, 0.1, 0.3, 1, 3, and 10 mM MgATP in Tris-buffered saline, 10 mM Tris-Cl, 150 mM NaCl, 3 mM KCl pH 7.5 (TBS) for 30 min at 25°C. The formed DNA-protein complex was pulled down with Streptavidin beads (Thermo Fisher Scientific, ID: 65601) according to the manufacturer’s protocol. Equal

amounts of the protein in isolation in the same buffer were used as a control for unspecific binding to the beads. After washing the beads with TBS supplemented with 0.2% NP-40 and with or without consistent ATP concentration, bead-bound protein was eluted with TBS supplemented with 0.1% SDS and was accompanied by heating for 5 min at 95°C. The eluate of the different samples were further processed for LC-MS/MS analysis. This experiment was performed by Sindhuja Sridharan (Sridharan et al., 2019).

2.4 Computational methods

2.4.1 Protein identification and quantification

Pre-processing of raw data was done using isobarQuant version 1.10 (Franken et al., 2015) and database search was performed using Mascot version 2.4 (Matrix Science) against the human (Uniprot, Proteome ID: UP000005640) or *E. coli* strain K 12 (Uniprot, Proteome ID: UP000000625) proteome extended by known contaminants and reversed protein sequences. The search parameters are listed in Table 2.4. Peptides were identified at 1% FDR using a target-decoy strategy and quantified using isobarQuant's post-Mascot routine which performs reporter ion peak integration. Protein-level FDR was controlled using the picked approach (Savitski et al., 2015).

2.4.2 Phosphopeptide identification and quantification

Phosphopeptide database search was performed with both isobarQuant version 1.10 (Franken et al., 2015) and MaxQuant version 1.6.2.3 (Cox & Mann, 2008) to benefit from precise isobaric quantification (isobarQuant) and phosphorylation site localization with annotation of confidence (MaxQuant).

Table 2.4: Database search parameters for standard peptide identification.

Parameter	Setting
Protease	Trypsin
Missed cleavages	3
Peptide tolerance	10 ppm
MS/MS tolerance	0.02 Da
Fixed modifications	Carbamidomethylation on cysteines; TMT10-plex on lysines
Variable modifications	Acetylation of N-termini; Oxidation of methionines; TMT10-plex on N-termini

Table 2.5: Database search parameters for phosphopeptide identification.

Parameter	Setting
Protease	Trypsin
Missed cleavages	3
Peptide tolerance	10 ppm
MS/MS tolerance	0.02 Da
Fixed modifications	Carbamidomethylation on cysteines; TMT10-plex on lysines
Variable modifications	Acetylation of N-termini; Oxidation of methionines; TMT10-plex on N-termini; Phosphorylation of serine; threonine and tyrosine

2.4.3 Analysis of temperature range thermal proteome profiling data

TPP-TR datasets were imported and normalized using the TPP package (Franken et al., 2015), except for phospho-TPP data which were normalized differently as outlined in the respective subsection.

Methods used to analyze normalized TPP-TR datasets in the context of PPIs are described in section “Thermal proximity coaggregation analysis of annotated protein pairs”. The melting point-centric comparison applied to phosphoTPP data is described in subsection “Melting point-centric analysis” of the respective section.

The analysis of the TPP-TR dataset comparing 10 mM MgATP with NP-40 control in Jurkat cell lysate encompassed assigning proteins into the groups ‘soluble’ and ‘insoluble’ based on whether they were found as significant hits in the SPP experiments comparing SDS and NP-40.

To compute the Euclidean distances between proteasome subunits as edge weights in the network in Figure 5.2a, the intact cell TPP-TR experiment of Jurkat cells included in the human meltome atlas (Jarzab et al., 2020) was used by averaging fold changes obtained from different replicates and applying Eq. 2.1 to obtain Euclidean distances between all pairs of proteins part of the 26S proteasome. To build the network, only PPIs with a melting curve distance of 0.5 or smaller were considered.

2.4.4 Thermal coaggregation based on melting point similarity

In order to assess globally whether subunits of protein complexes showed lower difference in melting points than expected by chance, we fitted sigmoid melting curves (Eq. 1.4) to the TPP-TR dataset by Becher et al. (2018) of HeLa cells synchronized in G1/S phase. Melting points for each protein were extracted and annotated for protein complexes using the data by Ori et al. (2016). Standard deviations (SD) of melting points per complex were computed. The same was done for 1000 random permutations of the complex annotation and the median of SD of melting points was compared.

2.4.5 Thermal proximity coaggregation analysis of annotated protein pairs

Fold changes obtained at temperature k for each protein, aggregated per gene symbol, were summarized by the median across replicates. A proteome-wide matrix of Euclidean distances across all K fold changes at temperature k was performed by computing:

$$d_{i,j} = \frac{1}{K} \sqrt{\sum_{k=1}^K (r_{i,k} - r_{j,k})^2} \quad (2.1)$$

for each possible pair of proteins i and j (Tan et al., 2018). The obtained distance matrix was reduced to the lower triangular values and converted to long table format, i.e., a table with two columns: protein pair id and average Euclidean distance (ED). To generate unique protein pair ids the two proteins were ordered alphabetically. The resulting long table was sorted by ED in increasing order and known PPIs were annotated based on the STRING database (Szklarczyk et al., 2019). True positive rate ($\text{TPR} = \frac{\text{TP}}{\text{TP} + \text{FN}}$, sensitivity), true negative rate ($\text{TNR} = \frac{\text{TN}}{\text{TN} + \text{FP}}$, 1-specificity) and the area under the receiver operating characteristic (ROC) curve (AUC) were computed using the pROC R package.

Next, 10,000 random pairs of proteins were drawn and their ED $d_{i,j}^*$ was computed according to Eq. 2.1. By comparison of the distribution of EDs obtained from the annotated PPIs with the randomly drawn ones an empirical p -value was computed for the coaggregation of each annotated PPI with an ED of $d_{i,j} \leq \theta$ with:

$$\hat{p}(\theta) = \frac{\#\{d_{i,j}^* \leq \theta\}}{\#\{d_{i,j}^*\}}. \quad (2.2)$$

Obtained p -values were adjusted for multiple testing using the method of Benjamini and Hochberg (Benjamini & Hochberg, 1995). PPIs with an adjusted p -value with $p_{\text{adj.}} \leq 0.1$ were accepted as significantly coaggregating protein pairs.

2.4.6 Thermal proximity coaggregation analysis of annotated protein complex subunits

The all versus all protein distance matrix was computed as for the PPI coaggregation analysis. Then, all unique PPIs $m = (i, j)$ between subunits of annotated protein complexes by Ori et al. (2016) were combined to an average ED $d_{i. c.}$ (intra complex) per complex with:

$$d_{i. c.} = \frac{1}{M} \sum_{m=1}^M d_m \quad (2.3)$$

with M representing the total number of unique PPIs per complex (Tan et al., 2018). To test for significant coaggregation of protein complexes, for each distinct total number of unique PPIs per complex M , 10,000 groups of proteins with equivalent size were randomly drawn and an empirical p -value was computed with Eq. 2.2 considering $d_{i. c.}$ and $d_{i. c.}^*$ instead of $d_{i,j}$ and $d_{i,j}^*$ (Tan et al., 2018).

In order to create ROC curves to represent a dataset’s specificity and sensitivity in recovering annotated protein complexes, we generated five permuted lists of annotated protein complexes reflecting the size distribution of the truly annotated complexes. The average EDs for truly annotated protein complexes as well as for the permuted annotation were computed with Eq. 2.3. A separate table with the columns protein complex id and average ED was then created for every version of the permuted complex annotation and the values obtained for the true annotation, sorted by increasing average ED and assigned a rank. TPR and FPR (TPs were considered truly annotated protein complexes and FP protein complexes from the permuted complex annotation) were then computed as average TPR and FPR observed per rank across the different tables. The AUC was then computed through integration of the ROC curve (Kurzawa, Mateus, et al., 2020).

2.4.7 Differential thermal proximity coaggregation analysis

In order to detect changes in thermal coaggregation of two proteins i and j annotated to interact, in conditions c_1 and c_2 , a different type of distance matrix, featuring the

residual sum of squares (RSS) between each pair of proteins i and j for both condition individually was obtained with:

$$\text{RSS}_{i,j}^c = \sum_{k=1}^n (r_{i,k} - r_{j,k})^2. \quad (2.4)$$

Next, a statistic similar to an F -statistic (Eq. 1.2), but not obtained from a nested model situation, was computed with:

$$F_{i,j} = \frac{|\text{RSS}_{i,j}^{c_1} - \text{RSS}_{i,j}^{c_2}|}{\min(\text{RSS}_{i,j}^{c_1}, \text{RSS}_{i,j}^{c_2})}. \quad (2.5)$$

To assess significance of $F_{i,j}$ above a given threshold θ , we made use of a similar empirical p -value calculation as in Eq. 2.2 by computing $F_{i,j}^*$ for 10,000 pairs of proteins, not annotated as interactors. Specifically, we computed:

$$\hat{p}(\theta) = \frac{\#\{F_{i,j}^* \leq \theta\}}{\#\{F_{i,j}^*\}}. \quad (2.6)$$

Obtained p -values were adjusted for multiple testing (Benjamini & Hochberg, 1995) and protein pairs with $p_{\text{adj.}} \leq 0.1$ were considered to change significantly in their coaggregation behavior between the two conditions (Kurzawa, Mateus, et al., 2020).

2.4.8 Detection of ligand-protein interactions from 2D thermal profiles

In order to detect proteins whose thermal profiles were altered by the presence of a ligand in a dose-dependent manner and thus were assumed to be bound by the profiled ligand, we performed hypothesis tests on curves fitted to the abundance of proteins derived from 2D-TTP (DLPTP). The method adapts and extends the approach by Storey et al. (2005) for analysis of microarray time-course experiments and was implemented by fitting two parametric nested models for each protein i at temperature j and ligand concentration k .

Data pre-processing

Quantification of unique reporter ion spectra were aggregated per protein (gene symbol) by summing ion peak areas for all cases in which proteins had been quantified by at least two unique peptides. Cases with only one unique peptide per protein were not considered. Thus, intensity values $s_{i,u}$ were obtained for protein i in condition $u = (j, k)$, at temperature j and ligand concentration k . Further, we made use of the robust fold change estimates $r_{i,u}$ for jointly multiplexed conditions relative to control condition u' , computed by isobarQuant (Franken et al., 2015). By combining them with the summed reporter ion intensity across all channels, we computed \log_2 signal intensities $y_{i,u}$ more accurately reflecting the relative differences between different conditions

$$y_{i,u} = \log_2\left(\frac{r_{i,u}}{\sum_l r_{i,l}} \sum_l s_{i,l}\right), \quad (2.7)$$

where l contained all u of one set of multiplexed channels. The obtained abundance table $Y = (y_{i,u})$ was filtered to contain only cases with $p_i = \#\{y_{i,u}\} \geq 20$, i.e., proteins had to be quantified at least at four temperatures and at all ten respective ligand concentrations (Kurzawa, Becher, et al., 2020).

Data exclusion

For the dataset profiling PCI-34051 it was noticed that the measurements at temperatures 54 and 56.1°C had unexpectedly high noise levels. Especially, the relative reporter ion intensities obtained at 54°C showed about ten times higher variances in comparison to other temperatures. Hence, the data measured for these temperature was excluded from the analysis.

Moreover, in the datasets profiling the drugs PCI-34051 and BRD-3811, we found that thermal profiles of some proteins were affected by carry-over, i.e., instruments were still containing peptides from MS experiments runs prior to the acquisition for these datasets. These cases showed a pattern of stabilization at every other temperature and no continuous profiles. Such cases (individual proteins with their entire profiles) were identi-

fied by manual inspection and removed before model fitting (Kurzawa, Becher, et al., 2020).

Description of models

The null model, expected for no ligand induced effect, is:

$$y_{i,j,k} = \beta_{i,j}^{(0)} + \epsilon_{i,j,k}^{(0)}. \quad (2.8)$$

Here, $\beta_{i,j}^{(0)}$ is the base intensity level a temperature j and $\epsilon_{i,j,k}^{(0)}$ is a residual noise term. The alternative model, reflecting thermal profiles affected by the compound in a dose-dependent manner, is:

$$y_{i,j,k} = \beta_{i,j}^{(1)} + \frac{\alpha_{i,j}\delta_i}{1 + \exp(-\kappa_i(c_k - \zeta_i(T_j)))} + \epsilon_{i,j,k}^{(1)}. \quad (2.9)$$

Here, the base intensity at temperature j is $\beta_{i,j}^{(1)}$, δ_i represents the maximal absolute stabilization across all temperatures measured for protein i , $\alpha_{i,j} \in [0, 1]$ describes which fraction of the maximal stabilization happens at temperature j and κ_i is a joint slope factor optimized across all temperatures. Lastly, the concentration of half-maximal stabilization is reflected by $\zeta_i(T_j)$, also referred to as half maximal effective concentration in $-\log_{10}$ space (pEC50), with $\zeta_i(T_j) = \zeta_i^0 + a_i T$, where a_i is a slope indicating a linear temperature-dependent increase or decay of the inflection point, and ζ_i^0 is the intercept term of the linear model. As for the null model, $\epsilon_{i,j,k}^{(1)}$ is a residual noise term.

Model fits were obtained by minimization of the sum of squared residuals $RSS_i^{(0)} = \sum_j \sum_k (\epsilon_{i,j,k}^{(0)})^2$ and $RSS_i^{(1)} = \sum_j \sum_k (\epsilon_{i,j,k}^{(1)})^2$ using the L-BFGS-B algorithm (Byrd et al., 1995) using R's `optim` function.

The start values for iterative optimization of $\beta_{i,j}$ in both models were initialized with the mean abundance $\bar{y}_{i,j}$ of protein i at temperature j ; δ_i was set to the maximal difference observed between abundance values within a temperature for protein i ; $\alpha_{i,j}$ was initialized as $\alpha_{i,j} = 0$ for all i and j ; κ_i was initialized with the value estimated for the slope of a linear model across temperatures; ζ_i^0 was set to the average \log_{10} drug concentration

featured in the experiment; and a_i was set to 0. The sum of squared residuals obtained of both models were compared using the F -statistic (Eq. 1.2). In this case, the parameters in Eq. 1.2, $d_1 = \nu_1 - \nu_0$ and $d_2 = p_i - \nu_i$ represent the models' respective degrees of freedom, where p_i is the number of observed data points for protein i , and ν_0 and ν_1 are the number of parameters of the null and alternative model respectively.

Moreover, we computed an *empirical Bayes moderated* version of Eq. 1.2, by making use of the `squeezeVar` function of the R/Bioconductor package `limma` (Ritchie et al., 2015). The function `squeezeVar` uses the observed variances $s_i^2 = \text{RSS}_i^{(1)}/d_2$ to estimate a common value s_0^2 and shrinks each s_i^2 towards that value. To do so, `squeezeVar` assumes that the true σ_i^2 come from a scaled inverse χ^2 distribution with parameter s_0^2 :

$$\frac{1}{\sigma_i^2} \sim \frac{1}{d_0 s_0^2} \chi^2. \quad (2.10)$$

By assuming that the residuals follow a normal distribution, using the scaled inverse Chi-squared prior and Bayes' theorem, it can be derived (Smyth, 2004) that the expectation value of the posterior of $\sigma_i^2 | s_i^2$ is

$$\tilde{s}_i^2 = \frac{d_0 s_0^2 + d_2 s_i^2}{d_0 + d_2}. \quad (2.11)$$

The hyperparameters s_0^2 and d_0 are approximated by fitting a scaled F -distribution with $s_1^2 \sim s_0^2 F_{d_2, d_0}$ (Smyth, 2004). Thus, we obtained moderated \tilde{F} -statistics with

$$\tilde{F} = \frac{\text{RSS}_i^{(0)} - \text{RSS}_i^{(1)}}{\tilde{s}_i^2 d_1} \quad (2.12)$$

(Kurzawa, Becher, et al., 2020).

FDR estimation

To approximate the false discovery-rate (FDR) for rejecting the null model for protein i with $m_i n_i$ observations and $\tilde{F} = \theta$, we applied a modified version of the bootstrap approach by Storey et al. (2005) : To obtain a null distribution, we repeated the following procedure B -times: i) Draw a randomized sample with replacement of the residuals $\epsilon_{i,w}^1$ of

the alternative model fit for protein i in MS experiment w to obtain $\epsilon_{i,w}^{1*}$ and add them to the fitted estimates of the respective null model of protein i to obtain $y_{i,w}^* = \mu_{i,t}^0 + \epsilon_{i,w}^{1*}$. ii) Fit both models (Eqs. 2.8 and 2.9) to $y_{i,w}^*$ and compute \tilde{F}_i^{0b} . FDR was then estimated by partitioning all proteins $\{1, \dots, P\}$ into groups with similar number of observations $D(p)$ with $\gamma(p) = \lfloor \frac{D(p)}{10} + \frac{1}{2} \rfloor$ and then:

$$\widehat{\text{FDR}}_g(\theta) = \hat{\pi}_{0g}(\theta) \frac{\sum_{b=1}^B \#\{\tilde{F}_p^{0b} \geq \theta | \gamma(p) = g\}}{B \cdot \#\{\tilde{F}_p \geq \theta | \gamma(p) = g\}}. \quad (2.13)$$

The fraction of true null events $\hat{\pi}_{0g}$ for the group g of proteins was estimated by:

$$\hat{\pi}_{0g}(\theta) = \frac{B \cdot \#\{\tilde{F}_p < \theta | \gamma(p) = g\}}{\sum_{b=1}^B \#\{\tilde{F}_p^{0b} < \theta | \gamma(p) = g\}}. \quad (2.14)$$

For the standard DLPTP approach (without moderation), we performed the same approach as described above using F -statistics derived from Eq. 1.2 without subsequent moderation (Kurzawa, Becher, et al., 2020).

Incorporation of replicates

To estimate FDR for ligand effects on thermal profiles of protein obtained by 2D-TPP experiments performed in replicates, we performed the above described model fitting and computing of moderated F -statistics and bootstrapping ($B = 100$) for proteins from both replicates separately. We then required that a protein had been fit in both of the replicates and chose for each protein in each dataset (true and different rounds of bootstrapping) the lowest obtained F -statistic. Based on the retrieved dataset, we performed the above indicated steps for FDR estimation.

2.4.9 Differential Solubility Proteome Profiling analysis

Differential analysis of SPP data was performed using the R/Bioconductor package `limma` (Ritchie et al., 2015), by comparing the \log_2 intensity levels of control conditions (NP-40 without any compound) and the highest treatment condition with ATP, GTP, AMP-PNP

or SDS. The design formula was *intensity* \sim *condition* + *batch*.

Positive effective solubilization concentrations (pESC₅₀) were determined for proteins found to significantly change in the highest treatment condition with a minimal fold change of 1.5. Sigmoidal curves were fitted to log₂-transformed relative fold changes measured at log₁₀-transformed concentrations x with Eq. 1.4, where x represented the compound concentration, using the R package `drc` (Ritz et al., 2015). The parameter pESC₅₀ was then computed as $\text{pESC}_{50} = -a$.

2.4.10 Phospho-TPP data analysis

Obtained database search results from isobarQuant (Franken et al., 2015) and MaxQuant (Cox & Mann, 2008) were joined by peptide MS/MS scan id and filtered to contain at least one phosphosite with a localization probability greater than 0.75 as obtained from the MaxQuant output. Additional filtering criteria to keep phosphopeptides for further analysis were: a signal to interference ratio higher or equal to 0.5 and a precursor to threshold ratio higher or equal to 4 to keep only peptides with low levels of co-isolation and thus avoid ratio compression (Savitski et al., 2013). Peptides which shared phosphosite localization and identical sequences were aggregated by summation of signal intensities.

For the non-modified fraction only isobarQuant search and quantification results were used. Filtering criteria for non-modified peptides were that they mapped to one protein only, had a Mascot score of greater than 20 and an FDR lower than 1%. Fold changes were computed for all phospho- and non-modified peptides by dividing all signal intensities by the respective signal intensity measured at the lowest temperature, 37°C.

Normalization

A two-step normalization procedure was performed to first adjust for global differences in the phosphopeptide enriched samples to their corresponding flow-through (non-modified)

samples, and second a curve-based normalization to account for TMT-channel differences.

In the first step, normalization factors were retrieved to align median fold changes of non-modified peptides quantified in matching replicates of phospho- and non-modified samples by restricting overlapping peptides to follow expected melting curves (observed fold change at the 7th temperature should be between 0.4 and 0.6, between 0 and 0.4 for the 9th temperature, and between 0 and 0.2 for the 10th temperature) (Potel et al., 2021).

After obtained normalization factors were applied, the curve-based normalization strategy suggested by Savitski et al. (2014) was performed. This was done by finding the set of overlapping peptides across all replicates of unmodified datasets, filtering these according to similar fold changes boundaries as before (the fold change measured at the 3rd temperature should be higher than 1, between 0.4 and 0.6 at the 7th temperature, between 0 and 0.3 at the 9th temperature, and between 0 and 0.2 at the 10th temperature). We then chose the replicate per condition with the highest subset of these peptides fulfilling these criteria S_{hq} and fitted a melting curve to their median fold changes at each temperature using Eq. 1.4, where x represented the temperature. Normalization factors for each replicate were then obtained for each replicate as the ratio of observed median fold change across of all peptides in S_{hq} and the predicted value by the fitted melting curve. Obtained normalization factors for each replicate were then applied to normalize unmodified and phosphopeptide enriched datasets of the same replicate (Potel et al., 2021).

Melting point-centric analysis

Sigmoidal melting curves were fitted to normalized fold changes measured for phosphopeptides with a distinct modified sequence and to normalized fold changes obtained for all peptides mapping uniquely to one protein. The sigmoid model used was Eq. 1.4, where x represented the temperature.

Melting curves were only accepted if $R^2 \geq 0.8$ and the plateau was below 0.2. Fits not fulfilling these requirements were removed from further analysis. Melting points of remaining fits were estimated as $\mu(T_m) = 0.5$. To assess significantly thermally shifted phosphopeptides compared to respective proteins, we applied the method described by Savitski et al. (2014). This included filtering T_m estimates of phosphopeptides and corresponding proteins to determined in at least three replicates, computing replicate-wise ΔT_m , z -transforming and converting z -scores into p -values. Obtained p -values were then adjusted for multiple testing using the Benjamini-Hochberg procedure. To call a phosphopeptide significantly differentially thermally stable compared to its protein, we asked for at least two replicates with and $p_{\text{adj.}} \leq 0.1$ and an equal sign of the thermal shift in all replicates.

Curve-centric analysis using Gaussian processes

For the curve-centric analysis, all replicates were once fitted jointly across phosphopeptides and respective non-modified proteins (null model) and once for each condition separately (alternative model), using a Gaussian process:

$$f(x) \sim \text{GP}(\mu(x), k(x, x')), \quad (2.15)$$

where $k(x, x')$ was taken as a radial basis function kernel and x is the temperature at which relative fold changes were observed. The posterior mean function $\mu_{f|\mathcal{D}}(x)$ was computed using the python (version 3.7.4) package `gpytorch` (version 1.0.1) (Gardner et al., 2018) by maximizing the Gaussian likelihood. The code was adapted from a script provided by Britta Velten.

The $\text{RSS}_{0/1}$ obtained from null and alternative model fits were then analyzed using the NPARC (nonparametric analysis of response curves) procedure (Childs et al., 2019). This involved computing an F -statistic according to Eq. 1.2.

To find a suitable null distribution for obtained F -statistics, we created a synthetic dataset. This was done by picking for each protein, for which we found at least one phosphopeptide in at least three replicates to compare with, a random non-modified

peptide. We then performed the same procedure as for the phosphopeptide vs. non-modified protein data by comparing melting profiles of picked peptides with non-modified protein profiles inferred from the remaining peptides. Then, the procedure, described by Childs et al. (2019), was performed to estimate degrees of freedom d_1^* and d_2^* of the F -distribution after NPARC analysis. Next, p -values were obtained using the $F_{d_1^*, d_2^*}$ -distribution and F -statistics obtained from the actual comparison of phosphopeptide vs. non-modified protein melting profiles, adjusted for multiple testing using the Benjamini-Hochberg procedure and phosphopeptides were considered significantly thermal shifted if $p_{\text{adj.}} \leq 0.01$.

2.4.11 Annotation of protein features and ontologies

Annotation of *E. coli* complexes and protein localization to compartments

E. coli protein complexes were annotated using the EcoCyc database (Keseler et al., 2017). Protein localization was annotated using the STEPdb 2.0 database (Loos et al., 2019). Proteins were annotated using gene level information provided by EcoCyc and STEPdb.

Annotation of protein disorder and isoelectric points

Protein disorder and isoelectric points were annotated using the Uniprot ID per gene symbol with the longest sequence provided by Oates et al. (2013) and Kozłowski (2017) respectively.

Gene ontology annotation and enrichment analyses

Annotation of gene ontologies (GO) was done using the R/Bioconductor packages **Anno-****tationDbi** (Pagès et al., 2020) and **org.Hs.eg.db** (Carlson, 2020). Enrichment analyses for GO terms associated to *cellular compartment* or *biological process* were performed

using the R/Bioconductor package `clusterProfiler` (Yu et al., 2012) using a q -value cutoff of 0.1 and the method of Benjamini and Hochberg for adjusting for multiple testing (Benjamini & Hochberg, 1995).

Chapter 3

Thermal proteome profiling to probe protein-protein interactions and protein complexes

“The main idea behind complex systems is that the ensemble behaves in ways not predicted by its components.”

— Nassim Nicholas Taleb, *Skin in the Game*

This chapter details how TPP datasets can be analyzed to inform on PPI dynamics. An R/Bioconductor package `Rtpca` (<https://bioconductor.org/packages/Rtpca>) (Kurzawa, Mateus, et al., 2020), which was created for this purpose, is presented. The application of the software focuses on two datasets: an experiment comparing different phases of the human cell cycle (Becher et al., 2018) and an experiment which profiles proteome thermal stability in *E. coli* cells (Mateus et al., 2018).

3.1 Thermal proximity coaggregation

As reported by Tan et al. (2018), we observed that thermal stability of protein complex members is more similar than expected by chance (Figure 3.1) (Becher et al., 2018). This finding paved the way for systematic analyses of TPP experiments with regard to assembly states of protein complexes and presence of PPIs in different biological samples and conditions. While our approach of comparing standard deviations of melting points within complexes allowed us to test for the effect of coaggregation of interacting proteins on a global scale, the method by Tan et al. (2018) allows to test for the association of individual protein complexes or PPIs, a method termed Thermal Proximity Coaggregation Analysis (TPCA) (Figure 3.2).

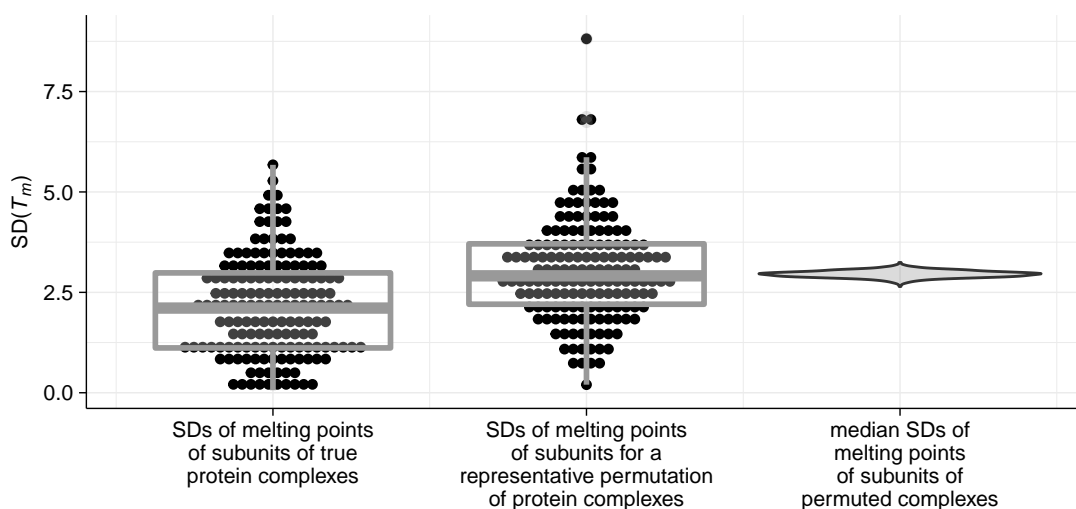


Figure 3.1: Assessing coaggregation by melting point similarity. Comparison of standard deviations of melting points of proteins, part of the same complex. Dotplot and boxplot show the distribution of values obtained for complexes, violin plot shows the distribution of medians of standard deviations of melting points obtained for 1000 permutation of the complex annotation list. The median SD of melting points obtained for the true protein complex annotation (bold line in boxplot) is clearly lower than any of those obtained by permuted complex annotation (violin plot).

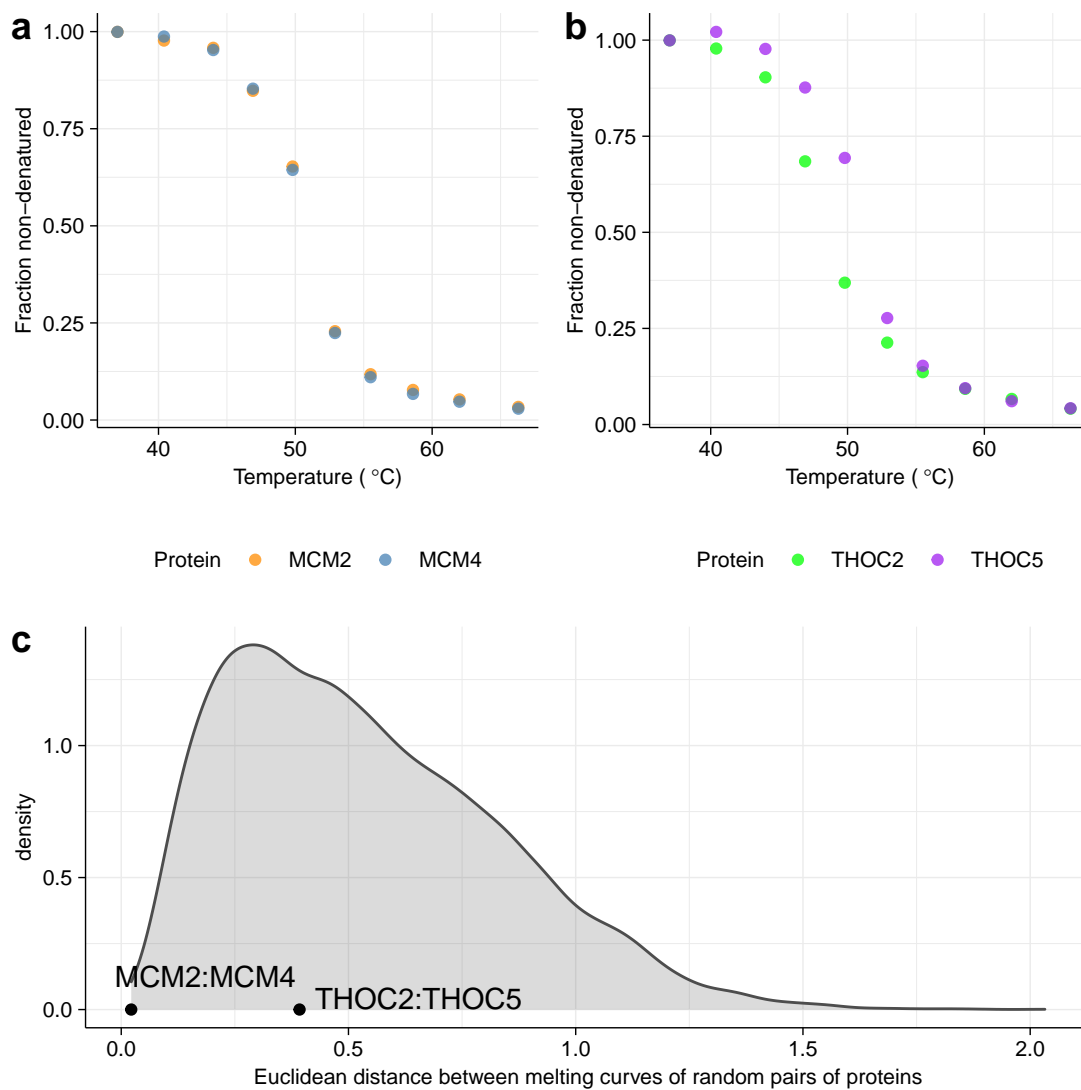


Figure 3.2: The concept of thermal proximity coaggregation analysis. a) Example profiles of the proteins MDM2 and MDM3 which are found to significantly coaggregate with TPCA. b) Example profile of two proteins annotated to interact, but not showing coaggregation. c) Distribution of Euclidean distances between random pairs of proteins used to determine significance of values obtained for annotated interactors.

3.2 An R package for analysis of PPI dynamics using TPP datasets

The goal of creating an R package for performing TPCA was to build a package for the standardized and efficient coaggregation analysis as an extension to the existing R/Bioconductor package TPP (Franken et al., 2015) which can handle data import and normalization and differential melting curve analysis, but not TPCA. Moreover, we aimed to expand this package by a method that allowed to test for differential PPIs across distinct conditions. Hence, we created the R/Bioconductor package `Rtpca` (<https://bioconductor.org/packages/release/bioc/html/Rtpca.html>) (Kurzawa, Mateus, et al., 2020).

To showcase the functionality of the package and the ability of using TPP datasets to infer assembled protein complexes, PPIs and their dynamics, we reanalyzed the TPP-TR dataset by Becher et al. (2018) comparing the human cell cycle phases G1/S (interphase) and M (mitosis).

3.2.1 TPCA of datasets in a single condition

The first function we created was `runTPCA` which implements TPCA to find significantly coaggregating PPIs based on an imported TPP dataset and a PPI or protein complex annotation. Moreover, when setting the parameter `doRocAnalysis = TRUE` it also computes receiver operating curves (ROC) for the PPI-predictive power of the dataset. This is done by sorting all protein pairs by the obtained Euclidean distance of their melting profiles and annotating whether they are known interactors or not. If true positive interactors are enriched at the top of the table, i.e., have a low Euclidean distance, one is more likely to predict a true interaction than just by chance ($AUC > 0.5$).

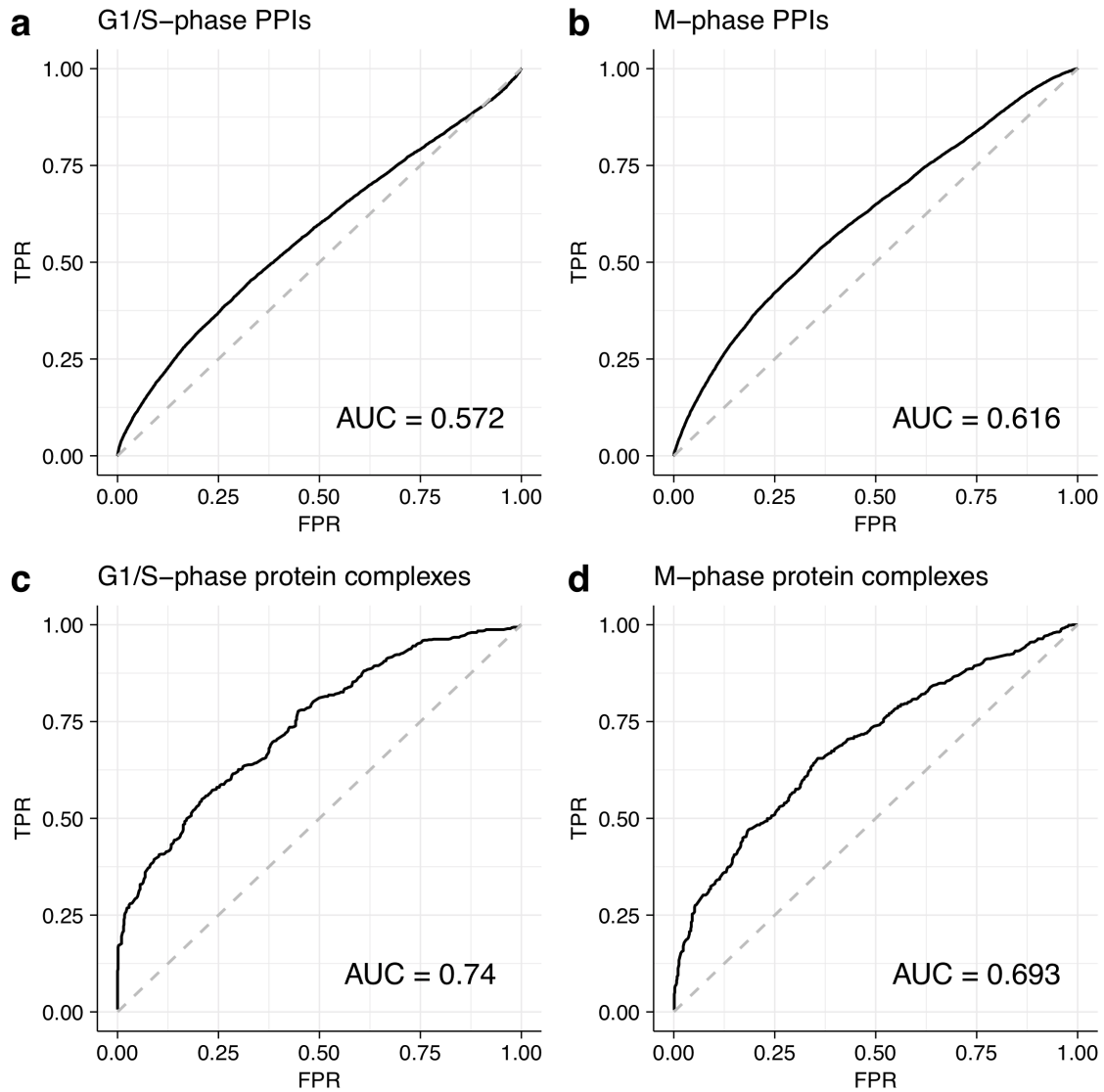


Figure 3.3: PPI and complex predictive performance of TPP datasets of different cell cycle stages. a-b) ROC curves for prediction of PPIs in G1/S (a) and M phase. c-d) ROC curves for TPCA-based prediction of protein complexes in G1/S (c) and M phase (d).

In addition to the ROC curves for PPIs suggested by Tan et al. (2018) (Figure 3.3a and b), we also implemented a version that works for protein complexes (Figure 3.3c and d) which uses truly annotated protein complexes as true positives and permuted complex annotations as false negatives. When running `Rtpca` on the datasets obtained for both cell cycle phases we observed both, PPIs that were found to significantly coaggregate in both phases such as the two mitochondrial tryfunctional enzyme subunits *HADHA:HADHB* and PPIs that could only be found in one of the phases, e.g., the members of the Sin3 deacetylase complex *HDAC1:SIN3A* which only coaggregated in interphase. On the complex level, we observed the same. For example, we found the RNA polymerase III core complex only to significantly coaggregate in G1/S, and the Cohesin complex in M phase.

3.2.2 Detection of differential PPIs using TPCA

The second function we implemented was to enable differential PPI coaggregation analysis for which we took a different approach than suggested by Tan et al. (2018). While Tan et al. (2018) used the difference in Euclidean distance between the melting curves of two proteins annotated to interact to find changes in coaggregation, we developed a method which also incorporated information on whether the coaggregation of two PPIs was at all evident in one of the tested conditions based on a statistic (Eq. 2.5) inspired by the F -statistic.

In order to perform successful differential coaggregation analysis, however, one needs to consider the limited power of TPCA, i.e., the small AUC of the ROC curve for predicting PPIs (Figure 3.3a and b). This limited enrichment of true PPIs, due to the relatively high chance of similarity of melting curves between two proteins which do not coaggregate, requires to focus the analysis on a set of potential interactors with an increased fraction of true positives to be able to recover true positives when the multiple testing burden is high. Thus, we have developed two strategies to cope with this challenge which are presented and compared using the TPP-TR dataset of Becher et al. (2018) in the

following subsections.

Analysis of PPI dynamics during the human cell cycle

We downloaded the TPP-TR dataset of Becher et al. (2018) and imported and formatted the data. PPIs were annotated using interactions listed in the STRING database (Szklarczyk et al., 2019) with a combined score of 975 or higher. Annotation of protein complexes was taken from Ori et al. (2016). ROC curves for PPI- (Figure 3.3a and b) and protein complex-predictiveness (Figure 3.3c and d) for datasets of both cell cycle phases and significantly coaggregating PPIs were determined using the TPCA procedure by invoking the `Rtpca` function `runTPCA` with `doRocAnalysis = TRUE`. Interestingly, while there appeared to be stronger coaggregation of PPIs in M phase compared to G1/S (larger AUC in Figure 3.3b than a), the trend was inverse when considering protein complexes (larger AUC in Figure 3.3c than d).

Next, we applied our newly developed method, implemented as function `runDiffTPCA` as part of the `Rtpca` package, to find differential PPIs between the different cell cycle stages. To do so, we followed two different strategies: i) we restricted the PPIs to test for differential TPCA to those that had been found to significantly coaggregate ($p_{\text{adj.}} < 0.2$, Note: we were intentionally less stringent here, to not exclude too many PPIs a priori) in either of the two cell cycle phases and ii) we included all possible intra-complex PPIs of all complexes that had been found to significantly co-melt ($p_{\text{adj.}} < 0.2$) for differential TPCA testing. Both strategies found differently coaggregating PPIs, with the PPI-centric approach finding many more at $p_{\text{adj.}} < 0.1$ ($n = 41$) compared to the complex-centric one ($n = 7$) (Figure 3.4). The intra-ribosomal PPIs *RPS6:RPSA* and *RPS23:RPSA* were found by both strategies to be differentially coaggregating, i.e., comelting in G1/S, but not in M phase. The PPI-centric approach additionally found the eukaryotic translation initiation factors *EIF3D:EIF3E* to be associated in G1/S, but not in M phase. Together with the ribosomal proteins, this may reflect the high global translational activity in G1/S compared to M phase (Tanenbaum et al., 2015). The PPI-centric found *CDC5L:EXOC7*

as coaggregating in M, but not in G1/S phase. CDC5L is pre-mRNA splicing factor crucial for mitotic progression (Mu et al., 2014). Its mitosis-specific association with exocyst complex subunit EXOC7, could be related to regulation of splicing specific to genes involved in mitosis (Dellago et al., 2011; Mu et al., 2014). On the other hand, the complex-centric approach found several nucleoporins (NUP188, NUP88, NUP93 and NUP205) to coaggregate mitosis-specifically with the Nuclear pore complex associated protein RANBP2. The strong association of RANBP2 with these nucleoporins in M phase, could be due to RANBP2's role in nuclear envelope breakdown during mitosis (Prunuske et al., 2006).

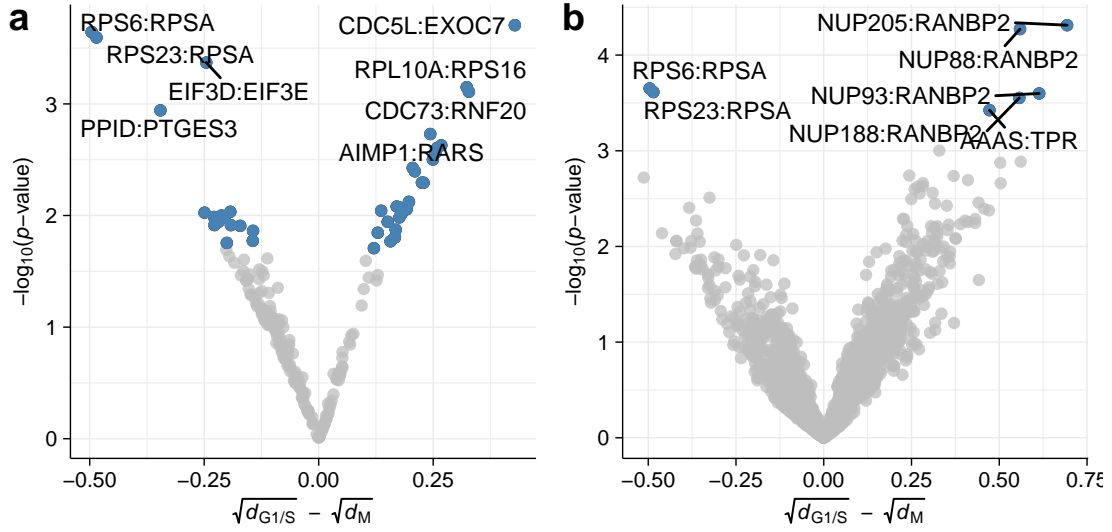


Figure 3.4: Results obtained from differential thermal coaggregation analysis between G1/S and M phase. Volcano plots obtained from a) PPI-centric and b) complex centric approach. Blue dots represent PPIs found to significantly differentially coaggregate between the two conditions with $p_{\text{adj.}} < 0.1$.

3.2.3 TPCA of the *E. coli* proteome

The TPP technology was first developed in human cells (Savitski et al., 2014). The interest in expanding the assay to other organisms led our group to adapt the technology

to *Escherichia coli*, through several modifications in the protocol (Mateus et al., 2018). Based on the previous observations concerning PPIs and protein complexes in human cells, we were interested whether TPCA would also recover known protein complexes in bacterial cells. Thus, we obtained an annotation of protein complexes in *E. coli* from the EcoCyc database (Keseler et al., 2017) and performed TPCA. The ROC curve we obtained from this analysis showed that melting curves measured in *E. coli* were predictive for protein complexes (Figure 3.5a). However, when comparing the distribution of average Euclidean distances of melting curves of complex subunits with the ones obtained for human (Figure 3.5b), we observed that the obtained values in *E. coli* were on average higher and that less significantly coaggregating complexes were found.

We noticed that the average thermal stability of proteins in *E. coli* varies considerably across different compartments, with thermal stability in general increasing from inner to outer compartments (Mateus et al., 2018). Since compartment spanning complexes in *E. coli* are common, e.g., many ABC-transporter complexes, we wondered whether complex aggregation was influenced by the localization of subunits to multiple compartments. Thus, we made use of the STEPdb 2.0 database (Loos et al., 2019) which annotates the majority of known *E. coli* proteins to different compartments and we split complexes into a group that featured complexes with subunits localized to the same compartment and a group of complexes with subunits annotated to localize to multiple compartments. When we compared Euclidean distances of complexes in both groups, we found that when protein complex subunits were all localized in one compartment the distribution of average Euclidean distances appeared comparable to those obtained for human complexes and that only compartment-spanning complexes showed higher Euclidean distances (Figure 3.5c).

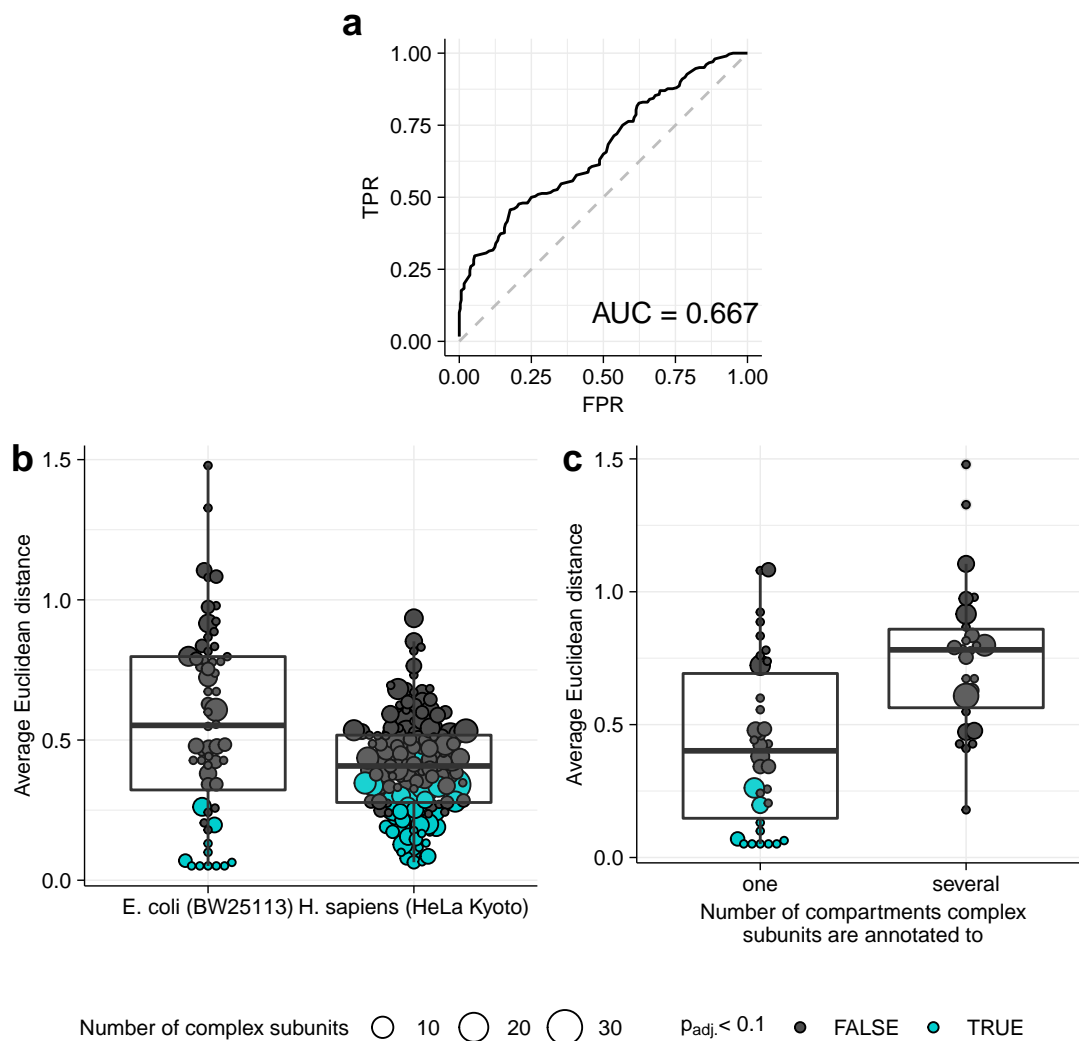


Figure 3.5: TPCA of protein complexes in *E. coli*. a) ROC curve for prediction of protein complexes based on coaggregation of subunits in the *E. coli* TPP dataset. b) Comparison between average Euclidean distances of complex subunit melting profiles obtained in human and *E. coli* TPP experiments. c) Average Euclidean distances of complexes with all subunits in one versus multiple compartments in *E. coli*.

3.3 Conclusion

In this chapter, it was shown that TPP experiments can be informative on PPIs and the association of protein complexes. Using a TPP-TR dataset profiling different stages of the human cell cycle, it was demonstrated how computational methods, implemented in the `Rtpca` software, can be used to infer PPIs and complex assembly in individual datasets and how to find differential associations between different conditions. Moreover, by analyzing TPP-TR data obtained for the bacterium *Escherichia coli*, it could be shown that also in this organism TPP can be used to inform on PPIs and protein complexes with the limitation that in *E. coli* many complexes feature subunits in different compartments and it was found that such cases are not amenable for coaggregation analysis.

Chapter 4

Computational detection of ligand-protein interactions from two-dimensional thermal proteome profiles

“An expert is a person who has made all the mistakes that can be made in a very narrow field.”

— Niels Bohr

In this chapter a computational method for the analysis of 2D-TPP, an experimental design of the TPP assay for sensitive profiling of ligand-protein interactions, is introduced. The approach is benchmarked on a synthetic dataset and applied to multiple real datasets. It was implemented as an R/Bioconductor package TPP2D (<https://bioconductor.org/packages/TPP2D>) and is thus freely available and open source (Kurzawa, Becher, et al., 2020).

4.1 Data obtained from 2D-TPP experiments

In 2D-TPP experiments (Becher et al., 2016), thermal stability of proteins is measured as a function of n concentrations of a ligand of interest and m temperatures (Figure 1.6). Hence, an $n \times m$ matrix Y_i of intensity values is observed for protein i (Figure 4.1 a). However, due to the fact that for some proteins a major proportion of the intracellular pool will denature at temperatures lower than the maximal temperature used for the heat treatment and may thus not be quantified at higher temperatures, these data matrices contain non-randomly missing values towards higher temperatures. Moreover, due to the long measurement time required to record a single replicate of a 2D-TPP experiment, they are in most cases acquired in only one replicate.

4.2 A curve-based hypothesis testing framework for 2D-TPP analysis

The first analysis strategy for 2D-TPP experiment employed bespoke thresholds, a minimal fold change of 1.5 at the highest ligand concentration and $R^2 > 0.8$ of the dose-response fits at two consecutive temperatures, to detect proteins affected by the ligand used in the experiment (Becher et al., 2016). However, this approach is inherently limited in sensitivity, does not inform on the false discovery rate (FDR) and does not account for varying noise levels across experiments.

To address these shortcomings, we developed a method termed Detection of Ligand-Protein Interactions from Thermal Profiles (DLPTP) which allows to analyze 2D-TPP experiments with FDR-control and high sensitivity. The approach we took was based on a nested modeling framework which fits for each protein i a null model, expected if the profiled ligand showed no effect on the thermal stability of protein i , and an alternative model which models the case of dose-dependent stabilization of protein i .

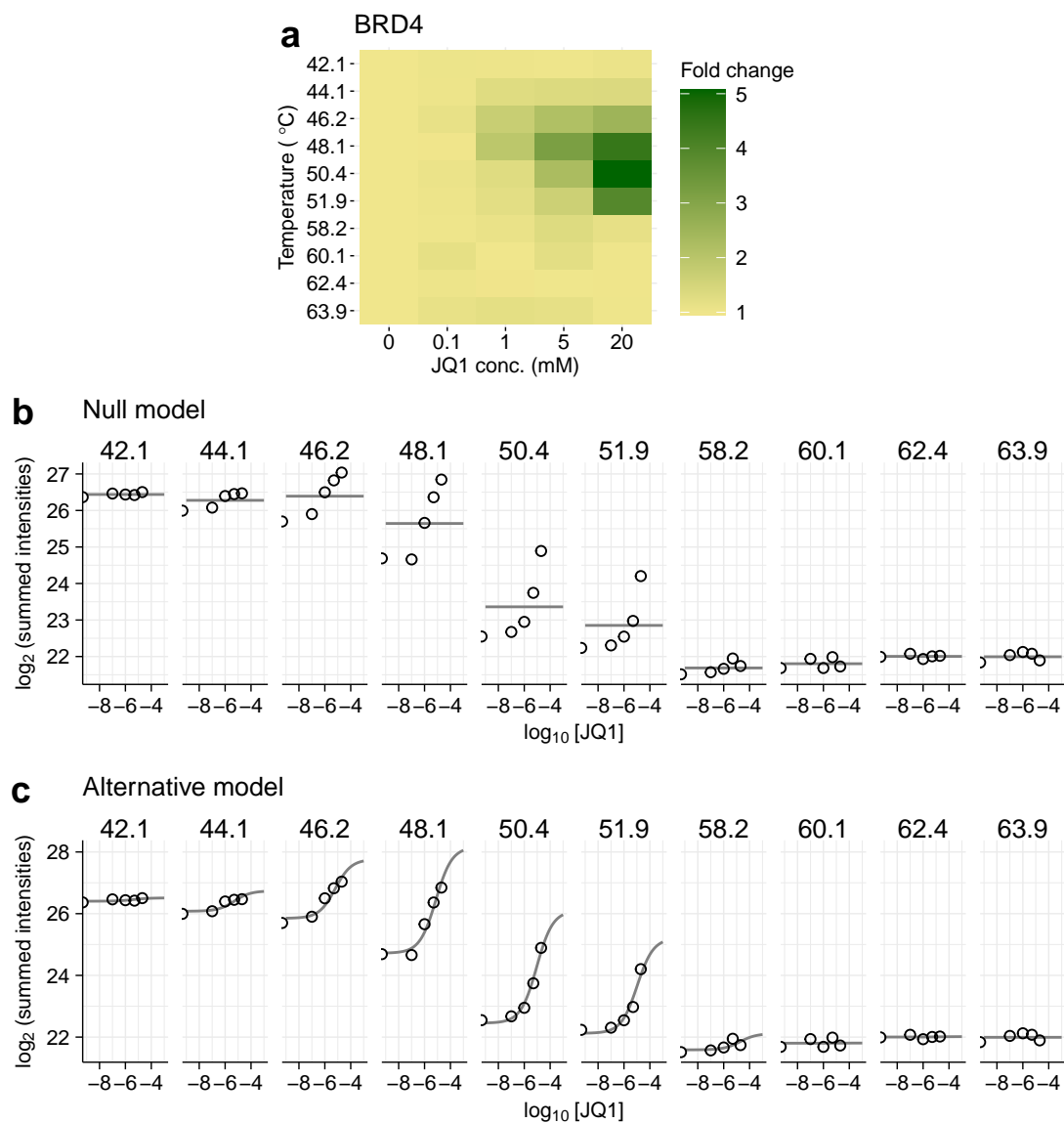


Figure 4.1: Illustration of data obtained from 2D-TPP experiments and design of DLPTP's nested models. a) Heatmap of relative fold changes at individual temperatures measured for BRD4 in the JQ1 HL60 lysate dataset. b) Null and c) alternative model fitted to log₂ intensity signal of BRD4 from the same dataset.

Both models were fit to the \log_2 intensity signal of protein i across temperatures and ligand concentrations. The null model was taken as a temperature-wise intercept model of the 2D-thermal profile of protein i (Figure 4.1a, Eq. 2.8). For the alternative model we designed a constrained dose-response model across temperatures (Figure 4.1b, Eq. 2.9). This was done by fitting the base level intensity at each temperature, a joint slope, but varying degrees of stabilization per temperature and an inflection point which was allowed to vary linearly across temperatures. Using the residual sum of squares (RSS) obtained for each model, we computed for each protein i an F -statistic (Eq. 1.2). Moreover, we implemented an empirical Bayes moderated version of obtained F -statistics. However, since residuals of both models were correlated and heteroscedastic, we could not directly use obtained F -statistics and theoretical degrees of freedom to compute p -values, adjust them for multiple testing and control for false discoveries. Thus, we adapted a bootstrapping approach from Storey et al. (2005), originally suggested for significance analysis of microarray timecourse experiments, and adjusted it to the specific noise structure of 2D-TPP data, i.e., we restricted resampling to measurements from the same MS experiment, to calibrate our F -statistics in terms of FDR. Since 2D-TPP datasets contain varying numbers of observations for different proteins, we applied this approach separately for groups of proteins with similar number of observations.

4.3 Benchmarking DLPTP on a synthetic dataset

To evaluate whether our implementation of DLPTP indeed controlled FDR as expected, we created a synthetic dataset composed of 5000 true negative thermal protein profiles simulated based on our null model with additional Gaussian noise observed for the real datasets and 80 known true positive profiles from various datasets (Becher et al., 2016; Mateus et al., 2018; Savitski et al., 2018; Sridharan et al., 2019). We then evaluated both, the standard and the empirical Bayes moderated version of DLPTP and compared their performance to the threshold-based approach (Figure 4.2). We found that both versions of DLPTP were able to control FDR at nominal levels. While the standard

version of DLPTP did not show a better sensitivity-specificity trade-off compared to the threshold-based approach, the moderated version was found to be more sensitive.

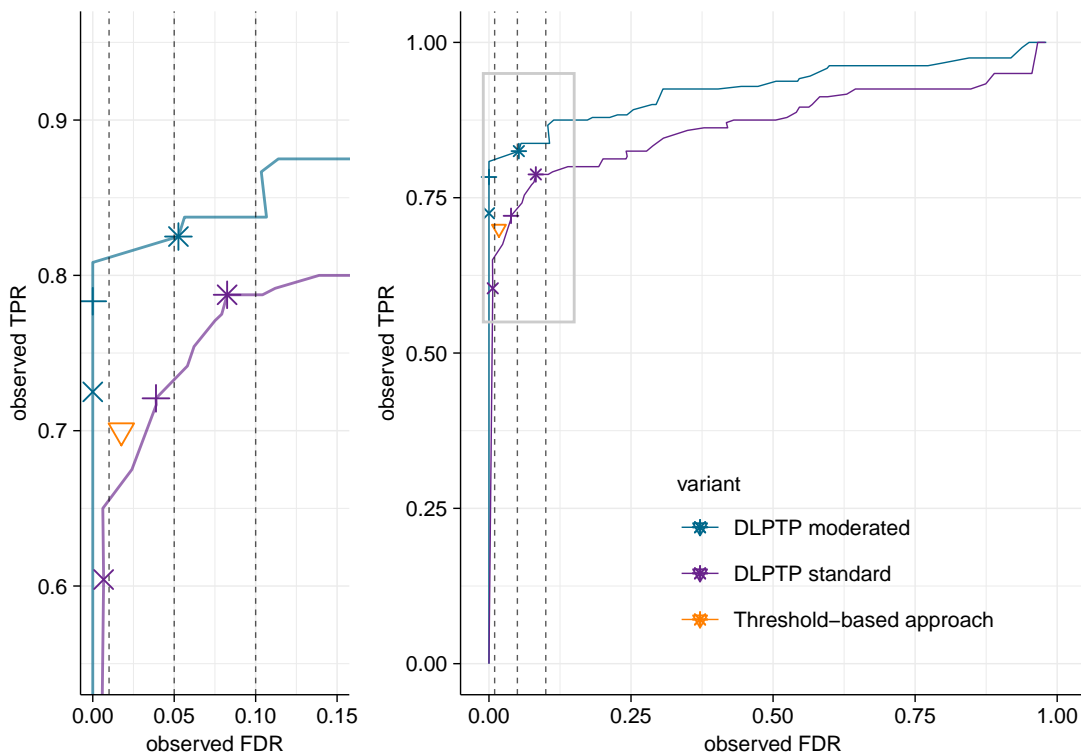


Figure 4.2: A benchmark of DLPTP with a synthetic dataset confirms FDR control and improved sensitivity compared to the threshold-based approach. TPR vs. FDR curve of the different compared methods for 2D-TPP analysis. Dashed lines correspond to 1, 5 and 10% nominal FDR.

4.4 Application of DLPTP to published 2D-TPP datasets

To further explore our method we reanalyzed two previously published 2D-TPP datasets. First, the first published 2D-TPP experiment profiling the pan-HDAC inhibitor Panobinostat in intact HepG2 cells (Becher et al., 2016) and second a 2D-TPP dataset of the BRD4 inhibitor JQ1 in HL60 lysate (Savitski et al., 2018).

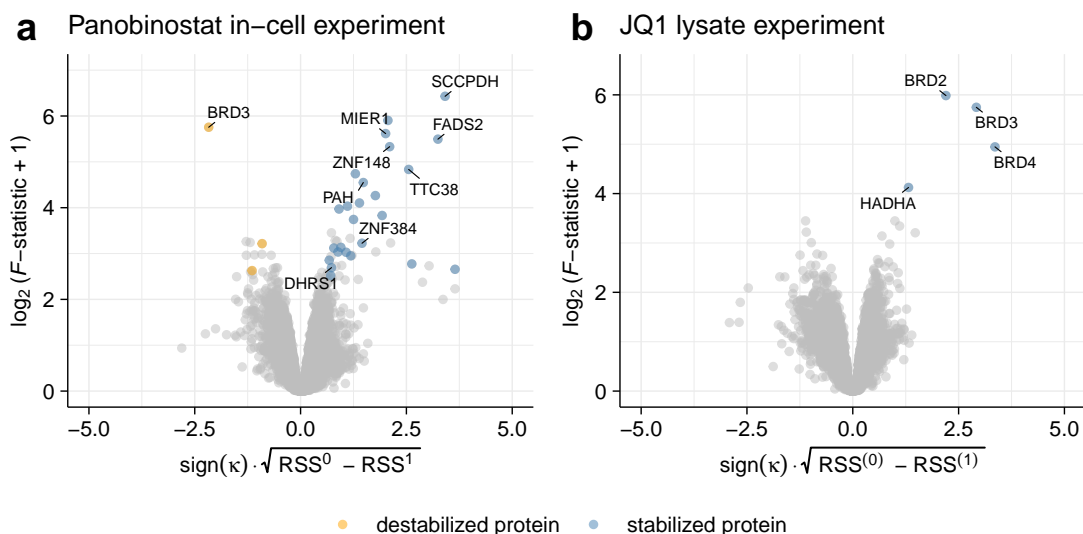


Figure 4.3: DLPTP recovers known drug-binding proteins based on published datasets. Volcano plots of DLPTP results obtained for the a) Panobinostat in-cell and the b) JQ1 lysate dataset. The effect size is taken as $\text{sign}(\kappa) \cdot \sqrt{\text{RSS}^{(0)} - \text{RSS}^{(1)}}$ which describes how much more variance is explained by the alternative versus the null model, signed by the direction of the effect, i.e., stabilization of destabilization. The F -statistic on the y-axis is transformed as described to guarantee that transformed values remain bounded as F approaches 0. Colored points represent proteins found significantly affected in thermal stability at 10% FDR.

The DLPTP analysis of the Panobinostat dataset (Figure 4.3a) revealed all so far described on- and off-targets of the drug: HDAC1, HDAC2, TTC38, PAH, FADS1 and FADS2, except for HDAC6 which featured noisy measurements at the highest and second highest temperature which prevented the alternative model from achieving a fit with small enough residual error despite of the presence of a dose-response trend. Additionally, we could identify the zinc finger transcription factor ZNF148 which has been described recently to be amenable for Panobinostat binding and DHRS1 which is likely indirectly affected by Panobinostat (Perrin et al., 2020). Both of these proteins could not be identified as significantly affected by the drug by previous analysis of this dataset.

The reanalysis of the JQ1 dataset revealed the chemical probe’s previously described targets (Savitski et al., 2018): the BET transcriptional regulators BRD2, 3 and 4 and HADHA, a mitochondrial trifunctional enzyme with acetyl-transferase activity, but not the off-targets SOAT1 and FYTDD1.

4.5 Target Profiling of the HDAC8-inhibitor PCI-34051

Next, we turned to a 2D-TPP dataset profiling the HDAC8 inhibitor PCI-34051 (Figure 4.4a), a compound reported to be effective against different forms of T-cell leukemia (Balasubramanian et al., 2008). By analyzing the dataset with DLPTP, we identified 154 proteins which significantly changed in thermal stability (Figure 4.4b). A gene ontology analysis revealed that the hits were enriched for the biological process terms ‘oxidation–reduction process’ (hypergeometric test, $p_{\text{adj.}} = 5 \cdot 10^{-11}$, odds ratio: 3.5) and ‘carboxylic acid metabolic process’ (hypergeometric test, $p_{\text{adj.}} = 7 \cdot 10^{-6}$, odds ratio: 2.8). Proteins belonging to these groups are likely not direct targets of the drug, but rather involved in the metabolic response to the compound. In addition to proteins which reflected these gene sets, we found the target of PCI-34051, HDAC8 ($\text{pEC}_{50}^{\text{PCI-34051}} = 6.4$), and unexpectedly, Leucine aminopeptidase 3 (LAP3; also called Cytosol aminopeptidase; $\text{pEC}_{50} = 5.9$), a Zn^{2+} -dependent metallopeptidase, in the group of most significantly affected proteins. LAP3 expression was reported to correlate with malignant development of hepatocellular carcinoma (Tian et al., 2014) and its inhibition was observed to limit invasion of ovarian cancer cells (Wang et al., 2015). Thus, LAP3 constitutes a potentially interesting target for therapy of different cancer entities.

To further investigate our discovery of LAP3 as potential off-target of PCI-34051, another 2D-TPP experiment was performed on BRD-3811 (Figure 4.4c), an analog of PCI-34051 which is sterically hindered to bind to HDAC8 by its additional methyl group (Olson et al., 2014), to assess whether BRD-3811 could be a specific inhibitor of LAP3.

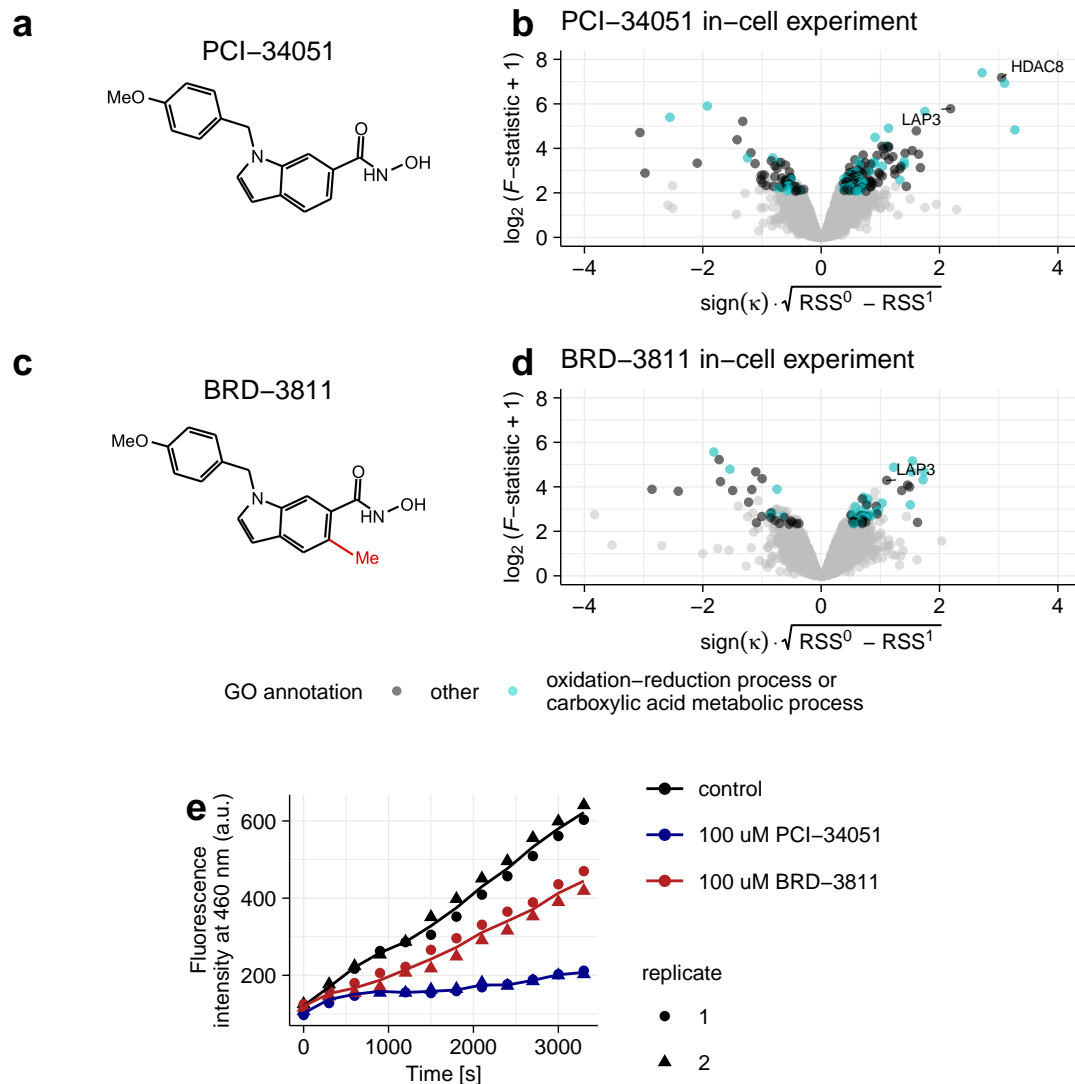


Figure 4.4: Target profiling with 2D-TPP of the HDAC8 inhibitor PCI-34051 and its analog BRD-3811. a) Chemical structure of PCI-34051. b) Volcano plot obtained by DLPTP analysis of a PCI-34051 2D-TPP experiment. c) Chemical structure of BRD-3811. d) Volcano plot obtained by DLPTP analysis of a BRD-3811 2D-TPP experiment. e) Leucine aminopeptidase *in vitro* assay shows inhibition of LAP3 by PCI-34051 and BRD-3811. Time course measurement of an fluorescent reporter of recombinant LAP3 peptidase activity in the presence of PCI-34051, BRD-3811 or solvent control.

When analyzing the obtained dataset with DLPTP, HDAC8 was not found to be stabilized, as expected. However, LAP3 was found to be significantly affected in its thermal stability also by BRD-3811 (Figure 4.4d). In order to determine whether enzymatic activity of LAP3 was inhibited in the presence of either of the two compounds, a fluorometric aminopeptidase assay was performed with recombinant LAP3 in the presence of 100 μ M PCI-34051, BRD-3811 or solvent control. Indeed, a slower increase in fluorescent signal, reflecting attenuated peptidase product accumulation, could be observed in the presence of both compounds (Figure 4.4e). The effect was weaker for BRD-3811, resembling the lower pEC₅₀ of LAP3 stabilization, obtained for the compound by 2D-TPP (pEC₅₀^{BRD-3811} = 5.0). This could mean that the additional methyl group in BRD-3811 dampens the binding to LAP3 which likely also works via Zn²⁺ chelation at the active site of the enzyme.

4.6 DLPTP analysis of 2D-TPP experiments in rat tissues and human blood

The ability to assess drug distribution to different organs and tissue-specific target engagement *in vivo*, is highly desirable in the pre-clinical drug discovery process. It allows to determine whether a drug reaches the destined tissue and whether it specifically engages its molecular target. These insights are invaluable to evaluate drug safety and efficacy.

To establish the application of TPP in an *in vivo* and an *ex vivo* setting we collaborated with colleagues from GSK/Cellzome. Whereas *in vivo* experiments with drug versus vehicle dosed rats were performed in a similar setup as TPP-TR experiments (not reported in this thesis), respective *ex vivo* experiments, were performed on rat organs and on human blood in 2D-TPP format (Perrin et al., 2020). These experiments were performed by sacrificing untreated rats, extracting different tissues, i.e., testis or spleen, and treating different tissue pieces with different concentrations of a compound, followed by

heating and extraction, and profiling of soluble proteins. All of these experiments were done in replicates, since these experiments were expected to be more noisy compared to cell culture based experiments.

Thus, we devised a strategy to apply DLPTP to 2D-TPP experiments with replicates. This was implemented by running DLPTP on each replicate of the same experiment separately using 100 rounds of bootstrapping each. Replicates were then integrated by requiring each protein to be replicated and selecting the lowest observed F -statistic across the two replicates for each protein in the true dataset and each round of the bootstrapped dataset. FDR was then computed on this combined dataset with the same approach as for a single dataset (Eq. 2.13 and 2.14). We applied this approach to all datasets of this study.

4.6.1 *Ex vivo* 2D-TPP experiments in rat tissues

For the *ex vivo* experiment in rat testis profiling the BRAF-inhibitor Vemurafenib, a drug approved for late stage melanoma therapy, we observed specific stabilization of Braf (rat homolog of human BRAF), but also destabilization of the kinase Ulk4 which was not reported as a target of the drug so far. However, the known off-target ferrochelatase (Fech) (Savitski et al., 2014) was identified, but was not found to be significantly altered in thermal stability.

Next, we analyzed the 2D-TPP experiment profiling Panobinostat in rat spleen punches (Figure 4.5b). We observed the known targets Hdac1, Hdac2 and its off-target Ttc38. Additionally, Dhrr1 was found to significantly stabilize. We had also identified DHRS1 (human homolog) in the HepG2 in-cell 2D-TPP experiment with Panobinostat (Figure 4.3a) and wondered whether the oxidoreductase was a direct off-target of the drug or whether it could be a molecule derived from metabolism of Panobinostat that bound to Dhrr1 and stabilized it (Figure S3). Hence, to test whether Dhrr1 was a direct target of Panobinostat or one of its metabolism products, we purified, recombinantly expressed human DHRS1 and performed differential scanning fluorimetry. This was done in the

presence of Panobinostat, some of its metabolites and solvent control. However, we found no apparent difference in thermal stability for any of the compounds compared to control, which would have indicated a direct interaction of any of the molecules with DHRS1 (Figure 4.5c). Thus, we performed a TPP experiment in rat liver lysate with a reduced design to test multiple compounds in two multiplexed TMT MS experiments. These experiments were done with only one vehicle control reference channel at 37°C and all other channels at 50°C (a temperature close to the melting point of DHRS1 (Jarzab et al., 2020)) in the presence of vehicle control, Panobinostat or metabolized forms of the drug at two concentrations. As in the previous experiment, we could not observe any effect on Dhhr1 thermal stability by any of the tested compounds, but saw thermal stabilization of Hdac2 at both concentrations of panobinostat and one of its metabolized forms T27c, which still contains the hydroxamic acid group involved in target engagement (Figure 4.5d). Hence, the thermal stabilization of Dhhr1 in rat spleen could not be explained by a direct interaction with Panobinostat, we hypothesized that it might thus be induced indirectly, e.g. by a cellular process triggering activation of Dhhr1. Since Dhhr1 is known to be dependent on NADP binding to function (Zemanová et al., 2019), we performed another reduced TPP experiment in rat liver lysate in the presence of further metabolized forms of Panobinostat and NADP, this time not at different concentrations, but at different temperatures around the melting point of DHRS1 in human cell lines (~ 50°C) (Jarzab et al., 2020). This time we observed only stabilization of Dhhr1 in the presence of NADP, but not for any of the other compounds (Figure 4.5e). We thus concluded that Panobinostat treatment in metabolically active cells or tissues likely induced a cellular process triggering a change of the biophysical state of Dhhr1, possibly related to stronger binding to NADP.

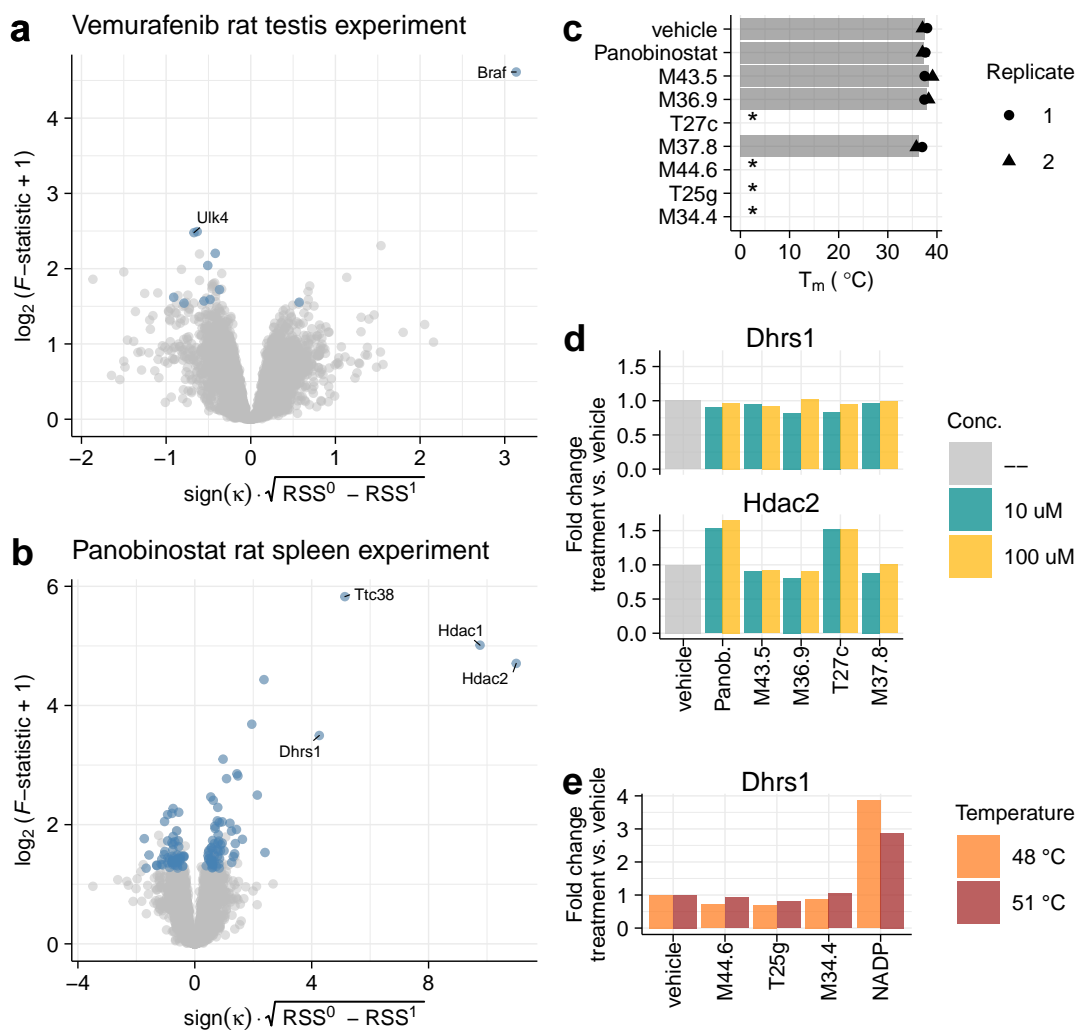


Figure 4.5: DLPTP analysis of 2D-TPP experiments performed in rat tissues. Volcano plots of *ex vivo* 2D-TPP experiments of a) Vemurafenib in rat testis and b) Panobinostat in rat spleen. c) Melting points obtained for purified, recombinantly expressed DHRS1 by differential scanning fluorimetry in the presence of different compounds. *: Not measurable due to autofluorescence. d-e) Fold changes obtained from TPP experiments in S9 rat liver extract for d) Dhars1 and Hdac2 at 50°C in the presence of different concentrations of Panobinostat and different metabolized forms compared to vehicle control and e) for Dhars1 at 48 and 51°C in the presence of a different set of Panobinostat derivatives (100 μ M) than in d) and NADP (0.4 mM) compared to vehicle control.

4.6.2 2D-TPP experiment in human blood

The datasets of 2D-TPP performed directly in human blood were obtained by performing the drug- and subsequent heat treatment on fresh blood samples, followed by centrifugation and extraction of primary blood mononuclear cells, extracting remaining soluble proteins from those cells and measuring them by LC-MS/MS analysis.

In the experiment featuring Panobinostat we were able to find several of the previously described (off-)targets such as HDAC1, HDAC2, HDAC6 and TTC38. In addition, the zinc finger transcription factor ZNF512 was found to significantly stabilize in the presence of Panobinostat (Figure 4.6a). This is in line with the reported Zn^{2+} chelation activity mode of Panobinostat's hydroxamic acid group. However, we also found a high fraction of members of the large and small ribosome to significantly destabilize in this experiment. This has not been observed before in cell line-based experiments (Figure 4.3a) and seemed to be an artifact of this particular experiment, since we did not observe similar effects in the JQ1 2D-TPP experiment in human blood (Figure 4.6b).

For JQ1 profiled in human blood, we could identify the cognate targets BRD2, 3 and 4 as significantly stabilized. Moreover, as in the cell lysate experiment (Figure 4.3b), we found HADHA and this time also its binding partner HADHAB to be significantly altered in thermal stability.

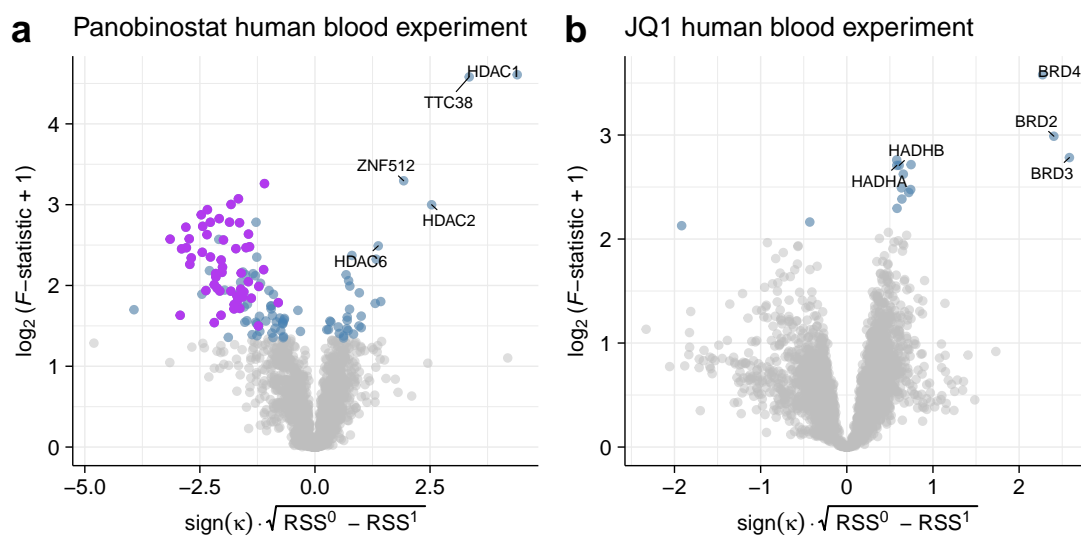


Figure 4.6: DLPTP analysis results for 2D-TPP datasets obtained with human blood. Volcano plots of results obtained for the datasets of a) Panobinostat and b) JQ1 profiled in human blood. Blue dots represented proteins found with significantly altered thermal stability at 10% FDR. Purple points in panel a) represent members of the large and small ribosome subunits.

4.7 Conclusion

Here, a novel statistical method for analysis of 2D-TPP experiments—DLPTP—was presented. The concept of curve-based hypothesis testing tailored to thermal profiles enabled the first approach for 2D-TPP analysis with control of the the false discovery rate. The method’s performance was assessed on a synthetic dataset and it was found to outperform the previous analysis approach by being more sensitive at the same specificity. Application of DLPTP to published 2D-TPP datasets found known on- and off-targets of the profiled drugs and thus further validated our approach. The analysis of a 2D-TPP dataset profiling the HDAC8 inhibitor PCI-34051 found an off-target of the drug: LAP3 which is a potentially interesting target for therapy of different cancer entities. BRD-3811, an analog of the compound which does not bind HDAC8, was found to also bind and inhibit LAP3. Hence, BRD-3811 could be a starting point drug candidate

for specific, high affinity inhibitors of LAP3 that could be used for certain subtypes of ovarian and liver cancer.

Lastly, we applied DLPTP to different datasets obtained with the recently developed *ex vivo* realization of 2D-TPP which allows to profile drugs directly in animal tissues of interest or in human blood. Also for these datasets, we were able to detect the reported targets of the profiled drugs and additionally observed downstream effects such as modulation of the oxidoreductase *Dhrs1* which was found to stabilize significantly in rat spleen upon treatment with Panobinostat.

Chapter 5

Applying thermal proteome profiling to study protein-metabolite interactions

“Measure what is measurable and make measurable what is not so.”

— Galileo Galilei

Metabolites fulfill a myriad of functions in cells, such as storing energy and regulating protein function (Rinschen et al., 2019). However, protein-metabolite interactions often lie on the transient, low affinity side of biochemical interactions, making them particularly hard to study in relevant biological contexts (Reznik et al., 2017). In this chapter, the application of TPP to study protein-metabolite interactions is described based on the example of ATP and GTP. Mapping protein interactions of these nucleotide metabolites served both as a proof of concept with previous literature knowledge to validate observations, as well as a resource giving new insights into intracellular regulatory roles of these molecules (Sridharan et al., 2019).

5.1 2D-TPP experiments of ATP and GTP in crude lysate

Intracellular nucleotide levels are tightly regulated and are thus difficult to modulate experimentally (Tsuura et al., 1999). Hence, we performed 2D-TPP experiments with mechanically disrupted Jurkat cells, to generate an as close as possible system to the intact cell scenario. With these lysates we performed 2D-TPP experiments with ATP and GTP (Figure S5a and b) using distinct dose ranges (ATP: solvent control + 0.005-2 mM; GTP: solvent control + 0.001, 0.01-0.5 mM) reflecting the different intracellular concentrations of the two nucleotides (ATP: \sim 1-10 mM; GTP: \sim 0.1-1 mM) (Traut, 1994). These experiments were performed in triplicates and thus our DLPTP analysis strategy for incorporation of replicates was applied to analyze obtained datasets. Based on the volcano plots obtained from the ATP and GTP experiments (Figure 5.1a and b), a high fraction of proteins with associated GO terms ‘ATP binding’ and ‘GTP binding’ were found to be significantly affected in thermal stability. Indeed, both were found to be significantly enriched (hypergeometric test $p < 2.2 \cdot 10^{-16}$ and odds ratio: 3.2 for ATP-binders in the ATP dataset and $p < 2.2 \cdot 10^{-16}$ and odds ratio: 17.5 for GTP in the GTP dataset). However, we also found a significant enrichment of the respective other nucleotide in both datasets, i.e., GTP binder enriched in the ATP dataset (hypergeometric test $p = 4.1 \cdot 10^{-4}$ and odds ratio: 2.1) and ATP binders enriched in the GTP dataset (hypergeometric test $p < 2.2 \cdot 10^{-16}$ and odds ratio: 3.0). This reflected previously reported cross-talk between the two metabolites observed in *E. coli*, i.e., ATP binding to GTP-binders and vice versa (Piazza et al., 2018).

Next, we took a closer look at the obtained pEC₅₀ values, i.e., the effective thermal stabilization concentrations, of the two metabolites on proteins of different ontology groups (Figure 5.1a and b). As expected, we found that, for both datasets, proteins known to bind to the respective nucleotides showed the highest effective stabilization concentrations. However, the difference between ATP binders and GTP binders was much lower in the experiment profiling ATP than in the one of GTP. This could be related to the difference in intracellular concentrations of both metabolites.

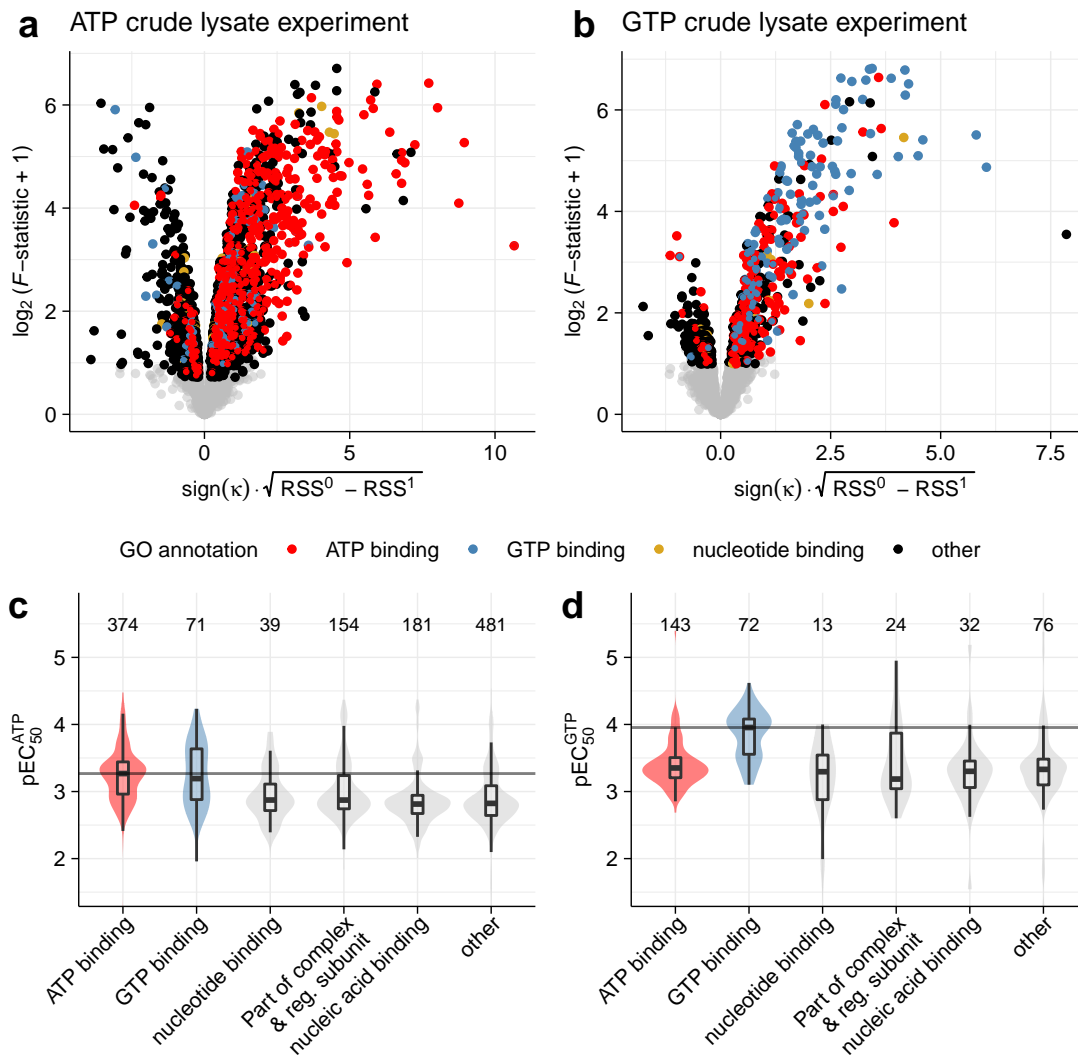


Figure 5.1: DLPTP analysis results for the 2D-TPP experiments profiling ATP and GTP in crude lysate. Volcano plots of DLPTP analysis results for the a) ATP and b) GTP dataset. Violin plots of distributions of effective stabilization concentrations (pEC₅₀) of different group of proteins found to be stabilized by c) ATP and d) GTP.

Since GTP is present in cells at much lower concentrations than ATP, GTP binding proteins need a higher affinity and specificity for GTP to ensure binding to the right nucleotide in excess presence of ATP.

5.2 Indirectly induced thermal stability effects by ATP

Interestingly, many proteins from other functional groups were also found to stabilize. While we were less surprised to observe proteins annotated to bind to other nucleotides or nucleic acids, due to the similarity to ATP and GTP, the many regulatory subunits and members of protein complexes with subunits that were nucleotide binders were unexpected. Thus, we took a closer look at this phenomenon. The proteasome represented an interesting examples (Figure 5.2a): while the 19S proteasome (the regulatory particle) features several ATPases in its base (“C”-subunits), the 20S proteasome (core particle) does not feature any annotated ATP-binding subunits. In Jurkat cells both subcomplexes aggregate distinctly, but show coaggregation of their respective subunits to a large extent (Figure 5.2b). We used these curves to compute pairwise Euclidean distances between individual subunits and observed that non-ATP binding proteasome subunits in close physical proximity, i.e., as inferred by low Euclidean distance of melting curves, to an ATP-binding one where co-stabilized in the presence of ATP (Figure 5.2c). This led us to hypothesize that ATP binding to subunits of complexes can costabilize nearby subunits. To test this hypothesis, we revisited the TPCA concept (introduced in Chapter 3) to compute Euclidean distances (ED) of protein pairs annotated to be part of the same complex using a Jurkat intact cell TPP-TR experiment (Jarzab et al., 2020). We then asked whether the median ED of non-ATP binding annotated proteins, which stabilized with ATP, to an ATP-binding subunit within the same complex was lower than for non-ATP binding annotated proteins, which did not stabilize in the presence of ATP. Indeed, we found that this was true, when testing across all complexes annotated by Ori et al. (2016) (Figure 5.2d).

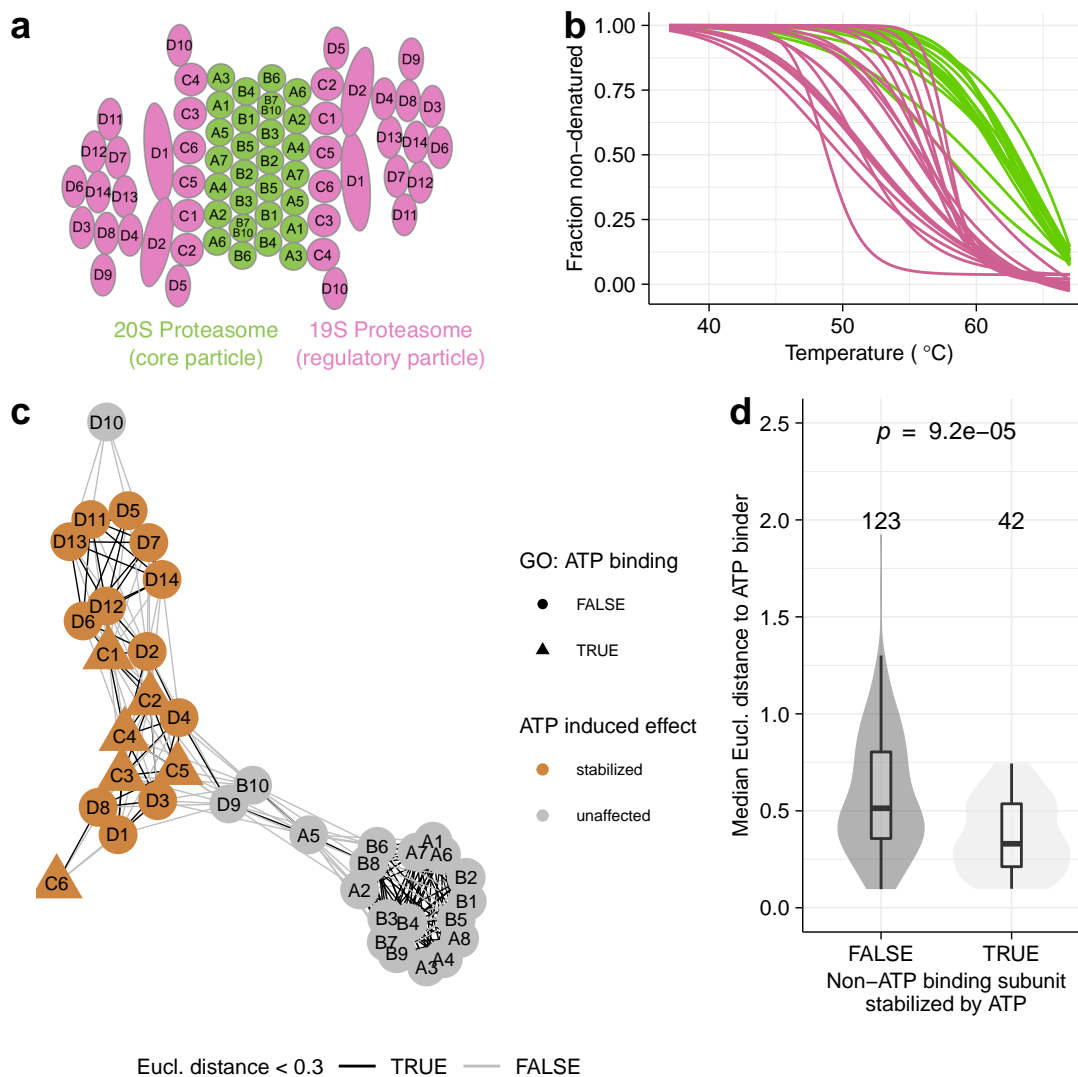


Figure 5.2: Co-stabilization of complex subunits by ATP. a) Schematic of the 26S proteasome and its subcomplexes (figure adapted from Becher et al. 2018, with permission based on its license). b) Melting curves of subunits of the proteasome. c) Network of protein-protein interactions within the proteasome showing the effect of ATP on subunit thermal stabilities. d) Violin plot of across complex comparison of median Euclidean distances between melting curves of non-ATP-binding annotated subunits found stabilized or unaffected by ATP and ATP-binding annotated subunits in the same complexes. Significance assessed by Wilcoxon rank sum test.

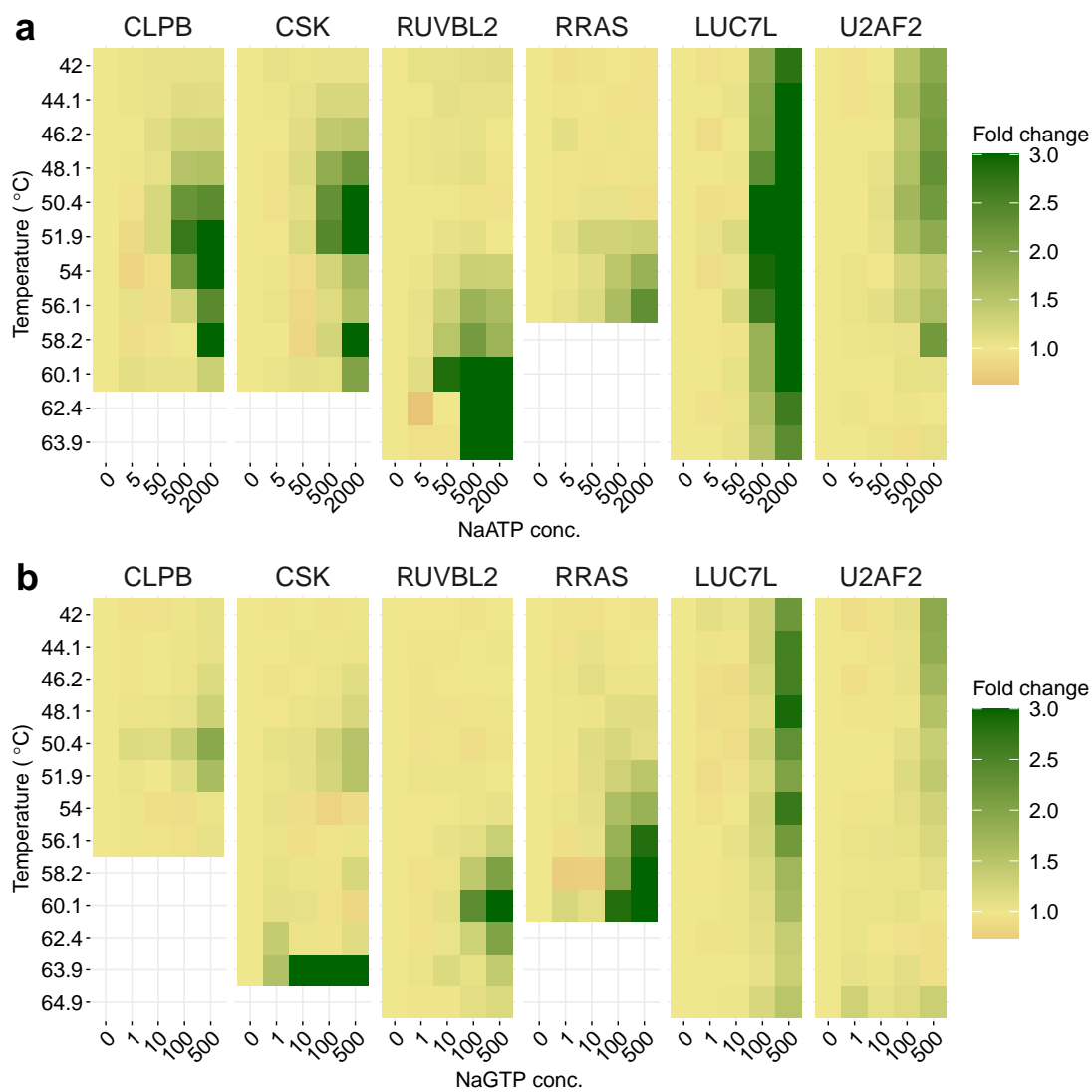


Figure 5.3: Exemplary heatmaps of ATP and GTP induced stability fold changes at different temperatures. Average relative fold change 2D profiles of selected proteins obtained for a) ATP and b) GTP. For visualization purposes fold changes higher than 3 were ceiled at 3.

Next, we took a step back and inspected the thermal profiles of proteins with significant thermal stability effects for ATP and GTP more closely. For proteins annotated as ATP-binders, but stabilized by both ATP and GTP (CLPB and CSK) and GTP-binders stabilized by both GTP and ATP (RRAS or RUVBL2), we found that the respective nucleotide annotated to bind the protein showed stronger and more potent stabilization, as expected (Figure 5.3a and b). However, especially for many RNA-binding proteins, such as LUC7L and U2AF2, we noted that many of them did not feature a typical stabilization pattern at higher temperatures, but rather from the lowest temperature onward (Figure 5.3a and b). The only explanation we could find for this phenomenon was, that at high concentrations, ATP and GTP could solubilize insoluble subpopulations of these proteins. This notion was reinforced by a recent report stating ATP could act as a biological hydrotrope (Patel et al., 2017) and expression changes could not be the reason for this observation, as these experiments were performed in lysates. To follow up on this hypothesis, we devised a new experimental approach termed Solubility Proteome Profiling (SPP).

5.3 Profiling proteome-wide ATP-induced solubilization of insoluble subpopulations

In order to measure soluble and insoluble subpopulations of proteins in crude lysates and the effect of a compound (ATP in this case) on the insoluble pool, we devised a new strategy termed SPP (Figure 5.4). By multiplexing both, a channel in which the proteome was extracted with a mild detergent (NP-40), which preserves insoluble proteins, and a channel for which a strong detergent (SDS) was used, we could monitor both the soluble and the total proteome. Additionally, we added channels in which proteins were extracted with NP-40 and a dose range of ATP (0.1-10 mM). To test for both, proteins which had an insoluble subpopulation and proteins which were solubilized by ATP, we used the R package `limma` to find proteins with significant signal intensity

changes between the SDS and NP-40 control and the 10 mM ATP and NP-40 control channel, respectively. The results of the analyses of this dataset are shown in Figure 5.5a. By comparing total (SDS) versus NP-40 soluble proteins, we found that 16% of the proteome (1063 out of 6522 proteins quantified by at least two peptides in at least two replicates) had a significant insoluble subpopulation, which was at least half the amount of the soluble population ($p_{\text{adj}} < 0.01$ and $r_{\text{SDS/NP-40}} \geq 1.5$).

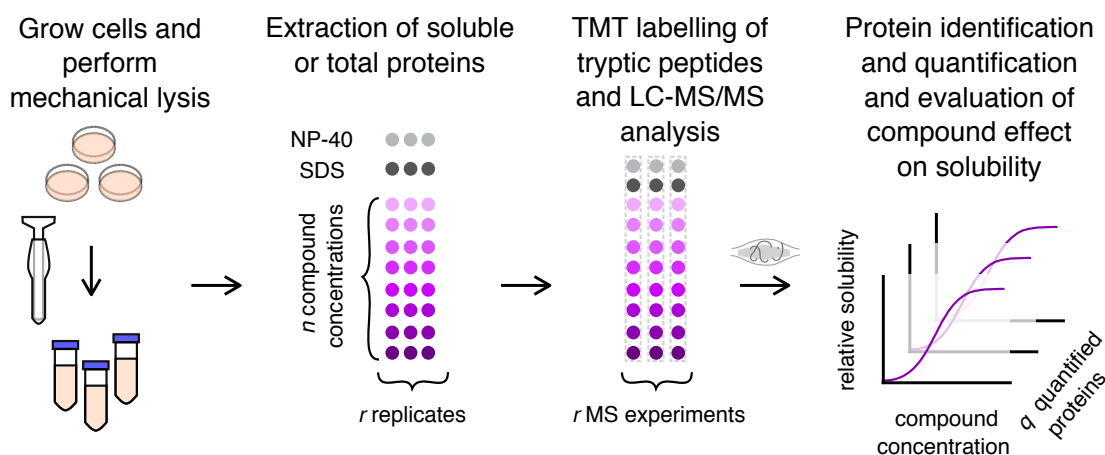


Figure 5.4: Schematic of the experimental workflow for Solubility Proteome Profiling. Cells are grown and disrupted mechanically using a Dounce homogenizer. Proteins are then extracted from crude lysates with either SDS or NP-40 alone, or with NP-40 and a concentration range of a compound. Extracted proteins are measured by LC-MS/MS analysis, identified by database search and quantified. By testing for intensity differences between the highest compound concentration channel and the NP-40 control channel, proteins with altered solubility are identified. Effective solubilization concentrations are then determined for significantly affected proteins by fitting of dose-response curves.

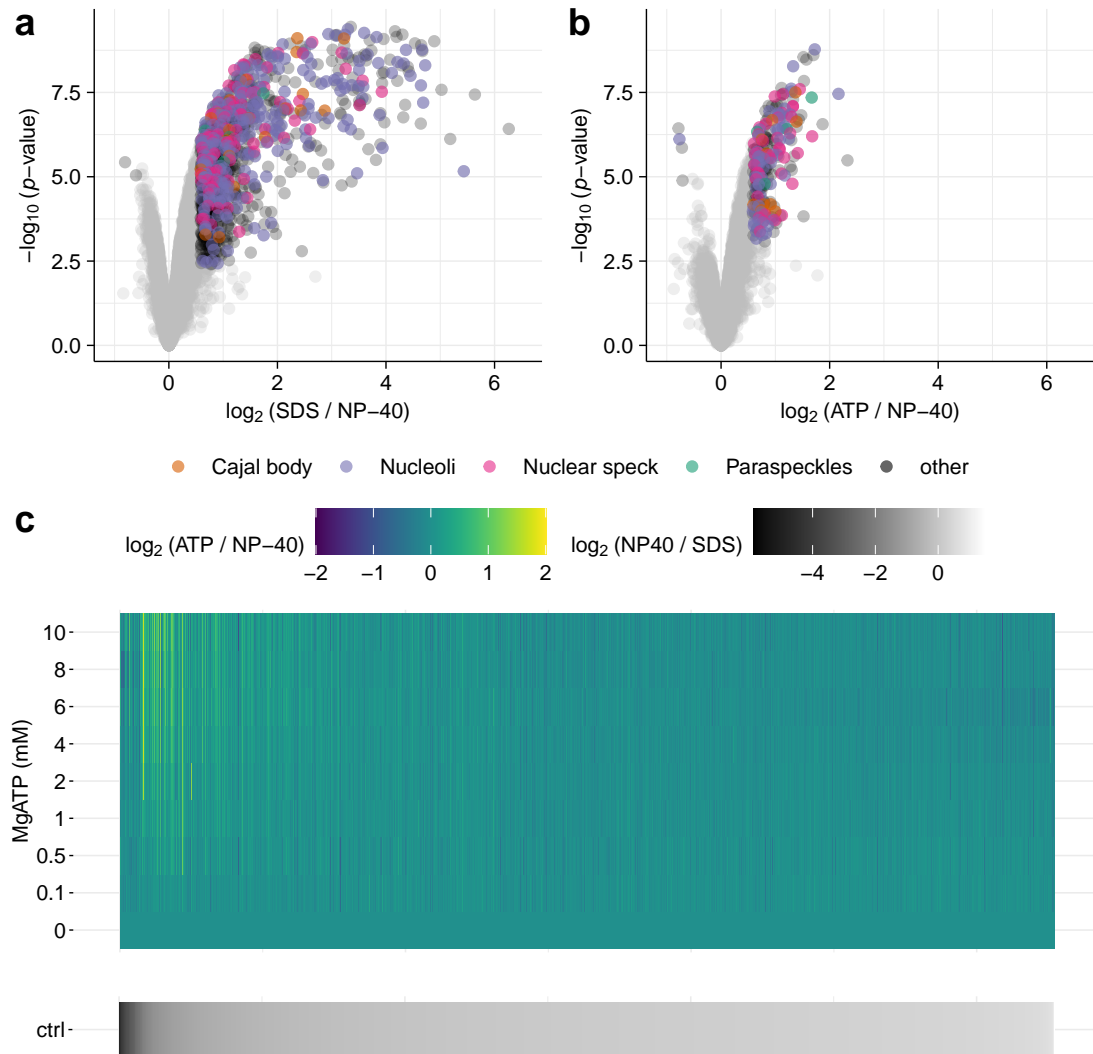


Figure 5.5: SPP experiments inform on insoluble subpopulation and solubilizing effect of ATP. Volcano plots obtained from `limma` analysis of the SPP data comparing a) the SDS vs. the NP-40 control and b) the 10 mM ATP vs. the NP-40 control channel ($p_{\text{adj.}} < 0.01$ and $\log_2(\text{fc}) > \log_2(1.5)$). c) Heatmap of the channels with different ATP concentrations. The black to light gray bar indicated the fraction of insolubility as measured by the SDS vs. NP-40 comparison.

Proteins with a significant insoluble fraction enriched for the cellular compartment GO terms ‘nuclear body’ ($p_{\text{adj}} < 2.2 \cdot 10^{-16}$, odds ratio: 3.0), ‘ribosome’ ($p_{\text{adj}} < 2.2 \cdot 10^{-16}$, odds ratio: 12.2), ‘preribosome’ ($p_{\text{adj}} < 2.2 \cdot 10^{-16}$, odds ratio: 42.1) and ‘nuclear speck’ ($p_{\text{adj}} < 2.2 \cdot 10^{-16}$, odds ratio: 4.8, all determined with hypergeometric tests). The interpretation of these terms became more clear when considering that the enriched GO term ‘nuclear body’, comprises terms, as ‘PML body’, ‘paraspeckles’, ‘Cajal body’, and ‘nuclear speck’. The enrichment of ribosomal proteins, especially preribosomal ones, in addition, could be due to the fact that they are produced and assembled in the nucleolus, another membrane-less compartment. Taken together, this indicated that our SPP experiment informed on insoluble subpopulations of proteins which were, to a large extent, part of membrane-less organelles (Banani et al., 2017).

From the comparison of the 10 mM ATP with the NP-40 condition (Figure 5.5b), we found 218 proteins, of which 216 were previously found to have a significant insoluble subpopulation, which significantly solubilized with ATP. These proteins were also enriched for the cellular compartment GO terms ‘nuclear body’ ($p_{\text{adj}} < 2.2 \cdot 10^{-16}$, odds ratio: 5.0), ‘nuclear speck’ ($p_{\text{adj}} < 2.2 \cdot 10^{-16}$, odds ratio: 6.5), ‘fibrillar center’ ($p_{\text{adj}} = 7.4 \cdot 10^{-9}$, odds ratio: 8.5) and ‘preribosome’ ($p_{\text{adj}} = 3.0 \cdot 10^{-6}$, odds ratio: 7.5) indicating that 10 mM ATP solubilized parts of membrane-less organelles. By integration of the results obtained from all ATP treated channels with both NP-40 and SDS control channels (Figure 5.5c), we observed that, except for a small group with the highest fraction of insolubility, ATP affected a large part of proteins with considerable insoluble subpopulations.

Next, we made use of all measured channels with different ATP concentrations to compute dose-response curves for the solubilization of those proteins which were found to be significantly affected by ATP. This allowed us to estimate the *effective solubilization concentration* (pESC_{50}), at which the half maximal solubilization effect was observed. We saw that these values varied strongly between different proteins (Figure 5.6 a-c). For the Barrier-to-autointegration factor (BANF1), a DNA-binding protein involved in chromatin organization, we observed one of the highest effective solubilization concentration $\text{pESC}_{50}^{\text{BANF1}} = 3.5$ (Figure 5.6 a).

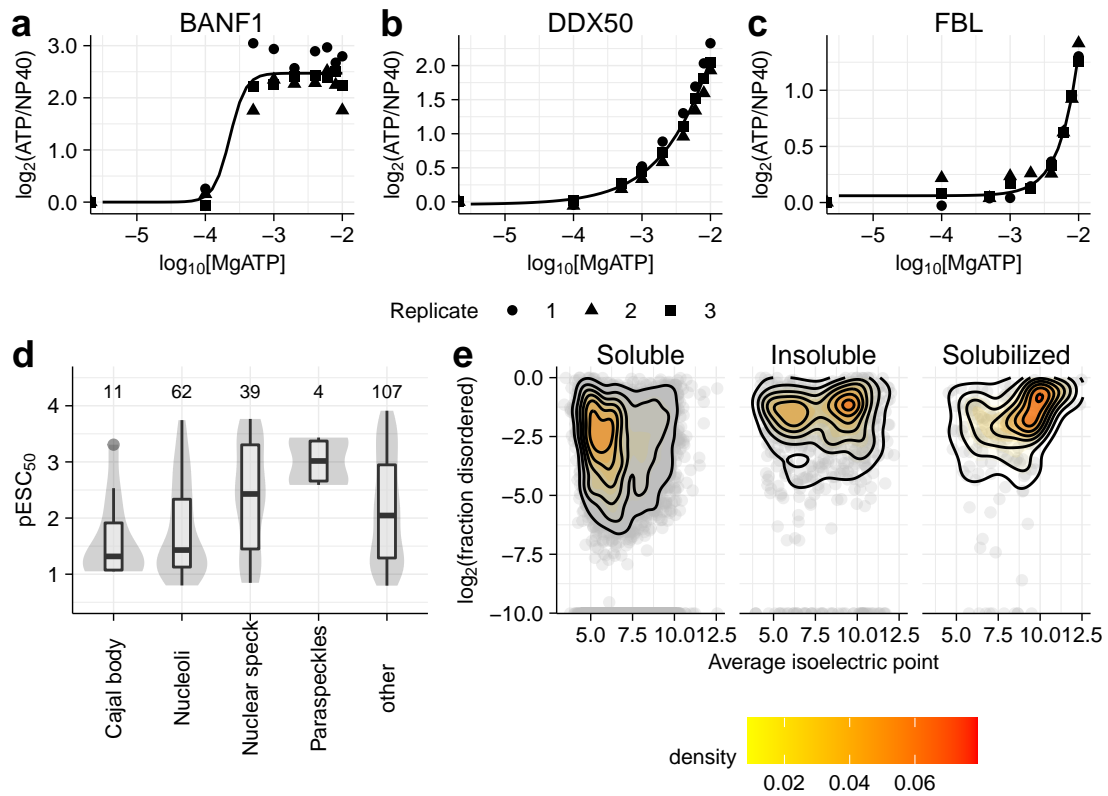


Figure 5.6: Susceptibility for solubilization by ATP varies across membrane-less organelles. ATP concentration-dependent solubility profiles of a) BANF1, b) DDX50 and c) FBL. d) Violin plot of effective solubilization concentrations (pESC₅₀) of proteins localizing to different membrane-less organelles. e) 2D density plots of soluble, insoluble and ATP-solubilized proteins with average isoelectric points vs. fraction disorder.

The proteins DDX50 and FBL localizing to nucleoli and Cajal bodies, respectively, showed lower pESC_{50} values ($\text{pESC}_{50}^{\text{DDX50}} = 1.2$ and $\text{pESC}_{50}^{\text{FBL}} = 1.3$), indicating higher required ATP concentrations for solubilization (Figure 5.6 b and c). This led us to systematically compare pESC_{50} values for different membrane-less organelles. We observed that paraspeckles needed the lowest ATP concentrations to be solubilized, followed by nuclear speckles and nucleoli, and Cajal bodies requiring the highest concentrations (Figure 5.6 d). This made us wonder which molecular features defined proteins with insoluble subpopulations and those which were solubilized by ATP.

Since the proteins we found affected in their solubility by ATP were mostly not annotated binders of the nucleotide, and as ATP is a highly negatively charged molecule, we hypothesized that positively charged proteins were more likely to be affected by it. Moreover, phase separation of membrane-less organelles has been reported to be driven by proteins with a high fraction of intrinsically disordered regions (Feric et al., 2016). Thus, we plotted all proteins confidently quantified in our SPP experiment into a 2D space defined by disordered protein sequence fraction and average protein isoelectric points (Figure 5.6 e). From the 2D density plot we observed that proteins with a primarily soluble population were spread out broadly in the 2D space, with a tendency towards low average isoelectric points. Proteins with a significant insoluble subpopulation making up at least 50% of their soluble one, however, showed a bimodal distribution in terms of average isoelectric points, but were characterized by a shift to a greater fraction of disordered sequences compared to primarily soluble proteins. Lastly, proteins which were solubilized by ATP featured a shift towards both, high average isoelectric points and high fraction of disordered sequences. This analysis further emphasized that the proteins we measured as insoluble and those that we found to be solubilized by ATP were enriched for proteins with characteristics of phase separating proteins forming membrane-less organelles.

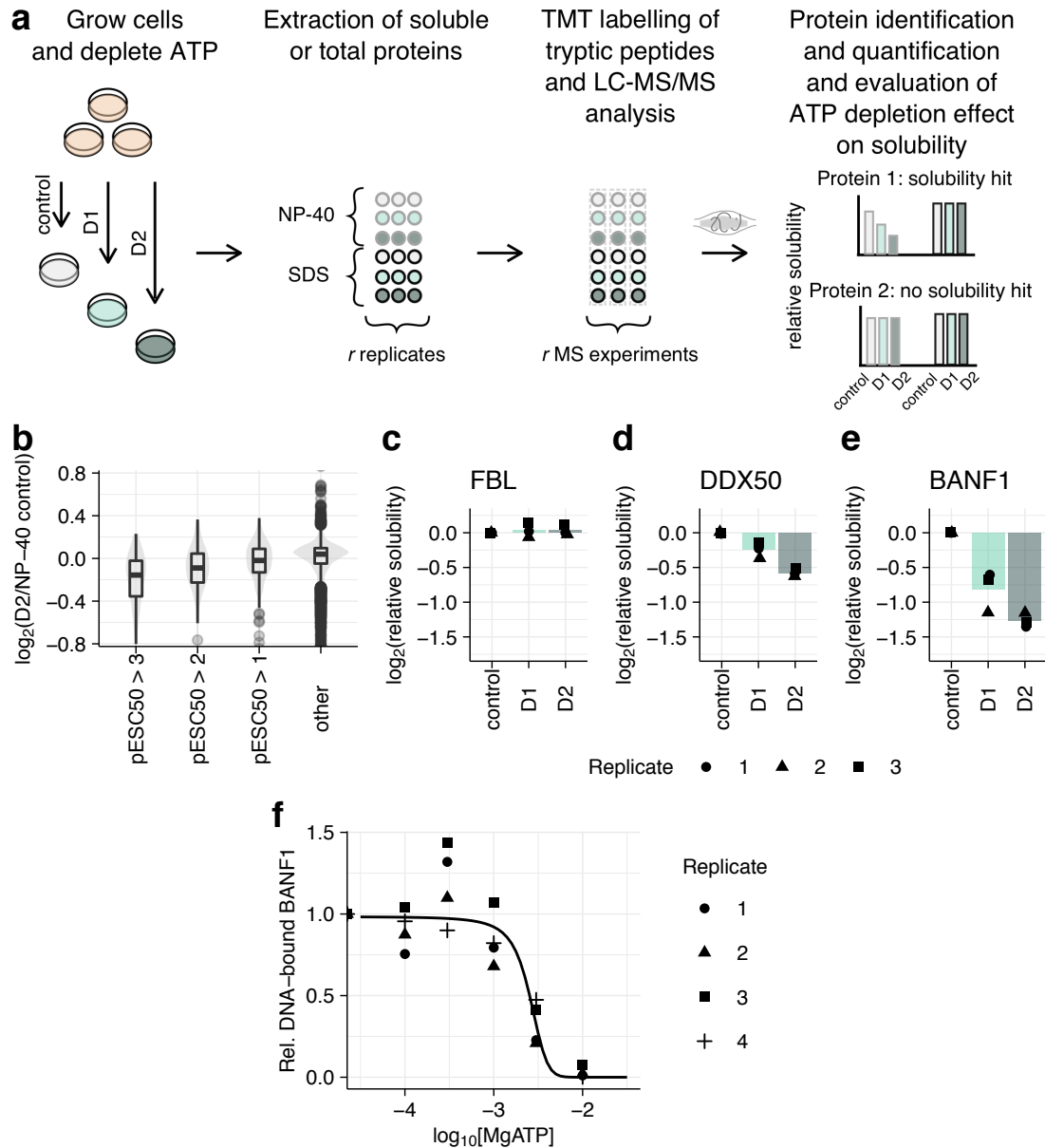


Figure 5.7: SPP experiments in intact cells with depleted ATP levels. a) Schematic of SPP with ATP depleted cells. D1: 0.1 nM AA and 1 mM 2DG, D2: 1 nM AA and 10 mM 2DG. b) Violin plots of degree of insolubility upon ATP depletion for groups of proteins with different pESC₅₀ values measured in the ATP SPP experiment in crude lysate. c-e) Example proteins representing different insolubility patterns upon ATP depletion. f) Relative DNA-bound BANF1 intensity in the presence of different ATP concentrations.

Recently, there has been a report linking ATP hydrolysis to solubilization of *Xenopus* oocyte nucleoli (Hayes et al., 2018). To evaluate whether the ATP induced solubility effects we observed were driven by ATP hydrolysis, we performed SPP experiments with GTP and adenylyl-imidodiphosphate (AMP-PNP) a non-hydrolysable analog of ATP (Figure S5c), using the same concentrations previously used for ATP. When comparing the relative fold changes of all proteins and dose-response solubilization of representative proteins found to be affected by our previous experiment with ATP, we observed that those effects were comparable to the ones observed for ATP (Figure S6). Thus, these control experiments suggested that these effects are not primarily driven by ATP hydrolysis.

Moreover, to verify that our observations would maintain relevance in intact cells and did not resemble artifacts obtained in lysates, we performed an additional experiment in which we reduced intracellular ATP levels and performed SPP of intact cells (Figure 5.7a). This was done using two different doses (D1 and D2, Figure S7) of treatments which inhibited both, oxidative phosphorylation via antimycin A (AA) and glycolysis via 2-deoxyglucose (2DG) (Hertel et al., 1986). Depletion of intracellular ATP levels has many consequences for cellular physiology and thus such experiments have to be interpreted very carefully. Thus, we focused our analysis on the proteins for which we had observed a significant solubility effect in our previous SPP experiment in crude lysates. When considering specifically these proteins, we observed the reversed effect in the ATP depletion experiment (Figure 5.7b), i.e., proteins which were solubilized by ATP in crude lysate already at low nucleotide concentrations, showed the most severe increase in insoluble subpopulations and vice versa. This notion became reinforced when inspecting the obtained patterns for the three exemplary proteins mentioned earlier (Figure 5.7c-e). We were particularly intrigued by the strong changes observed for BANF1, i.e., strong solubilization at low ATP concentrations in crude lysate and high degree of insolubility upon ATP depletion. BANF1 has been reported to cross-bridge chromosomes in anaphase by binding to unspecific DNA sequences (Samwer et al., 2017). Based on our observations we hypothesized that its DNA binding capacity might be affected by ATP binding. Hence,

we recombinantly expressed and purified BANF1 and incubated it with a biotinylated DNA oligonucleotide. When pulling down the DNA fragment with streptavidin beads in the presence of different concentrations of ATP and measuring BANF1 abundance by LC-MS/MS after washing the beads, we observed ATP dose-dependent competition of BANF1 off the DNA (Figure 5.7f). Hence, we conclude that BANF1 binding to DNA is mediated by ATP levels in the nucleus. If ATP levels are high, BANF1 DNA binding is inhibited. When ATP levels drop, BANF1 binds to chromatin and reads out as insoluble in our SPP experiments.

5.4 ATP induced loss of solubility of a small group of proteins

In contrast to the observations of ATP solubilized proteins described above, five proteins lost solubility with increasing concentration of ATP. Prominent examples were IMPDH1 and NUCKS1 (Figure 5.8a and b). IMPDHs have been reported to be modulated allosterically by ATP and to form a filamentous structure upon ATP binding (Labesse et al., 2013). This could explain the observed profile of IMPDH1 in our SPP experiment, due to the possible insoluble nature of their filamentous structures. In both cases it was likely that ATP hydrolysis played a role, since neither of the proteins showed the same behavior in the the SPP experiment with AMP-PNP. These observations made us wonder how such proteins would behave in a TPP-TR experiment with 10 mM ATP, since the treatment should render a high proportion of both proteins insoluble, thus essentially probing thermal stability of different subpopulations of such proteins. Indeed, when considering the melting curves obtained from such a TPP-TR experiment, we observed non-sigmoidal melting curves for both, IMPDH1 and NUCKS1 in the ATP-treated condition (Figure 5.8c and d). We thus normalized the soluble subpopulation by the relative solubility we had measured for both protein in the presence of 10 mM ATP in our SPP experiment.

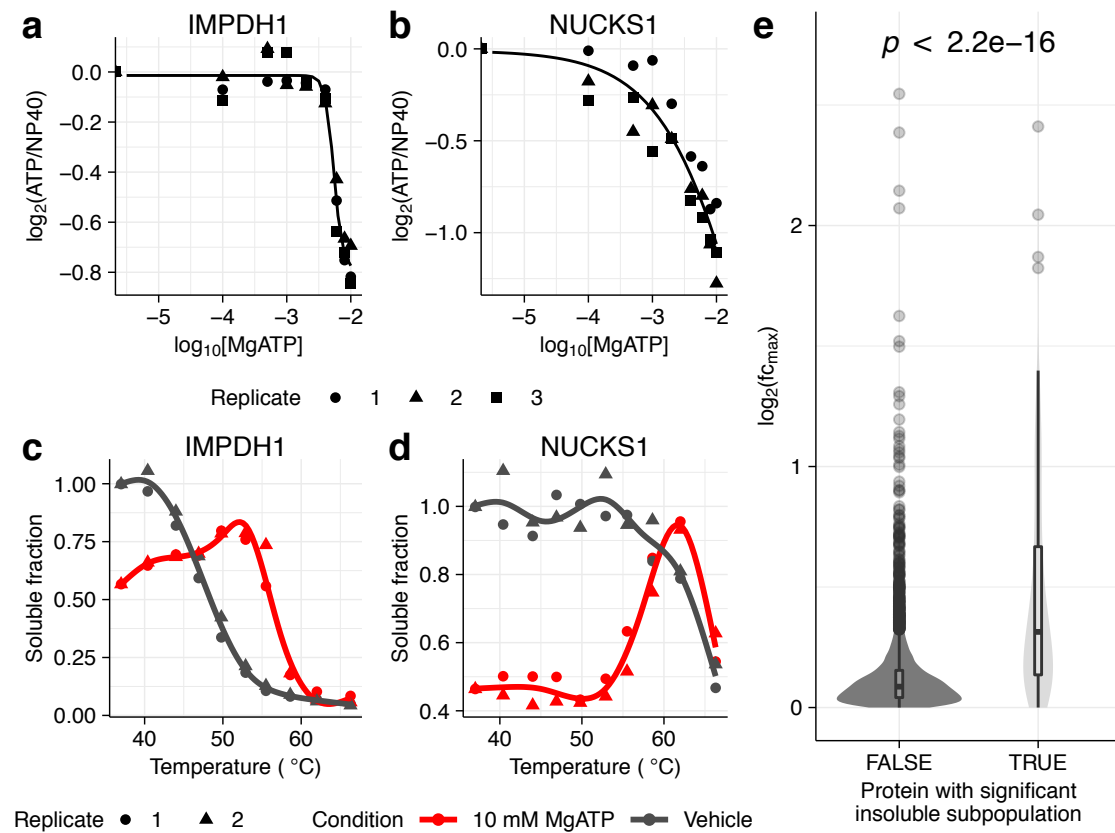


Figure 5.8: Proteins which lose solubility in the presence of high ATP concentrations. SPP profiles in crude lysate treated with ATP of a) IMPDH1 and b) NUCKS1. Melting curves obtained from TPP-TR experiments in crude lysate with and without 10 mM ATP for c) IMPDH1 and d) NUCKS1. The soluble fraction in the ATP-treated condition was corrected by the measured value in the SPP experiment. Both conditions were fit with natural splines with 5 degrees of freedom. e) Violin plot of maximal fold changes measured in control condition melting profiles obtained from crude lysates for proteins which were found by SPP to have insoluble subpopulations vs. such that had no insoluble subpopulations. Significance assessed by Wilcoxon rank sum test.

In the control condition IMPDH1 showed a sigmoidal curve, and the one of NUCKS1 was approximately monotonous, even though it showed incomplete denaturation across the applied temperature range. Hence, we reasoned that the signal we were observing in the ATP-treated condition reflected the reduced soluble subpopulation at the lower temperatures, but with increasing temperatures shifted towards a mixed signal of both subpopulations, apparently due to heat induced solubilization of the insoluble subpool. At the highest temperatures measured, both conditions converged for both proteins indicating that at these condition for both proteins the different subpopulations were behaving homogeneously. This observation made us wonder whether non-normalized signals in TPP-TR experiments could in general correspond to the presence of insoluble subpopulations of proteins. Thus, we compared maximal observed fold changes for proteins measured in the TPP-TR control condition for which we found significant insoluble subpopulations in our SPP comparison of SDS vs. NP-40. Indeed, we found that proteins with a significant insoluble subpopulation showed higher maximal fold changes in melting curves, indicating that non-sigmoidal melting curves, especially featuring higher signal with increasing temperatures as opposed to monotonously decreasing signal, obtained with TPP-TR experiments inform on the presence of such subpopulations (Figure 5.8e).

5.5 Conclusion

Here, it was demonstrated how TPP, particularly in the 2D-TPP format in combination with DLPTP analysis, can be used to study metabolite-protein interactions. Based on the example using the nucleotides ATP and GTP, it was shown that this approach offers the possibility to detect proteome-wide nucleotide interactions and indirect effects such as costabilization of complex members, and solubilization of insoluble protein subpopulations.

Moreover, a dedicated experimental strategy—Solubility proteome profiling (SPP)—to identify proteome-wide insoluble subpools in crude lysates and to profile ATP effects

on the solubility of such proteins was presented. Based on the obtained data it could be shown that many of the proteins found to have insoluble subpopulations and those which were affected in their solubility by ATP were part of membrane-less organelles. We found that proteins of different phase separated compartments showed different susceptibility to ATP solubilization and that high fraction of disordered sequence and increased isoelectric points were associated with this behavior.

Chapter 6

Thermal profiling to identify functional post-translational modifications

“The more we know, the more we realize there is to know.”

— Jennifer Doudna

Post-translational modifications (PTMs) are crucial for various cellular processes ranging from signal transduction to marking proteins for degradation (Karve & Cheema, 2011). Due to constant development and improvement of technologies to detect PTMs, our catalogs of their occurrence are growing continuously (Larsen et al., 2006). However, while specific modifications of individual sites have been linked to functions, globally our understanding of their consequences is limited. Thus, novel approaches are urgently needed which allow to find functional PTMs.

By far the most studied PTM is protein phosphorylation. However, while catalogs of phosphosites exist for several organisms (Hornbeck et al., 2019), we still know little about the functionality of most of these sites. One approach, that is presented in this

chapter, is to compare *in situ* thermal profiles of phosphorylated proteoforms with corresponding unmodified proteins. However, the experimental setup and the corresponding data analysis of such experiments have to be chosen carefully to enable valid interpretation of results. Here, the general principal of such approaches is described. A published experiment of this type by Huang et al. (2019) is inspected and problems with both the experimental approach and the data analysis strategy are analyzed. Subsequently, an alternative experimental setup and corresponding data analysis strategy is presented. Lastly, an advanced analysis strategy is described which can specifically account for unconventional thermal profiles of proteins or phosphopeptides.

6.1 Performing TPP of phosphorylated proteins

First introduced by Azimi et al. (2018), the combination of thermal proteome profiling with phosphopeptide enrichment (phospho-TPP) can give insights into melting behavior of phosphorylated proteoforms which can be different to profiles obtained for respective unmodified proteins, thus potentially reflecting different *intracellular states*. Such states may be defined by different engagement with other proteins, co-factors or by intramolecular rearrangements.

Importantly, to perform phospho-TPP, Azimi et al. (2018) enriched phosphopeptides after *in situ* heat treatment of intact cells, lysis and TMT-labeling of samples incubated at different temperatures. Enrichment post labeling is crucial since the procedure is not linearly comparable for samples with different amount of input material. Hence, when samples which received different heat treatments and thus contain vastly different levels of remaining soluble proteins are enriched separately, this may distort underlying denaturation profiles due to different enrichment efficiencies.

However, in the study by Azimi et al. (2018) no global comparison of melting profiles of phosphorylated proteoforms with their corresponding unmodified proteins was performed.

6.2 Hotspot thermal profiling

Huang et al. (2019) used a similar strategy to the one by Azimi et al. (2018) and proposed the global comparison of thermal profiles of phosphorylated versus unmodified proteins, terming their approach Hotspot thermal profiling (HTP). The authors reported 719 of 2,883 total comparisons (25%, $p < 0.05$, student's t-test) to be significantly shifted, although not considering adjustment for multiple testing and thus not controlling the false discovery-rate. Since the reported results would have exciting implications for effects of phosphorylation, e.g., implying widespread functionality of phosphosites, we carefully analyzed the dataset and the reported method details.

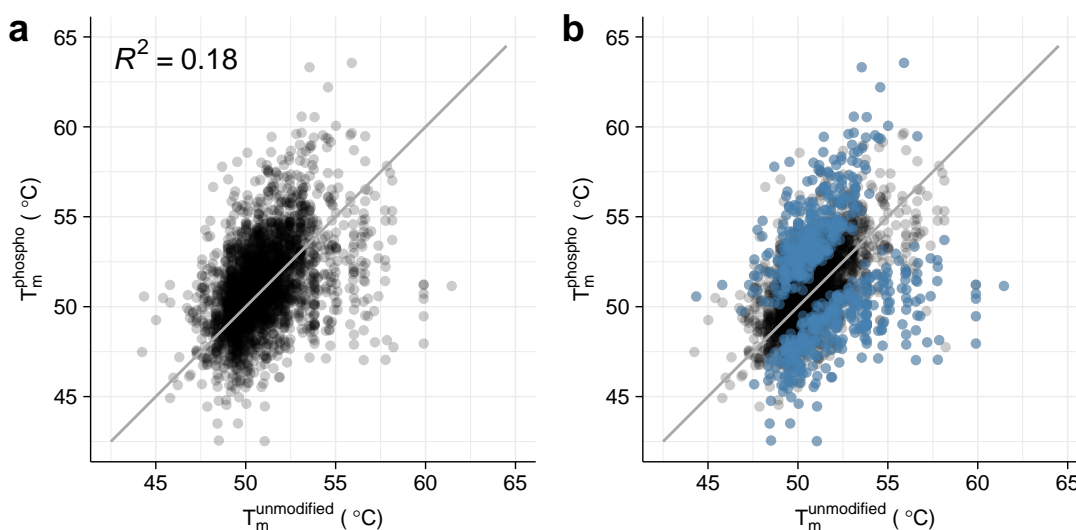


Figure 6.1: Scatterplot of estimated melting points for proteoforms with specific phosphosites and corresponding unmodified proteins from the HTP data. a) Scatterplot of estimated melting points. b) Scatterplot of estimated melting points with indicated significantly thermally shifted proteoforms with specific phosphosites compared to unmodified proteins in blue.

When examining the global relation between melting points of phosphorylated proteoforms and respective unmodified proteins (Figure 6.2a), we observed a surprisingly low correlation ($R^2 = 0.18$).

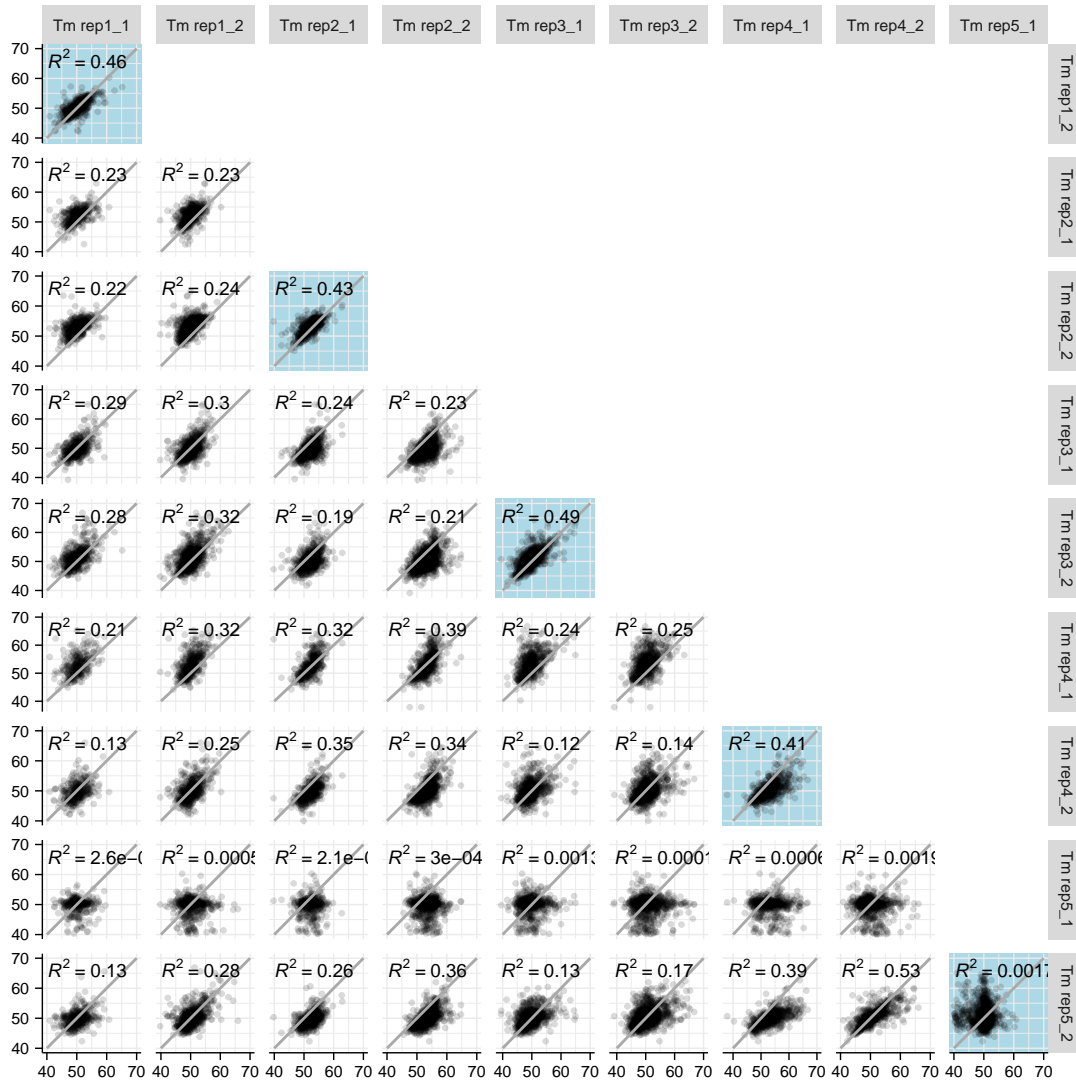


Figure 6.2: Melting point reproducibility for phosphorylated proteoforms from the HTP data. Scatterplots with light blue background represent comparisons of technical replicates.

This is not expected, since the majority of phosphosites is not evolutionary conserved and thus not expected to be functional (Landry et al., 2009) and only a subset of functional phosphosites is expected to alter protein thermal stability profoundly. This observation additionally, indicated to us that the HTP dataset had some inherent problem beyond being analyzed without control for false discoveries. When considering which of the phosphosites Huang et al. had reported to be thermally shifted (Figure 6.2b), it seemed that their method had picked up many comparisons as significant with very low effect size and omitted cases in which compared melting points were relatively high. Both observations further underlined that the applied analysis was not chosen appropriately. To further trace down the origin of the problems observed for the HTP dataset, we inspected reproducibility of the melting point estimates reported for the phosphorylated proteoforms (Figure 6.2). We observed overall low correlation (average $R^2 = 0.22$) between the five replicates with a technical replicate each. However, even between some of the technical replicate samples, correlations were very low. From this, it became evident that there were profound problems associated with the assessment of thermal stability of phosphorylated proteins in the HTP dataset. When carefully inspecting HTP's method details, we noted several points that could have negatively affected quality of thermal profiles of phosphopeptide enriched samples. First, Huang et al. (2019) did not perform orthogonal off-line fractionation to reduce ratio compression. This could have led to unreliable quantification of relative fold changes, which were also not corrected computationally (Savitski et al., 2013). Second, the authors of HTP did not perform phosphopeptide enrichment after, but before labeling with TMT reagents. Due to the above described non-linearity of the enrichment procedure this likely further distorted the relative quantification of phosphoproteoforms at different temperatures. Due to the above raised points, we were convinced that the HTP approach led to low quality melting profiles, especially of phosphopeptide enriched samples. The experimental deficiencies were reinforced by the analysis strategy based on hypothesis tests without consideration of type I error inflation due to no correction for multiple testing.

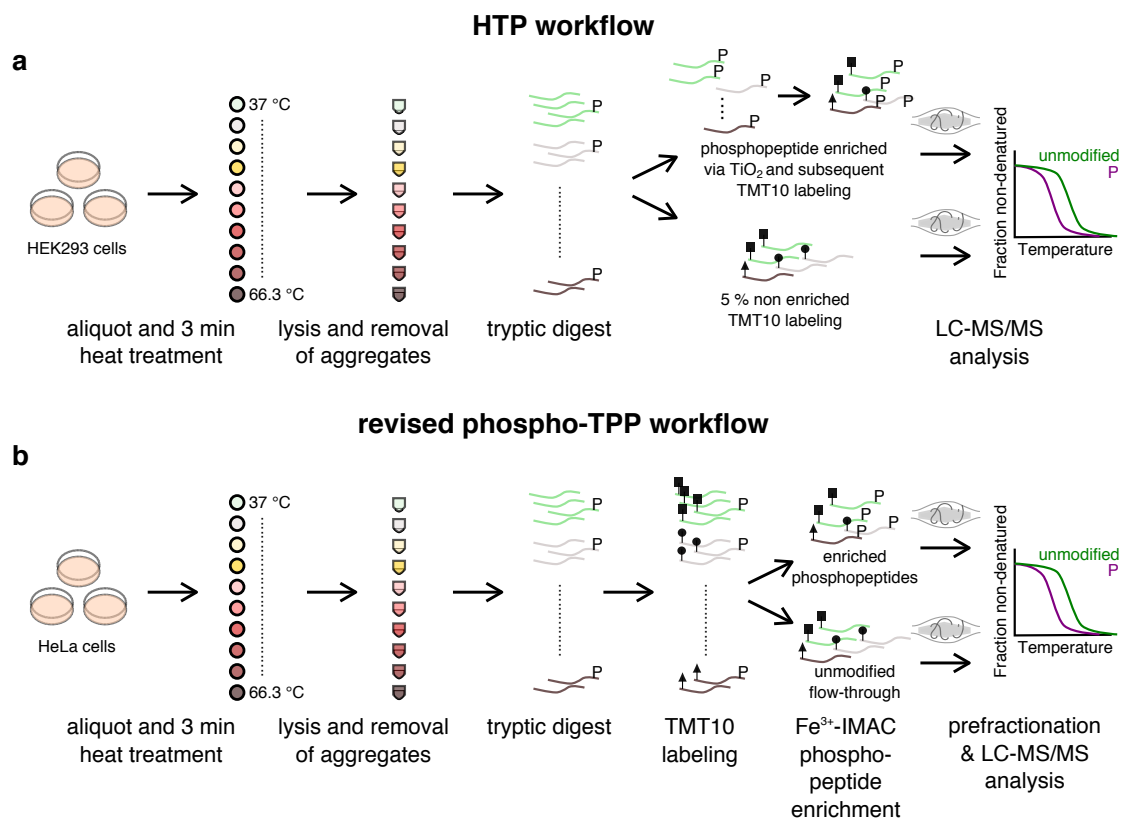


Figure 6.3: Schematic of the HTP and our revised phospho-TPP workflow. a) HEK293 cells are grown, aliquoted and subjected to heat treatment at different temperatures. Cells are lysed and non-denatured proteins extracted and digested with trypsin. 5 % of each aliquot are TMT-labeled and measured via LC-MS/MS analysis and taken as the unmodified control samples. The rest of the differently heat treated samples are enriched for phosphopeptides using TiO₂ spin tips, labeled with TMT and measured via LC-MS/MS analysis. b) Same steps as for HTP with HeLa cells up to the tryptic digest. Then, retrieved peptides of differentially heat-treated samples are labeled with distinct TMT reagents. Phosphopeptide enrichment is performed with pooled samples. Flow-through samples are prefractionated and measured with LC-MS/MS analysis and taken as unmodified samples. Phosphopeptide enriched samples are also prefractionated and measured with LC-MS/MS analysis and taken as the phosphorylated proteoform samples.

Thus, we concluded that the results presented by Huang et al. (2019) could be misleading for individual phosphosites. However, since the general concept of phospho-TPP is promising, we decided to generate a dataset avoiding the outlined pitfalls in experimental design and data analysis.

6.3 A revised workflow for phospho-TPP

The experimental workflow we set out to perform comprised several revised steps as compared to HTP (Figure 6.3). Importantly, these included phosphopeptide enrichment after TMT-labeling of tryptic peptides to avoid distortion of melting profiles by enrichment biases and prefractionation of samples before LC-MS/MS analysis to minimize ratio compression. Further, we developed a dedicated normalization and hypothesis testing strategy for FDR-controlled data analysis.

After database search and quantification, we filtered obtained data to remove peptides affected by ratio compression and required phosphopeptides to feature at least one class I site, i.e., localized with high confidence ($P > 0.75$). Based on the filtered raw data, we realized that we needed to normalize the signal obtained from different TMT reporter ion channels for both the unmodified (non-bound fraction) and the phosphopeptide enriched samples. This is a common necessity in chemical labeling-based MS datasets, induced by sample handling, pipetting errors and heterogeneous labeling efficiencies (Oberg & Mahoney, 2012). However, since we recorded melting curves across the different TMT channels (with decreasing average signal with increasing temperature), we could not simply normalize all channels to the same average signal, but had to employ a different strategy similar to the one suggested by Savitski et al. (2014). Additionally, we wanted to normalize also for effects introduced through differential sample handling of phosphopeptide enriched versus unbound fraction samples. Thus, we developed a two-step normalization procedure. The first step was to align median fold changes obtained for jointly identified unmodified peptides within replicates of phosphoenriched and flow-through samples.

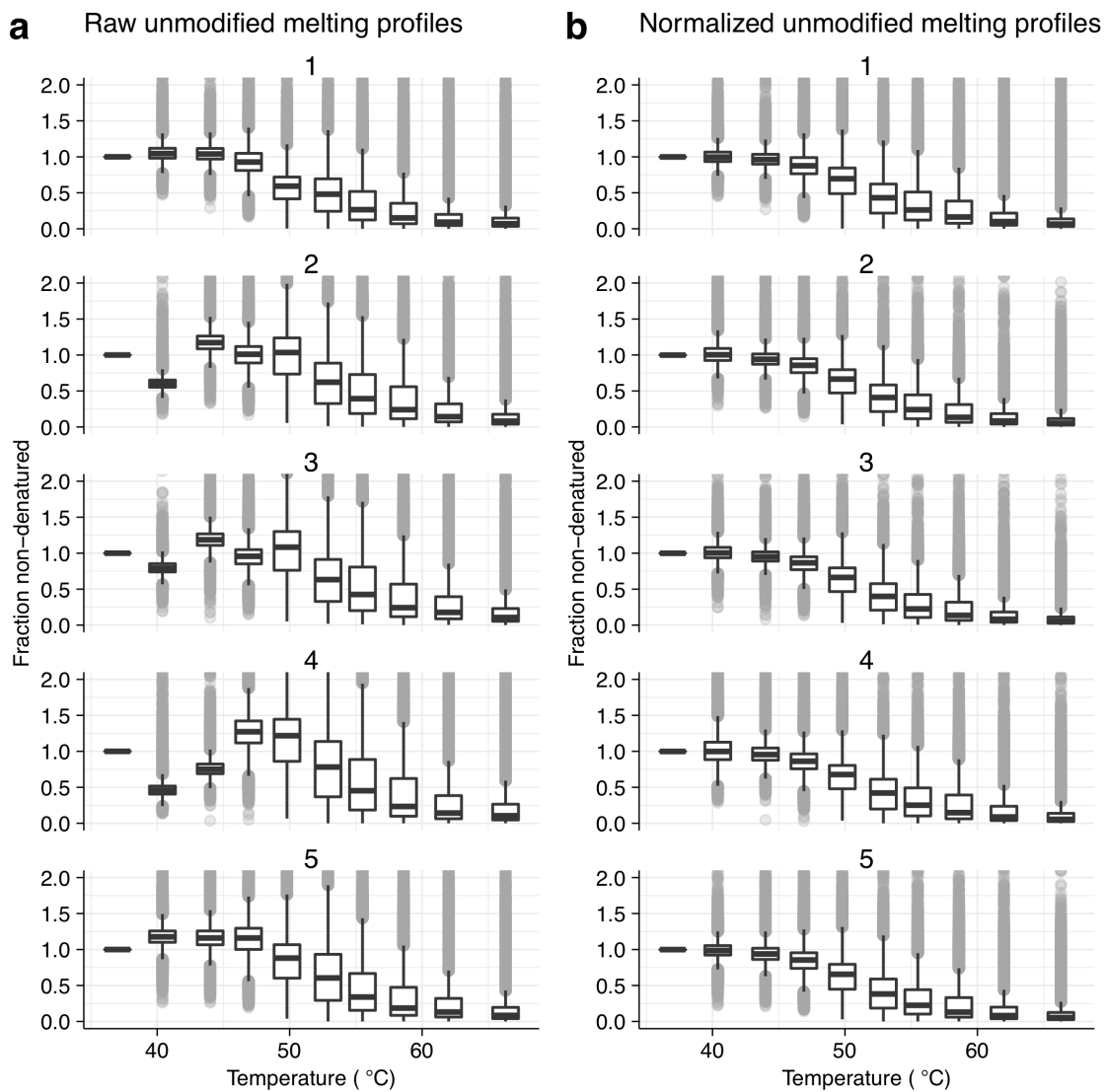


Figure 6.4: Comparison of raw and normalized unmodified protein melting profiles. a) Distributions of raw fold changes obtained at the different temperatures. b) Distributions of normalized fold changes obtained at the different temperatures.

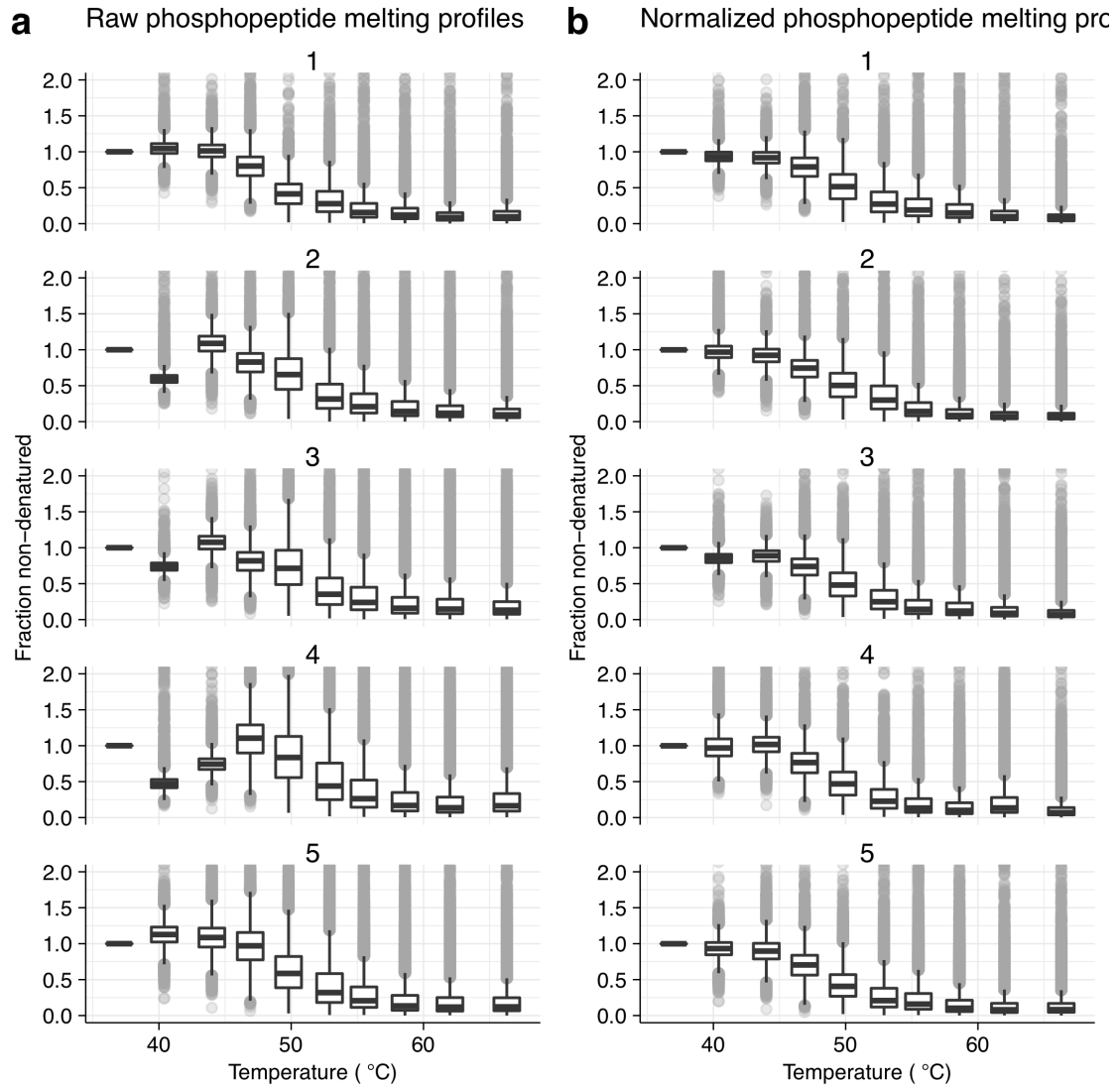


Figure 6.5: Comparison of raw and normalized phosphopeptide melting profiles. a) Distributions of raw fold changes obtained at the different temperatures. b) Distributions of normalized fold changes obtained at the different temperatures.

Second, we adapted the previously described TPP melting curve normalization approach (Franken et al., 2015; Savitski et al., 2014). We applied it to derive temperature-wise normalization factors for all replicates of unmodified datasets and applied them to both the unmodified and the phosphopeptide enriched datasets. The results of this normalization are shown in Figure 6.4 for the unmodified and in Figure 6.5 for the phosphopeptide enriched replicate datasets.

Next, we fit sigmoidal melting curves to the normalized fold changes of each distinct phosphopeptide and across all unmodified peptides mapping uniquely to a protein for each replicate separately. We accepted these fits if they featured an $R^2 > 0.8$ and a plateau lower than 0.2. From all accepted fits we extracted melting point estimates for each replicate for both phosphopeptide and unmodified protein profiles. To evaluate the reproducibility of replicates in our dataset we compared melting point estimates for both unmodified (Figure S8) and phosphorylated proteins (Figure S9). We observed significantly higher correlations between melting point estimates for biological replicates of both conditions than for the HTP data (on average for unmodified proteins: $R^2 = 0.86$, on average for phosphorylated proteins: $R^2 = 0.78$). Thus, we conclude that our revised phospho-TPP workflow led to significantly increased reproducibility compared to the HTP approach.

Next, we globally correlated these melting point estimates obtained for phosphorylated proteoforms and respective unmodified proteins (Figure 6.6a). Globally, we observed a good correspondence between melting points estimated for both conditions ($R^2 = 0.65$). This observation reinforced our initial notion that most phosphosites should not drastically affect protein thermal stability and the fact that this nevertheless appeared to be case for the HTP data was likely technically, but not biologically driven.

Based on our melting point estimates for phosphopeptides and corresponding unmodified proteins we went on to test for shifts in thermal stability. Reasoning that a significant shift of the thermal profile obtained for a phosphopeptide, with confident localization of a single or multiple phosphosites on a protein, compared to its respective unmodified protein indicated a functionality of these sites.

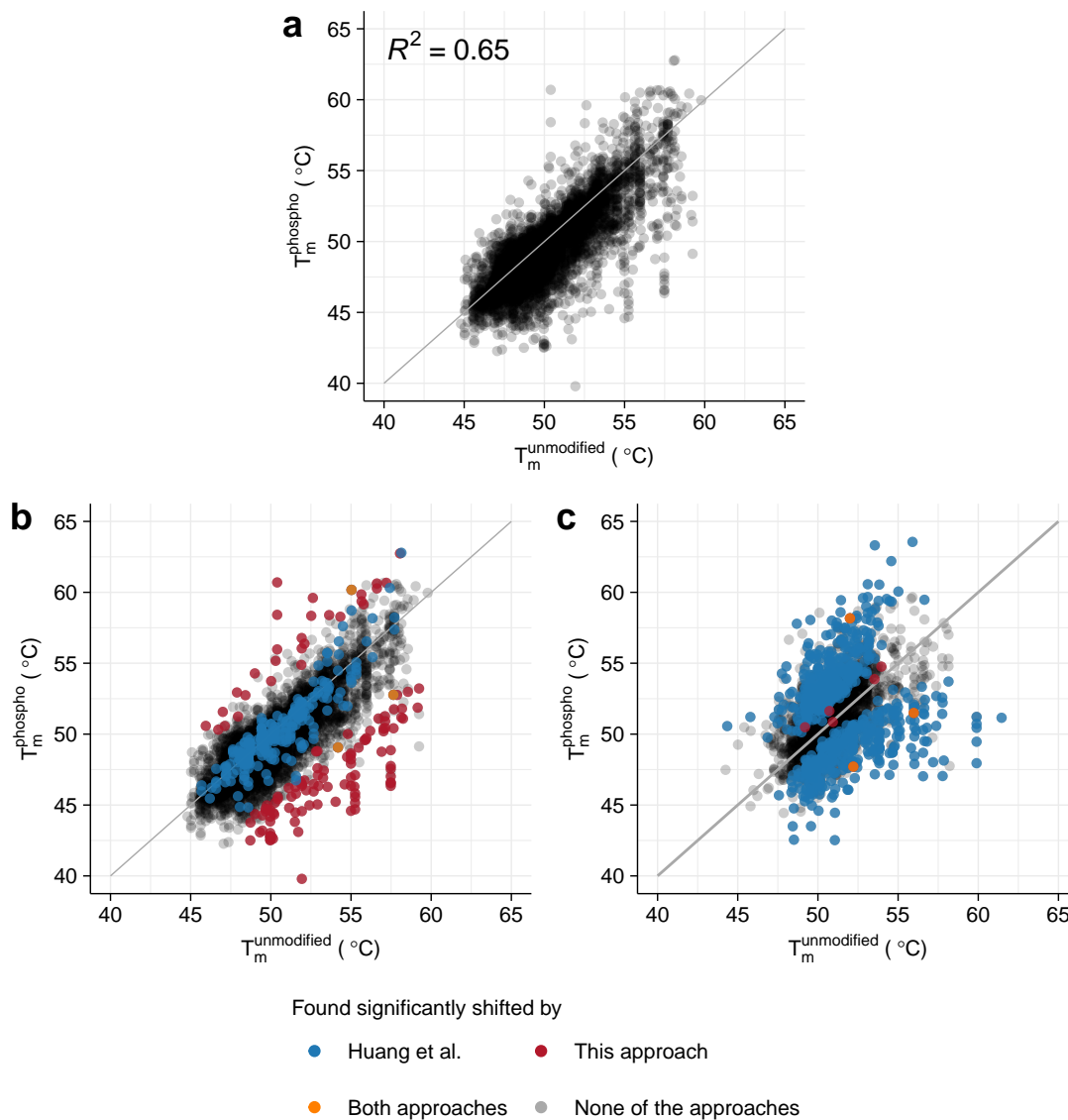


Figure 6.6: Correlation of obtained melting points for phosphorylated and unmodified proteins by the revised approach. a) Scatter plot of melting points obtained from our revised phospho-TPP workflow. Scatterplots of melting points with phosphosited colored by significance in the different datasets, obtained from b) our revised phospho-TPP workflow and c) the HTP workflow.

Hence, we applied the approach originally suggested by Savitski et al. (2014) to compare melting curves obtained from TPP-TR experiments featuring drug treated versus control cells. This approach stringently adjusted for multiple testing in strong contrast to the unadjusted t-tests applied by Huang et al. (2019). Overall, we found about 1.6% of phosphosites to significantly shift thermal stability of corresponding proteins ($p_{\text{adj.}} < 0.01$, 129 out of 7,864 tested comparisons). When comparing the phosphosites found significant by HTP and our approach (Figure 6.6b and c), we evaluated which of the overlapping phosphosites, covered by both methods, were found to have a significant effect on protein thermal stability according to either of the analysis approaches. Based on this, we observed that the vast majority of site-specific phosphorylated proteoforms which Huang et al. (2019) had found to be significantly thermally shifted were not found as such by our approach (234 sites, 98.7%) and were indeed largely scattered around the identity line in Figure 6.6b. On the other hand three out of 8 sites found significantly shifted by our approach were also found significant by HTP (Figure 6.6c). These observations, further substantiated that the results reported by Huang et al. (2019) were misleading. Next, we made use of the functional score for phosphorylation sites, recently reported by Ochoa et al. (2020). This score was obtained by a machine learning approach which integrated several features of phosphosites, such as whether they appear in the interface of known PPIs or whether they are known to be disease associated. We reasoned that phosphosites of thermally shifted proteoforms should be characterized by a higher functional score compared to non-shifted ones. However, when we compared the two groups as identified by HTP, we found no difference between their functional score distributions (Figure 6.7a). On the other hand, for the sites found to be significantly shifted by our revised approach, we indeed saw significantly higher functional scores (Figure 6.7b).

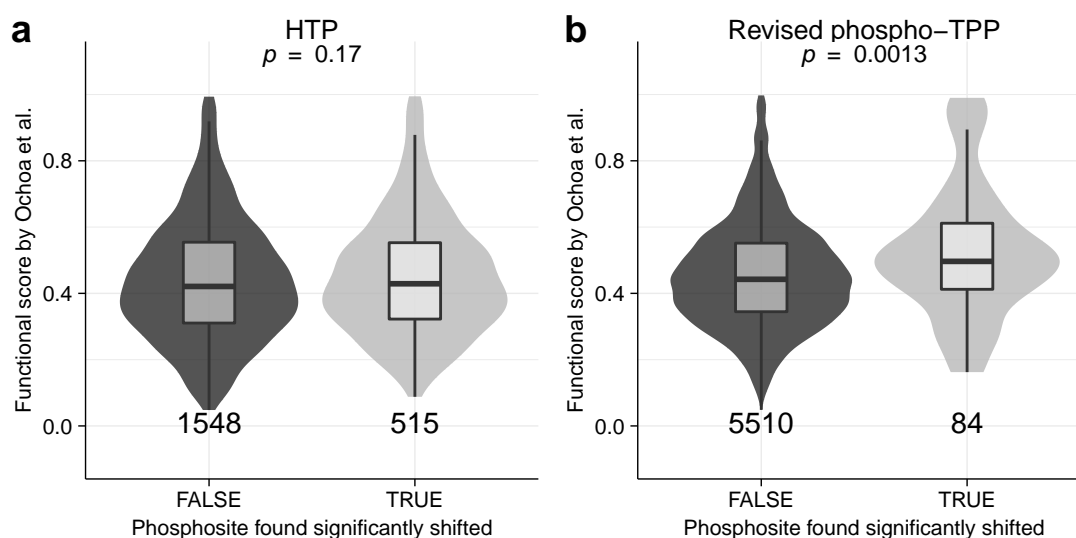


Figure 6.7: Comparison of distribution of functional scores by Ochoa et al. (2020) between shifted vs. non-shifted phosphosites. Violin plots of functional scores for both groups of phosphosites as distinguished by a) HTP and b) our revised phospho-TPP method. Significance between functional score distributions was assessed using a Wilcoxon rank sum test.

Convinced that site-specific phosphorylations on proteins which our approach identified as thermally shifted were strongly enriched for functionally relevant modifications, we went on to explore individual examples of such sites. First of all, we noted that 78% (100 out of 129) of all sites found by our approach to shift thermal stability significantly, had a destabilizing effect on the respective proteins. This was interesting, since we had not expected a general tendency for either stabilization nor destabilization.

One of these destabilizing phosphosite examples was phosphorylation of Tyr³⁹⁷ on protein kinase Lyn (LYN, $\Delta T_m = -5.2^\circ\text{C}$, Figure 6.8a), a protein involved in regulation of immune response, DNA damage response and hematopoiesis (Ingley, 2012). Tyr³⁹⁷ lies in the activation loop of LYN and phosphorylation of this site is known to influence the kinase activity through induction of a conformational change in proteins of the Src subfamily which enables more efficient access to the ATP binding site (Xu et al., 1999). Another example were the joint phosphorylations of Thr¹⁹ and Ser²² (only captured as a

doubly phosphorylated peptide) of Lamin-A (LMNA, $\Delta T_m = -8.6^\circ\text{C}$, Figure 6.8b). The nuclear intermediate filament Lamin-A is involved in the regulation of various essential cellular processes such as chromatin organization and replication (Gruenbaum & Foisner, 2015). Both of the phosphosites detected to affect LMNA thermal stability *in situ* were previously found to be crucial for nuclear lamina disassembly during mitosis (Heald & McKeon, 1990).

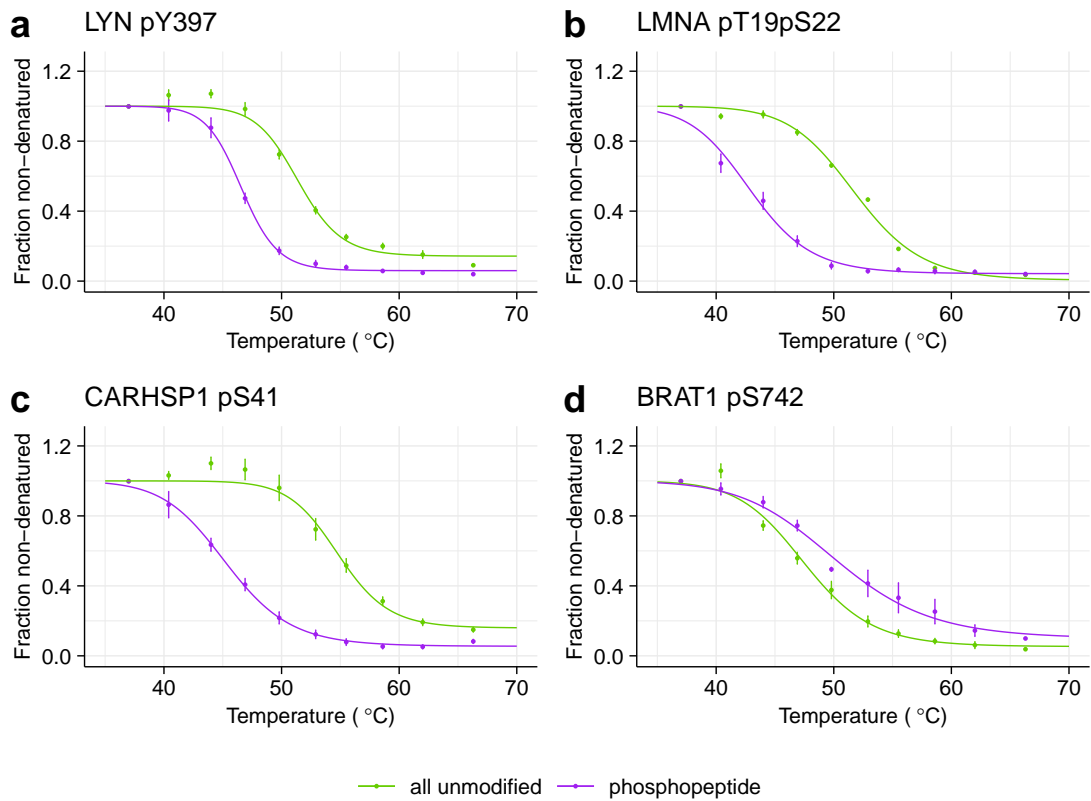


Figure 6.8: Examples of phosphosites found to significantly shift thermal stability of proteins. Comparison of phosphorylated vs. unmodified melting profiles for a) Tyrosine-protein kinase Lyn with and without phosphorylation of Tyr³⁹⁷, b) Lamin-A with and without phosphorylation of Thr¹⁹ and Ser²², c) Calcium-regulated heat stable protein 1 with and without phosphorylation of Ser⁴¹ and d) BRCA1-associated ATM activator 1 with and without phosphorylation of Ser⁷⁴². Error bars represent standard error of the mean.

Third, the cold shock domain containing calcium-regulated heat stable protein 1 (CARHSP1) which is known to localize to P-bodies and to bind tumor necrosis factor- α mRNA and thus to stabilize its half life (Pfeiffer et al., 2011) also was found to feature a phosphosite which thermally destabilized the protein, namely Ser⁴¹ ($\Delta T_m = -9.4^\circ\text{C}$, Figure 6.8c). This is in line with a report linking a Ser⁴¹ phospho-deficient mutant of CARHSP1 to decreased nucleic acid binding and loss of localization to cytoplasmic condensates (Hou et al., 2011). In addition, we found that Ser⁷⁴² phosphorylation of the BRCA1-associated ATM activator 1 (BRAT1, $\Delta T_m = 4.0^\circ\text{C}$, Figure 6.8d), involved in DNA damage response (Aglipay et al., 2006), led to thermal stabilization of the protein. BRAT1 mutations are associated with several diseases such as the rigidity and multifocal seizure syndrome (Srivastava et al., 2016). While Ser⁷⁴² phosphorylation of BRAT1 has been reported by several studies (Hornbeck et al., 2019), no functional role of this phosphosite has so far been implied. It would be interesting to perform pulldown or microscopy experiments with Ser⁷⁴² phosphomimetic and phosphodeficient versions of BRAT1 to see whether this phosphosite is involved in regulating PPIs or intracellular localization.

6.4 A nonparametric approach for phospho-TPP analysis

Our revised approach was able to identify 7,864 high quality comparisons between phosphorylated proteoforms and corresponding unmodified proteins. However, we noted that for some proteins and phosphopeptides the sigmoid fit had not converged or the filtering step on R^2 and plateau of obtained fits eliminated many cases from downstream analysis. Thus, we revisited thermal stability profiles obtained for examples which had been filtered out. Nucleophosmin (NPM1) (highest $R^2 = 0.74$ across replicates) could either not be fitted or was filtered out due to a mild upwards trend at low temperatures ($44\text{-}50^\circ\text{C}$, Figure 6.9a). NPM1 is an abundant component of the nucleolus (Mitrea et al., 2018) and this observation reminded us of our finding in the ATP study (Figure 5.8e), which revealed that proteins with insoluble subpopulations often showed fold changes higher than one, likely representing the thermal aggregation profile of a mixture of subpools.

Another example with an even more extreme profile was observed for the heterogeneous nuclear ribonucleoprotein A0 (HNRNPA0) phosphorylated on Ser⁸⁴, which featured up to four fold higher values at 44°C compared to 37°C (Figure 6.9b), also reminiscent of a profile obtained for a mixture of subpopulations. HNRNPA0 Ser⁸⁴ phosphorylation has been reported to lead to increased binding of HNRNPA0 to GADD45A mRNA, which is thereby stabilized (Reinhardt et al., 2010). This offers a compelling explanation for why a potentially RNA-bound subpopulation of HNRNPA0 may be characterized by Ser⁸⁴ phosphorylation.

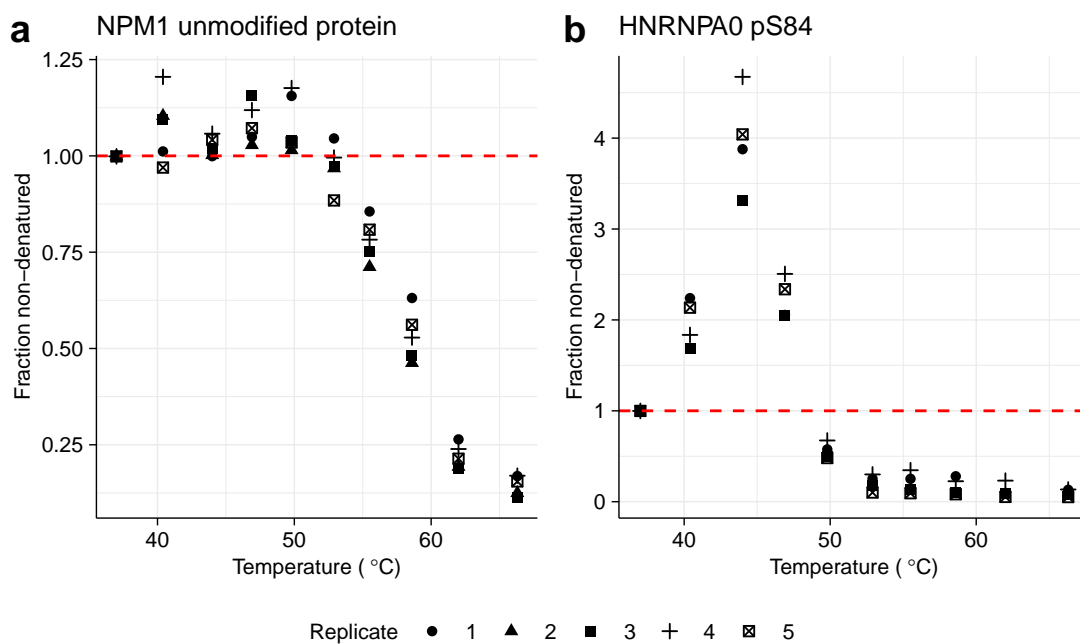


Figure 6.9: Examples of non-sigmoidal thermal profiles. TPP-TR profile of a) Nucleophosmin and b) Ser⁸⁴ phosphorylated heterogeneous nuclear ribonucleoprotein A0.

Motivated to find an approach which would allow us to include such cases into hypothesis testing, we turned to a method suggested by Childs et al. (2019) termed NPARC (Nonparametric analysis of response curves). However, Childs et al. (2019) originally also used sigmoid curves with this procedure, which we thought would not be adequate to capture cases such as the profile of phosphorylated HNRNPA0. Thus, we devised a

strategy of fitting Gaussian processes to phosphopeptide and corresponding unmodified protein thermal profiles and using obtained mean estimates to apply NPARC (NPARC-GP). To apply NPARC's empirical correction of obtained F -statistics, we performed the same procedure with a dataset in which we selected a random unmodified peptide and compared it to all other unmodified peptides. This comparison yielded a distribution of F -statistics expected under the null hypothesis, which we could use to obtain scaling factors to calibrate our F -statistics obtained from the phosphopeptide versus unmodified protein comparison (p -value histograms before and after F -statistic calibration are shown in Figure S10).

Satisfied with the calibration of our statistic, we went on to inspect phosphosites which were found significantly shifted by NPARC-GP (483 out of 16,051, 3% at $p_{\text{adj.}} < 0.01$, Figure 6.10a). This represented a similar fraction as found significant with our previous analysis strategy, while being considerably lower than the 25% reported by Huang et al. (2019). Moreover, as for the data analysis strategy described above, we also found a strong trend towards destabilization of proteins by phosphorylation (83%, 400 out of 483 significantly shifting phosphosites) for NPARC-GP. External validation of phosphosites predicted by NPARC-GP to be functional using the score by Ochoa et al. (2020), showed a highly significant enrichment of high functional scores (Figure 6.10b). Finally, we found that NPARC-GP detected all literature validated cases described above (LYN pY397, LMNA pT19pS22 and CARHSP1 pS41) and in addition phosphosites which modulated thermal stability of NPM1 (Figure 6.11a) and the striking profile of HNRNPA0 pS84 (Figure 6.11b). We thus conclude that NPARC-GP represents a powerful method for phospho-TTP analysis. It allowed assessing the significance of phosphorylation-induced shifts of protein thermal stability for twice as many amenable comparisons as the melting point-centered approach.

Together with results we previously obtained in our work concerning proteins with insoluble subpopulation (Figure 5.8e) and previous reports of site-specific phosphorylation events controlling protein localization to membrane-less organelles (Rai et al., 2018), these results may indicate that the identified phosphosites on NPM1 and HNRNPA0

might represent similar regulatory switches. However, to conclude that this is indeed the case, further experiments such as microscopy studies of specific phosphomimetic and phosphodeficient variants of these proteins in the presence of membrane-less organelle markers are needed.

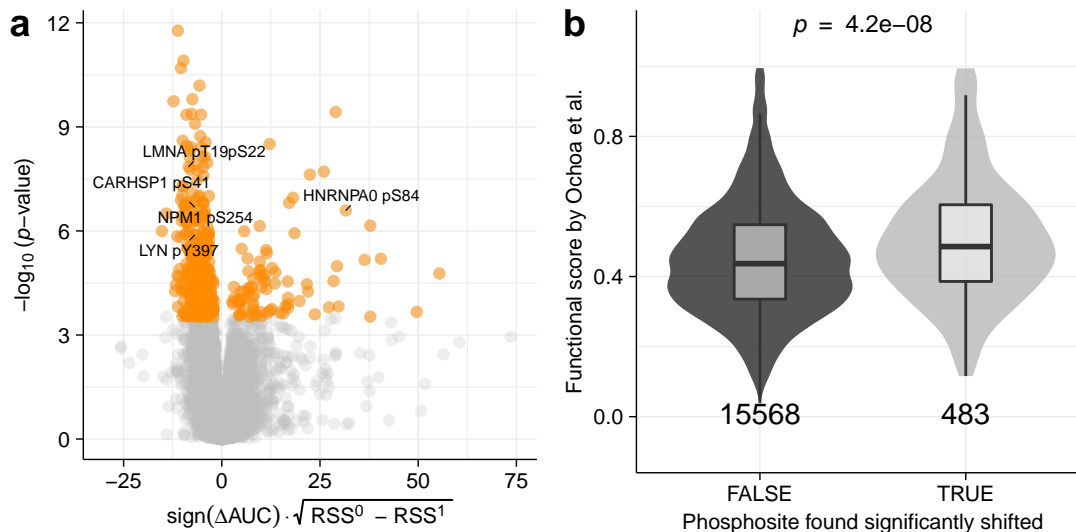


Figure 6.10: NPARC-GP results obtained for the phospho-TPP dataset. a) Volcano plot of NPARC-GP results. The effect size is taken as $\text{sign}(\Delta\text{AUC}) \cdot \sqrt{\text{RSS}^{(0)} - \text{RSS}^{(1)}}$ which describes how much more variance was explained by the alternative versus the null model, signed by the direction of the effect, i.e., stabilization of destabilization as measured by difference in area under the melting curve. Orange dots represent phosphopeptides found to significantly shift thermal stability of proteins at $p_{adj.} < 0.01$. b) Violin plot comparing distributions of functional scores by Ochoa et al. (2020) of significantly shifted vs. non-shifted phosphorylated proteoforms as detected by NPARC-GP. Significance between functional score distributions was assessed using a Wilcoxon rank sum test.

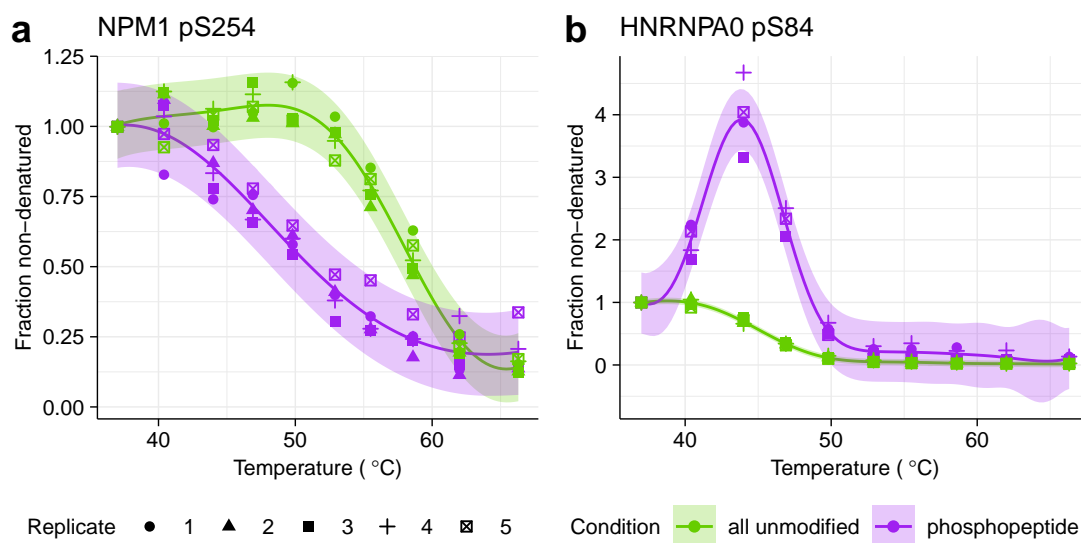


Figure 6.11: Examples of non-sigmoidal melting profiles captured by NPARC-GP. a) Nucleophosmin with and without phosphorylated Ser²⁵⁴ and b) heterogeneous nuclear ribonucleoprotein A0 with and without phosphorylation on Ser⁸⁴.

6.5 Conclusion

In this chapter, the combination of phosphoproteomics with thermal proteome profiling to identify functionally important phosphosites was introduced. A revised experimental strategy for phospho-TPP (Potel et al., 2021) was presented and analyzed in comparison to the HTP data by Huang et al. (2019). It was shown that phospho-TPP together with a dedicated data analysis strategy outperforms HTP in terms of reproducibility and credibility of hits as validated by an external resource (Ochoa et al., 2020). Our approach could recover many phosphosites reported to affect protein states and outlined so far functionally uncharacterized phosphosites which are interesting candidates to study with follow-up experiments.

Moreover, an alternative analysis strategy for phospho-TPP experiments was presented termed NPARC-GP. This approach compares mean estimates obtained by Gaussian process regression for phosphorylated and unmodified corresponding proteins jointly and

per conditions and thus computes an F -statistic. We show that this approach can accommodate thermal profiles which a parametric sigmoid model fails to capture and thus drastically increases amenable comparisons.

Chapter 7

Discussion

“The first rule is that you must not fool yourself and you are the easiest person to fool.”

— Richard Feynman

In this thesis, computational methods for different experimental setups of thermal proteome profiling are presented. The scope of these methods comprises detection of differential protein-protein interactions, identification of small molecule-protein engagement from 2D-TPP data and determination of phosphorylation sites which functionally affect proteins.

In the following, the presented methods and results obtained through their application are discussed in the context of the current literature.

7.1 Tracking protein-protein interactions dynamics with TPP

The first presented method, implemented as R/Bioconductor package `Rtpca`, covers both, the previously described analysis of TPP-TR data to detect significantly coaggregating pairs of proteins or subunits of protein complexes (Tan et al., 2018) and a newly

developed approach for detection of differential coaggregation when comparing two different conditions (Kurzawa, Mateus, et al., 2020).

The advantage of applying TPP to detect PPIs in comparison to other methods such as SEC co-elution MS (Dong et al., 2008; Heusel et al., 2019), BioID (Roux et al., 2012) or bait-prey pull down experiments (Ewing et al., 2007; Gavin et al., 2002), is that it is so far the only method that can give a representation of the *in situ* (Becher et al., 2018; Tan et al., 2018) and more recently also the *in vivo* (Perrin et al., 2020) interaction state of proteins without the requirement for any form of labeling or modification of proteins of interest.

A limitation of using TPP-TR for detection of PPIs or complex subunit assembly is, however, that for the method to work, protein populations have to be fully engaged in the interaction, otherwise the signal will be a mixture of bound and unbound subpopulations and thus not similar enough to that of interacting proteins. This problem is less severe for protein complexes with multiple subunits, since the similarity of melting profiles of multiple proteins is less likely to appear by chance in comparison to that of only two.

Moreover, the implementation of methods available in the `Rtpca` package also offer room for improvement. To integrate data across replicates the method currently computes median profiles. This approach was chosen to simplify the analysis in scenarios where three or more TPP-TR replicates are available, but some proteins were only quantified in two of those replicates. This could be improved by directly using measurements from individual replicates and accounting for the different number of observations when computing pairwise distances by using the normalized Euclidean distances. Additionally, the differential analysis could be generalized to be not only applicable to two, but any number of different conditions.

Further, TPP-TR experiments have so far only been performed with a maximal number of ten TMT channels for a single condition, whereas the latest SEC co-elution methods measure up to 160 fractions (Heusel et al., 2019) and thus can be more sensitive and specific due to more available data points in the profiles of individual proteins. It

would therefore be interesting to see whether a TPP-TR implementation using 16 TMT channels with the recently developed TMTpro reagents (Li et al., 2020) could lead to an improvement in this regard. In particular, it could be interesting to not design the experiment with evenly spaced temperatures, but rather to add more measurements in the low to medium temperature region. Since data quality is usually better in this region due to higher soluble protein abundance and as the most variable regions of protein is expected around the average melting point, such an experimental design could lead to better discrimination between melting profiles of individual proteins. However, since in the TPP-TR format deviations of individual proteins from the average melting profile are inherently limited, i.e., most proteins will follow some form of melting curve, exploiting the increased sensitivity of proteome changes within the same temperature as yielded by the 2D-TPP format (Becher et al., 2016, 2018), could be a more powerful alternative. Recently, we have shown that by measuring proteome-wide effects of genetic perturbation on cells in a 2D-TPP format and searching for proteins co-changing in abundance and thermal stability can lead to an improved prediction of PPIs and protein complexes (A. Mateus, Hevler, et al., 2020). Thus, this indicates that perturbation studies in 2D-TPP format, though being demanding in required sample numbers and MS measurement time, offer a promising route forward (A. Mateus, Kurzawa, et al., 2020).

Finally, a task that has not yet been tackled is using TPP data for the prediction of so far unannotated PPIs or complex members. Such an approach could be particularly powerful if combined with other features such as protein sequences, domains or structural elements (Hu et al., 2021).

In conclusion, it was shown that TPP data can be informative on PPIs and on their dynamics across differential conditions. Through work presented in this thesis, methods to perform such analyses are now available as open source software (<https://bioconductor.org/packages/Rtpca>). Since much of our knowledge on PPIs is based on characterization of easily accessible cell states, e.g., interphase cells in culture, many so far uncharacterized interactions, predominantly established in other cell states, still remain to be discovered. TPP can serve as a useful tool to complement other approaches

in tackling this goal in the future.

7.2 Detection of ligand-protein interactions using TPP

The initial goal which drove the development of TPP was to enable unbiased monitoring of drug-target engagement in living cells (Savitski et al., 2014). Since it first was established, several innovations have advanced its initial protocol (Franken et al., 2015).

One of the first steps was the finding that the original protocol, which used a lysis buffer without any detergents and suffered from not being able to identify membrane proteins, could be modified to include a mild detergent—NP-40, which does not resolubilize heat denatured proteins but makes membrane proteins accessible to the technology (Huber et al., 2015; Reinhard et al., 2015). Recently, this aspect has been further improved by the establishment of a TPP protocol targeting specifically the cell surface proteome (Kalxdorf et al., 2021).

The recent adaptation of the assay to an *in vivo* and *ex vivo* setting represented another milestone, broadening the scope of the method from cell culture-based (off-)target identification to potential application in complementing pre-clinical absorption, distribution and toxicology studies (Perrin et al., 2020).

Importantly, the development of the two-dimensional format (Becher et al., 2016) was another important step forward, since it tackled the problem that different proteins may need different compound doses to stabilize and may denature at different temperatures, thus being susceptible for compound-induced stabilization at varied temperatures. While 2D-TPP improved the sensitivity of the assay, it also led to new data analysis challenges. Since obtained profiles are obtained by several independent MS runs, noise levels can vary across the profiles and due to full denaturation of measured proteins at some of the temperatures used for heat treatment, resulting data tables also feature missing values. Hence, identification of ligand-interacting proteins was done by applying bespoke thresholds to 2D-TPP data (Becher et al., 2016). However, these thresholds do not offer false discovery-rate control and are inherently limited in sensitivity. Thus, to address

the need for a statistical method for 2D-TPP analysis we developed the R/Bioconductor package TPP2D (method name: DLPTP, <https://bioconductor.org/packages/TPP2D>) (Kurzawa, Becher, et al., 2020).

7.2.1 FDR-controlled ligand-protein detection with DLPTP

The concept of DLPTP’s approach is inspired by NPARC (Childs et al., 2019), which features a nested modeling approach combined with ANOVA for detection of ligand-binding proteins from TPP-TR experiments avoiding the use of summary parameters. However, applying a similar concept to datasets obtained by the 2D-TPP format entails several additional challenges. First, nested null and alternative models have to be designed which need to be flexible enough to accommodate typical observed profiles and yet constrained such that effects on protein thermal profiles induced by drug binding can be fit, but not random deviations induced by experimental noise. Eventually this is realized by choosing the null model as a temperature-dependent intercept model (Eq. 2.8) and the alternative model as a temperature-wise dose-response model (Eq. 2.9) with several constraints on its parameters to avoid overfitting of apparent dose-response trends at individual temperatures. Second, obtained F -statistics need to be calibrated in terms of FDR. This is realized by adapting the bootstrapping procedure suggested by Storey et al. (2005) for analysis of microarray timecourse experiments. Third, to prevent misinterpretation of alternative models with extremely low or comparably high (often induced by few outlier measurements) residual error, an empirical Bayes moderation of obtained F -statistics is implemented.

The method implementing the above described features is shown to outperform the be-spoke rules approach on a synthetic dataset (Figure 4.2). However, some drawbacks still exist. First, especially the optimization of the complex alternative model is computationally intensive and together with the bootstrapping approach for FDR-calibration of the F -statistic, the method is slow and on the limit of what can be run on a laptop: 3-5 hours to run the method for a human dataset on one core of a modern laptop, while

applying the bespoke rules can be done in less than an hour. This could be improved by expanding the null and the alternative models such that the correlation of residuals can be accounted for and the ANOVA assumptions approximately hold true, so that the expected distribution of the F -statistic under the null can be used or at least empirically corrected to be used as suggested by Childs et al. (2019).

Moreover, although the method globally performs better than the bespoke thresholds, it misses the identification of individual known true positives, e.g., HDAC6 in the Panobinostat in-cell dataset (Figure 4.3a), for which the respective profile contains outlier measurements that prevent the fit from achieving low residual error (Figure S2). This issue is in part tackled by performing empirical Bayes moderation of the F -statistic, which leads to an overall increase in sensitivity without compromising specificity. However, even with empirical Bayes moderation, the aforementioned profile of HDAC6 can not be recovered at an acceptable FDR. This issue is expected to be alleviated by the improved experimental 2D-TPP designs (Zinn et al., 2021), exploiting additional available isobaric channels through usage of TMTpro (Li et al., 2020) to measure eight instead of five different compounds concentrations at every temperature.

Another remaining challenge in the analysis of 2D-TPP datasets is the interpretation of observed ligand-induced effects on thermal stability, i.e., determining whether an altered thermal profile is indicative of a ligand directly binding to a protein, inducing a change of interactions with other proteins or of a downstream process which leads to cofactor binding or to intramolecular rearrangements. This issue is showcased by the example of DHRS1 in the *ex vivo* Panobinostat datasets (Figures 4.5b-e). With increasing numbers of 2D-TPP datasets that will be generated in the future and orthogonal experiments to interpret observed hits, it may be possible to train machine learning algorithms to classify these different cases and thus to exploit even more of the potential of this technology.

In summary, TPP represents one of the current state-of-the-art technologies for detection of ligand-protein interactions, with advantages over similar methods, such as, no need for chemical modification of the compound of interest and application *in situ* and *in vivo* (A. Mateus, Kurzawa, et al., 2020). The increasing availability of open source computa-

tional methods for statistical analysis of obtained datasets further enables interpretation of retrieved datasets by the broad community (Childs et al., 2019; Kurzawa, Becher, et al., 2020).

7.3 TPP for detection of metabolite-protein interactions

Metabolites are one of the numerically most abundant classes of biomolecules in cells. By serving as cofactors, substrates and allosteric inhibitors, metabolites interacting with proteins are essential for cellular life (Diether & Sauer, 2017). While many metabolite-protein interactions have been studied based on isolated proteins via *in vitro* assays, systematic studies are rare (Yang et al., 2012).

In recent years, studies in *Saccharomyces cerevisiae* (Li et al., 2010) and *Escherichia coli* (Piazza et al., 2018) were performed, showing that many metabolite-protein interactions are not yet characterized. These can have a multitude of functional implications which are important to discover to further our understanding of protein regulation in cells. Thus, it is vital to develop approaches to map metabolite-protein interactions, especially in human cells to better understand cellular metabolism and its cross-regulation with proteins in health and disease.

The first application of TPP-TR to study metabolite-protein interactions was done by Reinhard et al. (2015) and Huber et al. (2015). While these approaches could recover a considerable amount of annotated interactors of the probed metabolites, also many known interactors were not found based on melting curve shifts. Hence, we performed experiments to probe the protein interactions landscape of ATP and GTP using the more sensitive 2D-TPP and analyzed the obtained data with DLPTP. For the 2D-TPP experiment with ATP, we identify over 50% more annotated ATP binders (Figure 5.1c) than with the TPP-TR setup, plus many so far uncharacterized interacting proteins. Performing 2D-TPP experiments for various other metabolites will help to systematically catalog metabolite-protein interactions and thus further our understand of metabolic and protein activity regulation.

Interestingly, we also find evidence that metabolite-protein interactions may affect assembly of protein complexes. Proteome-wide ATP-binding subunits appear to thermally co-stabilize non-ATP-binding subunits in their proximity (Figure 5.2). Indeed, such phenomena have been observed previously, e.g., the interaction of the histone deacetylase HDAC3 and its corresponding deacetylase activation domain of NCOR2 is dependent on inositol (1,4,5,6)-tetrakisphosphate which acts as a ‘intermolecular glue’(Watson et al., 2012). Thus, similar interaction-mediating roles are likely to exist for other metabolites and using TPP to study their effects on proteomes may help elucidate them.

Lastly, we make a striking observation in our 2D-TPP dataset of ATP, namely that in addition to the expected thermal stability effects induced by the nucleotide, at high concentrations it also appears to affect solubility of some proteins in mechanically disrupted cells. These results are in line with a recent report by Patel et al. (2017), who have described solubilizing effects of ATP on purified proteins which form condensates *in vitro*. Thus, we devised dedicated experiments to further characterize these effects.

7.3.1 ATP effects on protein solubility

Our SPP experiments in crude lysates (Figure 5.4) yield two distinct insights. First, the comparison of the SDS versus NP-40 extracted proteome gives insights into which proteins have insoluble subpopulations in the specific system we profile. Second, the comparison of NP-40 with different concentrations of MgATP versus NP-40-only extracted proteome gives insights into which of these insoluble pools can be resolubilized by ATP. Enrichment analyses for both comparisons suggests that these proteins localize to membrane-less organelles. Hence, our observations could substantiate the suggested role of ATP in regulating solubility of protein condensates (Brangwynne et al., 2011), ensuring that they stay liquid-like and do not transition to solid-like phases which have been described to have the potential to form irreversibly aggregated states often linked to pathologies (Molliex et al., 2015).

Patel et al. (2017) have attributed hydrophobic protein condensate solubilizing effects of

ATP to its amphiphilic properties comprising a relatively lipophilic adenosine ring and a highly hydrophilic triphosphate group. They have thus concluded that it acts as a biological *hydrotrope*, which are small compounds that contain hydrophobic and hydrophilic functional groups and can solubilize hydrophobic molecules in aqueous solvents (Kunz et al., 2016). Recently, there has been a discussion on whether this term is adequately describing effects exerted by ATP (Mehringner et al., 2021). The authors show that, contrary to what would be expected of a hydrotrope, ATP does not reduce surface tension (Mehringner et al., 2021). Moreover, some reports have linked ATP to inducing a loss, rather than a gain, in solubility of organic substances (Vraneš et al., 2020). Mehringner et al. (2021) thus argue that the effects observed by Patel et al. (2017) on proteins stem from different features than their hydrophobic nature, e.g., that ATP’s adenosine ring may interfere with π - π stacking of tryptophan-enriched low-complexity domains mediating protein phase separation (Wang et al., 2018). The arguments by Mehringner et al. (2021) are in line with our observations (Figure 5.6e) that ATP predominantly affects solubility of proteins with a high fraction of disordered regions and elevated isoelectric points which thus can not primarily be hydrophobic.

Hence, the emerging picture seems to be that ATP can affect insoluble subpools of proteins with disordered domains and with a tendency to be positively charged. Mechanistically this effect appears to be driven by interference of π - π stacking of interacting low-complexity domains within condensates by its hydrophobic adenosine ring. Negatively charged proteins are less affected due to ionic repulsion of ATP, but its strongly negative triphosphate group may additionally disturb cation- π interactions also involved in formation of phase separated compartments (Wang et al., 2018).

In summary, multiple lines of research have led to observations that high ATP concentrations can have solubilizing effects of condensates formed by certain proteins. Importantly, several of these studies (Mehringner et al., 2021; Patel et al., 2017), including the work presented in this thesis (Sridharan et al., 2019), have performed experiments indicating that the observed effects are independent of ATP hydrolysis. While discussions on the correct term to describe this phenomenon are still ongoing, the evidence for the intracellular

relevance of these observations is growing.

7.4 Detection of functional PTMs

In chapter 6, we have evaluated an approach termed Hotspot thermal profiling (HTP) which has been suggested for the identification of functional phosphorylation sites (Huang et al., 2019), using a modified version of phospho-TPP suggested by Azimi et al. (2018). We found several problems associated with the presented experimental strategy and the data analysis, resulting in misleading results obtained by HTP. Thus, we suggest a revised experimental workflow and a corresponding data analysis strategy. With our improved method, we find that only a small fraction of phosphosites induces shifts in thermal stability of respective proteins ($< 2\%$, Figure 6.6b). However, those sites which we find to alter thermal stability are enriched for known regulatory sites (Figure 6.8) and show an increased probability to be functional as predicted by the machine learning-derived score by Ochoa et al. (2020) (Figure 6.7). Our conclusion, based on the comparison of different phospho-TPP protocols, is that several aspects of the experimental workflow are vital to ensure generation of meaningful datasets and their valid interpretation: i) Phosphopeptide enrichment needs to be performed after TMT-labeling, ii) both, phosphorylated and unmodified, samples need to be prefractionated before LC-MS/MS analysis and iii) obtained data needs to be adequately normalized and analyzed with false discovery rate control (Potel et al., 2021).

Having generated a dataset following the above raised points, in addition to many examples with typical sigmoidal profiles, we find also phosphorylated proteoforms, which feature strikingly non-sigmoidal melting profiles. The most prominent example is represented by Ser⁸⁴ phosphorylated HNRNPA0, a component of ribonucleosomes, which features a strong increase in soluble fraction at temperatures up to 50°C before denaturing at higher temperatures (Figure 6.9b). Two reports have linked its phosphorylation on Ser⁸⁴, placed by MAP kinase-activated protein kinase 2 in response to lipopolysaccharide treatment or DNA damage, to increased mRNA binding (Reinhardt et al., 2010;

Rousseau et al., 2002). Together with our previous observation that melting curves of proteins with insoluble subpopulation can feature such profiles (Figure 5.8e), it is tempting to speculate that mRNA-bound Ser⁸⁴ phosphorylated HNRNPA0 form RNA-dependent insoluble subpools.

Like the example of the phosphoproteoform of HNRNPA0, other sites, which may be involved in the regulation of protein localization to insoluble subpools, could be part of phospho-TPP datasets. However, since such non-sigmoidal melting profiles can often not be incorporated into differential analysis based on sigmoid fits and comparison of melting points, we adapt the previously suggested nonparametric approach (Childs et al., 2019) to work with mean function estimates obtained from Gaussian processes. While the fraction of significantly thermally shifted phosphorylated proteoforms is still small (3%) this method allows to double the amenable phosphorylated versus unmodified profiles which can be compared.

Taken together, we suggest both, an experimental workflow and a corresponding statistical analyses, which offer the exploration of effects of phosphosites on protein states. The presented approach is by no means limited to the study of phosphorylation sites, but can readily be applied to various other PTMs such as acetylation or ubiquitinylation. Moreover, it is also not limited to human as the only amenable organism. Smith et al. (2020) have performed a similar protocol in yeast and in the future it would be interesting to expand this to other organisms and to different human cell types for which TPP is established in (Jarzab et al., 2020).

7.5 Conclusion

In summary, this work suggested computational methods to various application areas of thermal proteome profiling, which advanced its sensitivity and scope. In the future, TPP may contribute to more informed decisions in pre-clinical drug development, characterization of novel PPI dynamics, cataloging of metabolite-protein interactions and the discovery of functional PTMs in diverse organisms.

Bibliography

- Aglipay, J. A., Martin, S. A., Tawara, H., Lee, S. W., & Ouchi, T. (2006). ATM activation by ionizing radiation requires BRCA1-associated BAAT1. *The Journal of Biological Chemistry*, *281*(14), 9710–9718. <https://doi.org/10.1074/jbc.M510332200>
- Alberts, B., Johnson, A., Lewis, J., Raff, M., Roberts, K., & Walter, P. (2007). *Molecular biology of the cell* (5th ed.). Garland Science.
- Andersen, J. S., Matic, I., & Vertegaal, A. C. O. (2009). Identification of SUMO target proteins by quantitative proteomics. *Methods in Molecular Biology*, *497*, 19–31. https://doi.org/10.1007/978-1-59745-566-4/_2
- Azimi, A., Caramuta, S., Seashore-Ludlow, B., Boström, J., Robinson, J. L., Edfors, F., Tuominen, R., Kemper, K., Krijgsman, O., Peeper, D. S., Nielsen, J., Hansson, J., Egyhazi Brage, S., Altun, M., Uhlen, M., & Maddalo, G. (2018). Targeting CDK2 overcomes melanoma resistance against BRAF and hsp90 inhibitors. *Molecular Systems Biology*, *14*(3), e7858. <https://doi.org/10.15252/msb.20177858>
- Balasubramanian, S., Ramos, J., Luo, W., Sirisawad, M., Verner, E., & Buggy, J. J. (2008). A novel histone deacetylase 8 (HDAC8)-specific inhibitor PCI-34051 induces apoptosis in t-cell lymphomas. *Leukemia*, *22*(5), 1026–1034. <https://doi.org/10.1038/leu.2008.9>
- Banani, S. F., Lee, H. O., Hyman, A. A., & Rosen, M. K. (2017). Biomolecular conden-

- sates: Organizers of cellular biochemistry. *Nature Reviews. Molecular Cell Biology*, 18(5), 285–298. <https://doi.org/10.1038/nrm.2017.7>
- Bantscheff, M., Lemeer, S., Savitski, M. M., & Kuster, B. (2012). Quantitative mass spectrometry in proteomics: Critical review update from 2007 to the present. *Analytical and Bioanalytical Chemistry*, 404(4), 939–965. <https://doi.org/10.1007/s00216-012-6203-4>
- Becher, I., Andrés-Pons, A., Romanov, N., Stein, F., Schramm, M., Baudin, F., Helm, D., Kurzawa, N., Mateus, A., Mackmull, M.-T., Typas, A., Müller, C. W., Bork, P., Beck, M., & Savitski, M. M. (2018). Pervasive protein thermal stability variation during the cell cycle. *Cell*, 173(6), 1495–1507.e18. <https://doi.org/10.1016/j.cell.2018.03.053>
- Becher, I., Werner, T., Doce, C., Zaal, E. A., Tögel, I., Khan, C. A., Rueger, A., Muelbaier, M., Salzer, E., Berkers, C. R., Fitzpatrick, P. F., Bantscheff, M., & Savitski, M. M. (2016). Thermal profiling reveals phenylalanine hydroxylase as an off-target of panobinostat. *Nature Chemical Biology*, 12(11), 908–910. <https://doi.org/10.1038/nchembio.2185>
- Benjamini, Y., & Hochberg, Y. (1995). Controlling the false discovery rate: A practical and powerful approach to multiple testing. *Journal of the Royal Statistical Society. Series B (Methodological)*, 57(1), 289–300. <https://www.jstor.org/stable/2346101>
- Bentley, D. R., Balasubramanian, S., Swerdlow, H. P., Smith, G. P., Milton, J., Brown, C. G., Hall, K. P., Evers, D. J., Barnes, C. L., Bignell, H. R., Boutell, J. M., Bryant, J., Carter, R. J., Keira Cheetham, R., Cox, A. J., Ellis, D. J., Flatbush, M. R., Gormley, N. A., Humphray, S. J., ... Smith, A. J. (2008). Accurate whole human genome sequencing using reversible terminator chemistry. *Nature*, 456(7218), 53–59. <https://doi.org/10.1038/nature07517>
- Bishop, C. M. (2006). *Pattern recognition and machine learning*. Springer-Verlag New

York.

- Brandts, J. F. (1964). The thermodynamics of protein denaturation. I. The denaturation of chymotrypsinogen. *Journal of the American Chemical Society*, *86*(20), 4291–4301. <https://doi.org/10.1021/ja01074a013>
- Brangwynne, C. P., Mitchison, T. J., & Hyman, A. A. (2011). Active liquid-like behavior of nucleoli determines their size and shape in xenopus laevis oocytes. *Proceedings of the National Academy of Sciences of the United States of America*, *108*(11), 4334–4339. <https://doi.org/10.1073/pnas.1017150108>
- Byrd, R. H., Lu, P., Nocedal, J., & Zhu, C. (1995). A limited memory algorithm for bound constrained optimization. *SIAM Journal on Scientific Computing*, *16*(5), 1190–1208. <https://doi.org/10.1137/0916069>
- Carlson, M. (2020). *Org.Hs.eg.db: Genome wide annotation for human*.
- Chien, C. T., Bartel, P. L., Sternglanz, R., & Fields, S. (1991). The two-hybrid system: A method to identify and clone genes for proteins that interact with a protein of interest. *Proceedings of the National Academy of Sciences of the United States of America*, *88*(21), 9578–9582. <https://doi.org/10.1073/pnas.88.21.9578>
- Childs, D., Bach, K., Franken, H., Anders, S., Kurzawa, N., Bantscheff, M., Savitski, M., & Huber, W. (2019). Non-parametric analysis of thermal proteome profiles reveals novel drug-binding proteins. *Molecular & Cellular Proteomics*. <https://doi.org/10.1074/mcp.TIR119.001481>
- Cohen, P. (2002). The origins of protein phosphorylation. *Nature Cell Biology*, *4*(5), E127–30. <https://doi.org/10.1038/ncb0502-e127>
- Cokus, S. J., Feng, S., Zhang, X., Chen, Z., Merriman, B., Haudenschild, C. D., Pradhan, S., Nelson, S. F., Pellegrini, M., & Jacobsen, S. E. (2008). Shotgun bisulphite sequencing of the arabidopsis genome reveals DNA methylation patterning. *Nature*, *452*(7184), 215–219. <https://doi.org/10.1038/nature06745>

- Cotter, R. J. (1999). The new time-of-flight mass spectrometry. *Analytical Chemistry*, 71(13), 445A–51A. <https://doi.org/10.1021/ac9904617>
- Cox, J., Hein, M. Y., Lubner, C. A., Paron, I., Nagaraj, N., & Mann, M. (2014). Accurate proteome-wide label-free quantification by delayed normalization and maximal peptide ratio extraction, termed MaxLFQ. *Molecular & Cellular Proteomics*, 13(9), 2513–2526. <https://doi.org/10.1074/mcp.M113.031591>
- Cox, J., & Mann, M. (2008). MaxQuant enables high peptide identification rates, individualized p.p.b.-range mass accuracies and proteome-wide protein quantification. *Nature Biotechnology*, 26(12), 1367–1372. <https://doi.org/10.1038/nbt.1511>
- Cox, J., Neuhauser, N., Michalski, A., Scheltema, R. A., Olsen, J. V., & Mann, M. (2011). Andromeda: A peptide search engine integrated into the MaxQuant environment. *Journal of Proteome Research*, 10(4), 1794–1805. <https://doi.org/10.1021/pr101065j>
- Dellago, H., Löscher, M., Ajuh, P., Ryder, U., Kaisermayer, C., Grillari-Voglauer, R., Fortschegger, K., Gross, S., Gstraunthaler, A., Borth, N., Eisenhaber, F., Lamond, A. I., & Grillari, J. (2011). Exo70, a subunit of the exocyst complex, interacts with SNEV(hPrp19/hPso4) and is involved in pre-mRNA splicing. *The Biochemical Journal*, 438(1), 81–91. <https://doi.org/10.1042/7BBJ20110183>
- Diether, M., & Sauer, U. (2017). Towards detecting regulatory protein-metabolite interactions. *Current Opinion in Microbiology*, 39, 16–23. <https://doi.org/10.1016/j.mib.2017.07.006>
- Dong, M., Yang, L. L., Williams, K., Fisher, S. J., Hall, S. C., Biggin, M. D., Jin, J., & Witkowska, H. E. (2008). A "tagless" strategy for identification of stable protein complexes genome-wide by multidimensional orthogonal chromatographic separation and iTRAQ reagent tracking. *Journal of Proteome Research*, 7(5), 1836–1849. <https://doi.org/10.1021/pr700624e>

- Donnelly, D. P., Rawlins, C. M., DeHart, C. J., Fornelli, L., Schachner, L. F., Lin, Z., Lippens, J. L., Aluri, K. C., Sarin, R., Chen, B., Lantz, C., Jung, W., Johnson, K. R., Koller, A., Wolff, J. J., Campuzano, I. D. G., Auclair, J. R., Ivanov, A. R., Whitelegge, J. P., ... Agar, J. N. (2019). Best practices and benchmarks for intact protein analysis for top-down mass spectrometry. *Nature Methods*, *16*(7), 587–594. <https://doi.org/10.1038/s41592-019-0457-0>
- Efron, B. (2010). *Large-scale inference: Empirical bayes methods for estimation, testing, and prediction*. Cambridge University Press. <https://doi.org/10.1017/CB09780511761362>
- Elias, J. E., & Gygi, S. P. (2010). Target-decoy search strategy for mass spectrometry-based proteomics. *Methods in Molecular Biology*, *604*, 55–71. https://doi.org/10.1007/978-1-60761-444-9/_5
- Elias, J. E., & Gygi, S. P. (2007). Target-decoy search strategy for increased confidence in large-scale protein identifications by mass spectrometry. *Nature Methods*, *4*(3), 207–214. <https://doi.org/10.1038/nmeth1019>
- Ewing, R. M., Chu, P., Elisma, F., Li, H., Taylor, P., Climie, S., McBroom-Cerajewski, L., Robinson, M. D., O'Connor, L., Li, M., Taylor, R., Dharsee, M., Ho, Y., Heilbut, A., Moore, L., Zhang, S., Ornatsky, O., Bukhman, Y. V., Ethier, M., ... Figeys, D. (2007). Large-scale mapping of human protein-protein interactions by mass spectrometry. *Molecular Systems Biology*, *3*, 89. <https://doi.org/10.1038/msb4100134>
- Feng, Y., De Franceschi, G., Kahraman, A., Soste, M., Melnik, A., Boersema, P. J., Laureto, P. P. de, Nikolaev, Y., Oliveira, A. P., & Picotti, P. (2014). Global analysis of protein structural changes in complex proteomes. *Nature Biotechnology*, *32*(10), 1036–1044. <https://doi.org/10.1038/nbt.2999>
- Fenn, J. B., Mann, M., Meng, C. K., Wong, S. F., & Whitehouse, C. M. (1989). Electrospray ionization for mass spectrometry of large biomolecules. *Science*, *246*(4926), 64–71. <https://doi.org/10.1126/science.2675315>

- Feric, M., Vaidya, N., Harmon, T. S., Mitrea, D. M., Zhu, L., Richardson, T. M., Kriwacki, R. W., Pappu, R. V., & Brangwynne, C. P. (2016). Coexisting liquid phases underlie nucleolar subcompartments. *Cell*, *165*(7), 1686–1697. <https://doi.org/10.1016/j.cell.2016.04.047>
- Fisher, R. A. (1918). The correlation between relatives on the supposition of mendelian inheritance. *Transactions of the Royal Society of Edinburgh*, *52*, 399–433.
- Franken, H., Mathieson, T., Childs, D., Sweetman, G. M. A., Werner, T., Tögel, I., Doce, C., Gade, S., Bantscheff, M., Drewes, G., Reinhard, F. B. M., Huber, W., & Savitski, M. M. (2015). Thermal proteome profiling for unbiased identification of direct and indirect drug targets using multiplexed quantitative mass spectrometry. *Nature Protocols*, *10*(10), 1567–1593. <https://doi.org/10.1038/nprot.2015.101>
- Gardner, J., Pleiss, G., Weinberger, K. Q., Bindel, D., & Wilson, A. G. (2018). GPY-Torch: Blackbox matrix-matrix gaussian process inference with gpu acceleration. In S. Bengio, H. Wallach, H. Larochelle, K. Grauman, N. Cesa-Bianchi, & R. Garnett (Eds.), *Advances in neural information processing systems* (Vol. 31, pp. 7576–7586). Curran Associates, Inc. <https://proceedings.neurips.cc/paper/2018/file/27e8e17134dd7083b050476733207ea1-Paper.pdf>
- Gavin, A.-C., Bösch, M., Krause, R., Grandi, P., Marzioch, M., Bauer, A., Schultz, J., Rick, J. M., Michon, A.-M., Cruciat, C.-M., Remor, M., Höfert, C., Schelder, M., Brajenovic, M., Ruffner, H., Merino, A., Klein, K., Hudak, M., Dickson, D., ... Superti-Furga, G. (2002). Functional organization of the yeast proteome by systematic analysis of protein complexes. *Nature*, *415*(6868), 141–147. <https://doi.org/10.1038/415141a>
- Gillet, L. C., Navarro, P., Tate, S., Röst, H., Selevsek, N., Reiter, L., Bonner, R., & Aebersold, R. (2012). Targeted data extraction of the MS/MS spectra generated by data-independent acquisition: A new concept for consistent and accurate proteome analysis. *Molecular & Cellular Proteomics*, *11*(6), O111.016717. <https://doi.org/>

10.1074/mcp.0111.016717

- Gruenbaum, Y., & Foisner, R. (2015). Lamins: Nuclear intermediate filament proteins with fundamental functions in nuclear mechanics and genome regulation. *Annual Review of Biochemistry*, *84*, 131–164. <https://doi.org/10.1146/annurev-biochem-060614-034115>
- Hayes, M. H., Peuchen, E. H., Dovichi, N. J., & Weeks, D. L. (2018). Dual roles for ATP in the regulation of phase separated protein aggregates in xenopus oocyte nucleoli. *eLife*, *7*. <https://doi.org/10.7554/eLife.35224>
- Heald, R., & McKeon, F. (1990). Mutations of phosphorylation sites in lamin a that prevent nuclear lamina disassembly in mitosis. *Cell*, *61*(4), 579–589. [https://doi.org/10.1016/0092-8674\(90\)90470-y](https://doi.org/10.1016/0092-8674(90)90470-y)
- Hertel, C., Coulter, S. J., & Perkins, J. P. (1986). The involvement of cellular ATP in receptor-mediated internalization of epidermal growth factor and hormone-induced internalization of beta-adrenergic receptors. *The Journal of Biological Chemistry*, *261*(13), 5974–5980. <https://www.ncbi.nlm.nih.gov/pubmed/3009438>
- Heusel, M., Bludau, I., Rosenberger, G., Hafen, R., Frank, M., Banaei-Esfahani, A., Drogen, A. van, Collins, B. C., Gstaiger, M., & Aebersold, R. (2019). Complex-centric proteome profiling by SEC-SWATH-MS. *Molecular Systems Biology*, *15*(1), e8438. <https://doi.org/10.15252/msb.20188438>
- Holmes, S., & Huber, W. (2018). *Modern statistics for modern biology*. Cambridge University Press.
- Hornbeck, P. V., Kornhauser, J. M., Latham, V., Murray, B., Nandhikonda, V., Nord, A., Skrzypek, E., Wheeler, T., Zhang, B., & Gnad, F. (2019). 15 years of PhosphoSitePlus: Integrating post-translationally modified sites, disease variants and isoforms. *Nucleic Acids Research*, *47*(D1), D433–D441. <https://doi.org/10.1093/nar/gky1159>
- Hou, H., Wang, F., Zhang, W., Wang, D., Li, X., Bartlam, M., Yao, X., & Rao, Z. (2011).

- Structure-functional analyses of CRHSP-24 plasticity and dynamics in oxidative stress response. *The Journal of Biological Chemistry*, 286(11), 9623–9635. <https://doi.org/10.1074/jbc.M110.177436>
- Hu, L., Wang, X., Huang, Y.-A., Hu, P., & You, Z.-H. (2021). A survey on computational models for predicting protein-protein interactions. *Briefings in Bioinformatics*. <https://doi.org/10.1093/bib/bbab036>
- Hu, Q., Noll, R. J., Li, H., Makarov, A., Hardman, M., & Graham Cooks, R. (2005). The orbitrap: A new mass spectrometer. *Journal of Mass Spectrometry*, 40(4), 430–443. <https://doi.org/10.1002/jms.856>
- Huang, J. X., Lee, G., Cavanaugh, K. E., Chang, J. W., Gardel, M. L., & Moelling, R. E. (2019). High throughput discovery of functional protein modifications by hotspot thermal profiling. *Nature Methods*, 16(9), 894–901. <https://doi.org/10.1038/s41592-019-0499-3>
- Huber, W., Carey, V. J., Gentleman, R., Anders, S., Carlson, M., Carvalho, B. S., Bravo, H. C., Davis, S., Gatto, L., Girke, T., Gottardo, R., Hahne, F., Hansen, K. D., Irizarry, R. A., Lawrence, M., Love, M. I., MacDonald, J., Obenchain, V., Oleś, A. K., ... Morgan, M. (2015). Orchestrating high-throughput genomic analysis with bioconductor. *Nature Methods*, 12(2), 115–121. <https://doi.org/10.1038/nmeth.3252>
- Hughes, C. S., Moggridge, S., Müller, T., Sorensen, P. H., Morin, G. B., & Krijgsveld, J. (2019). Single-pot, solid-phase-enhanced sample preparation for proteomics experiments. *Nature Protocols*, 14(1), 68–85. <https://doi.org/10.1038/s41596-018-0082-x>
- Ingley, E. (2012). Functions of the lyn tyrosine kinase in health and disease. *Cell Communication and Signaling*, 10(1), 21. <https://doi.org/10.1186/1478-7B811X%7D-10-21>
- Jarzab, A., Kurzawa, N., Hopf, T., Moerch, M., Zecha, J., Leijten, N., Bian, Y., Musiol,

- E., Maschberger, M., Stoehr, G., Becher, I., Daly, C., Samaras, P., Mergner, J., Spanier, B., Angelov, A., Werner, T., Bantscheff, M., Wilhelm, M., ... Kuster, B. (2020). Meltome atlas-thermal proteome stability across the tree of life. *Nature Methods*, 17(5), 495–503. <https://doi.org/10.1038/s41592-020-0801-4>
- Johnson, D. S., Mortazavi, A., Myers, R. M., & Wold, B. (2007). Genome-wide mapping of in vivo protein-DNA interactions. *Science*, 316(5830), 1497–1502. <https://doi.org/10.1126/science.1141319>
- Kalxdorf, M., Günthner, I., Becher, I., Kurzawa, N., Knecht, S., Savitski, M. M., Eberl, H. C., & Bantscheff, M. (2021). Cell surface thermal proteome profiling tracks perturbations and drug targets on the plasma membrane. *Nature Methods*. <https://doi.org/10.1038/s41592-020-01022-1>
- Kammers, K., Cole, R. N., Tiengwe, C., & Ruczinski, I. (2015). Detecting significant changes in protein abundance. *EuPA Open Proteomics*, 7, 11–19. <https://doi.org/10.1016/j.euprot.2015.02.002>
- Karve, T. M., & Cheema, A. K. (2011). Small changes huge impact: The role of protein posttranslational modifications in cellular homeostasis and disease. *Journal of Amino Acids*, 2011, 207691. <https://doi.org/10.4061/2011/207691>
- Keseler, I. M., Mackie, A., Santos-Zavaleta, A., Billington, R., Bonavides-Martínez, C., Caspi, R., Fulcher, C., Gama-Castro, S., Kothari, A., Krummenacker, M., Latendresse, M., Muñoz-Rascado, L., Ong, Q., Paley, S., Peralta-Gil, M., Subhraveti, P., Velázquez-Ramírez, D. A., Weaver, D., Collado-Vides, J., ... Karp, P. D. (2017). The EcoCyc database: Reflecting new knowledge about escherichia coli k-12. *Nucleic Acids Research*, 45(D1), D543–D550. <https://doi.org/10.1093/nar/gkw1003>
- Kim, S. C., Sprung, R., Chen, Y., Xu, Y., Ball, H., Pei, J., Cheng, T., Kho, Y., Xiao, H., Xiao, L., Grishin, N. V., White, M., Yang, X.-J., & Zhao, Y. (2006). Substrate and functional diversity of lysine acetylation revealed by a proteomics survey. *Molecular Cell*, 23(4), 607–618. <https://doi.org/10.1016/j.molcel.2006.06.026>

- Kimura, T., Sakamoto, H., Appella, E., & Siraganian, R. P. (1996). Conformational changes induced in the protein tyrosine kinase p72syk by tyrosine phosphorylation or by binding of phosphorylated immunoreceptor tyrosine-based activation motif peptides. *Molecular and Cellular Biology*, *16*(4), 1471–1478. <https://doi.org/10.1128/mcb.16.4.1471>
- Kirschner, M. W. (2005). The meaning of systems biology. *Cell*, *121*(4), 503–504. <https://doi.org/10.1016/j.cell.2005.05.005>
- Kozłowski, L. P. (2017). Proteome-pI: Proteome isoelectric point database. *Nucleic Acids Research*, *45*(D1), D1112–D1116. <https://doi.org/10.1093/nar/gkw978>
- Kunz, W., Holmberg, K., & Zemb, T. (2016). Hydrotropes. *Current Opinion in Colloid & Interface Science*, *22*, 99–107. <https://doi.org/10.1016/j.cocis.2016.03.005>
- Kurzawa, N., Becher, I., Sridharan, S., Franken, H., Mateus, A., Anders, S., Bantscheff, M., Huber, W., & Savitski, M. M. (2020). A computational method for detection of ligand-binding proteins from dose range thermal proteome profiles. *Nature Communications*, *11*(1), 5783. <https://doi.org/10.1038/s41467-020-19529-8>
- Kurzawa, N., Mateus, A., & Savitski, M. M. (2020). Rtpca: An r package for differential thermal proximity coaggregation analysis. *Bioinformatics*. <https://doi.org/10.1093/bioinformatics/btaa682>
- Labesse, G., Alexandre, T., Vaupré, L., Salard-Arnaud, I., Him, J. L. K., Raynal, B., Bron, P., & Munier-Lehmann, H. (2013). MgATP regulates allostery and fiber formation in IMPDHs. *Structure*, *21*(6), 975–985. <https://doi.org/10.1016/j.str.2013.03.011>
- Landry, C. R., Levy, E. D., & Michnick, S. W. (2009). Weak functional constraints on phosphoproteomes. *Trends in Genetics*, *25*(5), 193–197. <https://doi.org/10.1016/j.tig.2009.03.003>

- Larsen, M. R., Trelle, M. B., Thingholm, T. E., & Jensen, O. N. (2006). Analysis of post-translational modifications of proteins by tandem mass spectrometry. *Biotechniques*, *40*(6), 790–798. <https://doi.org/10.2144/000112201>
- Li, J., Van Vranken, J. G., Pontano Vaites, L., Schweppe, D. K., Huttlin, E. L., Etienne, C., Nandhikonda, P., Viner, R., Robitaille, A. M., Thompson, A. H., Kuhn, K., Pike, I., Bomgarden, R. D., Rogers, J. C., Gygi, S. P., & Paulo, J. A. (2020). TMTpro reagents: A set of isobaric labeling mass tags enables simultaneous proteome-wide measurements across 16 samples. *Nature Methods*, *17*(4), 399–404. <https://doi.org/10.1038/s41592-020-0781-4>
- Li, X., Gianoulis, T. A., Yip, K. Y., Gerstein, M., & Snyder, M. (2010). Extensive in vivo metabolite-protein interactions revealed by large-scale systematic analyses. *Cell*, *143*(4), 639–650. <https://doi.org/10.1016/j.cell.2010.09.048>
- Linn, T. C., Pettit, F. H., & Reed, L. J. (1969). Alpha-keto acid dehydrogenase complexes. X. Regulation of the activity of the pyruvate dehydrogenase complex from beef kidney mitochondria by phosphorylation and dephosphorylation. *Proceedings of the National Academy of Sciences of the United States of America*, *62*(1), 234–241. <https://www.ncbi.nlm.nih.gov/pubmed/4306045>
- Lomenick, B., Hao, R., Jonai, N., Chin, R. M., Aghajan, M., Warburton, S., Wang, J., Wu, R. P., Gomez, F., Loo, J. A., Wohlschlegel, J. A., Vondriska, T. M., Pelletier, J., Herschman, H. R., Clardy, J., Clarke, C. F., & Huang, J. (2009). Target identification using drug affinity responsive target stability (DARTS). *Proceedings of the National Academy of Sciences of the United States of America*, *106*(51), 21984–21989. <https://doi.org/10.1073/pnas.0910040106>
- Loos, M. S., Ramakrishnan, R., Vranken, W., Tsigotaki, A., Tsare, E.-P., Zorzini, V., Geyter, J. D., Yuan, B., Tsamardinos, I., Klappa, M., Schymkowitz, J., Rousseau, F., Karamanou, S., & Economou, A. (2019). Structural basis of the subcellular topology landscape of escherichia coli. *Frontiers in Microbiology*, *10*, 1670. <https://doi.org/>

10.3389/fmicb.2019.01670

- Makarov, A. (2000). Electrostatic axially harmonic orbital trapping: A high-performance technique of mass analysis. *Analytical Chemistry*, *72*(6), 1156–1162. <https://doi.org/10.1021/ac991131p>
- Martinez Molina, D., Jafari, R., Ignatushchenko, M., Seki, T., Larsson, E. A., Dan, C., Sreekumar, L., Cao, Y., & Nordlund, P. (2013). Monitoring drug target engagement in cells and tissues using the cellular thermal shift assay. *Science*, *341*(6141), 84–87. <https://doi.org/10.1126/science.1233606>
- Mateus, A., Bobonis, J., Kurzawa, N., Stein, F., Helm, D., Hevler, J., Typas, A., & Savitski, M. M. (2018). Thermal proteome profiling in bacteria: Probing protein state in vivo. *Molecular Systems Biology*, *14*(7), e8242. <https://doi.org/10.15252/msb.20188242>
- Mateus, A., Hevler, J., Bobonis, J., Kurzawa, N., Shah, M., Mitošch, K., Goemans, C. V., Helm, D., Stein, F., Typas, A., & Savitski, M. M. (2020). The functional proteome landscape of escherichia coli. *Nature*, *588*(7838), 473–478. <https://doi.org/10.1038/s41586-020-3002-5>
- Mateus, A., Kurzawa, N., Becher, I., Sridharan, S., Helm, D., Stein, F., Typas, A., & Savitski, M. M. (2020). Thermal proteome profiling for interrogating protein interactions. *Molecular Systems Biology*, *16*(3), e9232. <https://doi.org/10.15252/msb.20199232>
- Mathieson, T., Franken, H., Kosinski, J., Kurzawa, N., Zinn, N., Sweetman, G., PoECKel, D., Ratnu, V. S., Schramm, M., Becher, I., Steidel, M., Noh, K.-M., Bergamini, G., Beck, M., Bantscheff, M., & Savitski, M. M. (2018). Systematic analysis of protein turnover in primary cells. *Nature Communications*, *9*(1), 689. <https://doi.org/10.1038/s41467-018-03106-1>
- Maxam, A. M., & Gilbert, W. (1977). A new method for sequencing DNA. *Proceedings*

- of the National Academy of Sciences of the United States of America, 74(2), 560–564. <https://doi.org/10.1073/pnas.74.2.560>
- Mehring, J., Do, T.-M., Touraud, D., Hohenschutz, M., Khoshima, A., Horinek, D., & Kunz, W. (2021). Hofmeister versus neuberg: Is ATP really a biological hydrotrope? *Cell Reports Physical Science*, 2(2), 100343. <https://doi.org/10.1016/j.xcrp.2021.100343>
- Michalski, A., Damoc, E., Hauschild, J.-P., Lange, O., Wiegand, A., Makarov, A., Nagaraj, N., Cox, J., Mann, M., & Horning, S. (2011). Mass spectrometry-based proteomics using q exactive, a high-performance benchtop quadrupole orbitrap mass spectrometer. *Molecular & Cellular Proteomics*, 10(9), M111.011015. <https://doi.org/10.1074/mcp.M111.011015>
- Mitrea, D. M., Cika, J. A., Stanley, C. B., Nourse, A., Onuchic, P. L., Banerjee, P. R., Phillips, A. H., Park, C.-G., Deniz, A. A., & Kriwacki, R. W. (2018). Self-interaction of NPM1 modulates multiple mechanisms of liquid-liquid phase separation. *Nature Communications*, 9(1), 842. <https://doi.org/10.1038/s41467-018-03255-3>
- Molliex, A., Temirov, J., Lee, J., Coughlin, M., Kanagaraj, A. P., Kim, H. J., Mittag, T., & Taylor, J. P. (2015). Phase separation by low complexity domains promotes stress granule assembly and drives pathological fibrillization. *Cell*, 163(1), 123–133. <https://doi.org/10.1016/j.cell.2015.09.015>
- Mu, R., Wang, Y.-B., Wu, M., Yang, Y., Song, W., Li, T., Zhang, W.-N., Tan, B., Li, A.-L., Wang, N., Xia, Q., Gong, W.-L., Wang, C.-G., Zhou, T., Guo, N., Sang, Z.-H., & Li, H.-Y. (2014). Depletion of pre-mRNA splicing factor Cdc5L inhibits mitotic progression and triggers mitotic catastrophe. *Cell Death & Disease*, 5, e1151. <https://doi.org/10.1038/cddis.2014.117>
- Nagalakshmi, U., Wang, Z., Waern, K., Shou, C., Raha, D., Gerstein, M., & Snyder, M. (2008). The transcriptional landscape of the yeast genome defined by RNA sequencing. *Science*, 320(5881), 1344–1349. <https://doi.org/10.1126/science>

1158441

- Nishi, H., Hashimoto, K., & Panchenko, A. R. (2011). Phosphorylation in protein-protein binding: Effect on stability and function. *Structure*, *19*(12), 1807–1815. <https://doi.org/10.1016/j.str.2011.09.021>
- Nurse, P., & Bissett, Y. (1981). Gene required in *g1* for commitment to cell cycle and in *g2* for control of mitosis in fission yeast. *Nature*, *292*(5823), 558–560. <https://doi.org/10.1038/292558a0>
- Oates, M. E., Romero, P., Ishida, T., Ghalwash, M., Mizianty, M. J., Xue, B., Dosztányi, Z., Uversky, V. N., Obradovic, Z., Kurgan, L., Dunker, A. K., & Gough, J. (2013). D²P²: Database of disordered protein predictions. *Nucleic Acids Research*, *41* (Database issue), D508–16. <https://doi.org/10.1093/nar/gks1226>
- Oberg, A. L., & Mahoney, D. W. (2012). Statistical methods for quantitative mass spectrometry proteomic experiments with labeling. *BMC Bioinformatics*, *13 Suppl 16*, S7. <https://doi.org/10.1186/1471-2105-13-S16-S7>
- Ochoa, D., Jarnuczak, A. F., Viéitez, C., Gehre, M., Soucheray, M., Mateus, A., Kleefeldt, A. A., Hill, A., Garcia-Alonso, L., Stein, F., Krogan, N. J., Savitski, M. M., Swaney, D. L., Vizcaíno, J. A., Noh, K.-M., & Beltrao, P. (2020). The functional landscape of the human phosphoproteome. *Nature Biotechnology*, *38*(3), 365–373. <https://doi.org/10.1038/s41587-019-0344-3>
- Olson, D. E., Udeshi, N. D., Wolfson, N. A., Pitcairn, C. A., Sullivan, E. D., Jaffe, J. D., Svinkina, T., Natoli, T., Lu, X., Paulk, J., McCarren, P., Wagner, F. F., Barker, D., Howe, E., Lazzaro, F., Gale, J. P., Zhang, Y.-L., Subramanian, A., Fierke, C. A., ... Holson, E. B. (2014). An unbiased approach to identify endogenous substrates of "histone" deacetylase 8. *ACS Chemical Biology*, *9*(10), 2210–2216. <https://doi.org/10.1021/cb500492r>
- Ong, S.-E., Blagoev, B., Kratchmarova, I., Kristensen, D. B., Steen, H., Pandey, A.,

- & Mann, M. (2002). Stable isotope labeling by amino acids in cell culture, SILAC, as a simple and accurate approach to expression proteomics. *Molecular & Cellular Proteomics*, 1(5), 376–386. <https://doi.org/10.1074/mcp.m200025-mcp200>
- Ong, S.-E., Kratchmarova, I., & Mann, M. (2003). Properties of ¹³C-substituted arginine in stable isotope labeling by amino acids in cell culture (SILAC). *Journal of Proteome Research*, 2(2), 173–181. <https://doi.org/10.1021/pr0255708>
- O'Reilly, F. J., & Rappsilber, J. (2018). Cross-linking mass spectrometry: Methods and applications in structural, molecular and systems biology. *Nature Structural & Molecular Biology*, 25(11), 1000–1008. <https://doi.org/10.1038/s41594-018-0147-0>
- Ori, A., Iskar, M., Buczak, K., Kastritis, P., Parca, L., Andrés-Pons, A., Singer, S., Bork, P., & Beck, M. (2016). Spatiotemporal variation of mammalian protein complex stoichiometries. *Genome Biology*, 17, 47. <https://doi.org/10.1186/s13059-016-0912-5>
- Ow, S. Y., Salim, M., Noirel, J., Evans, C., & Wright, P. C. (2011). Minimising iTRAQ ratio compression through understanding LC-MS elution dependence and high-resolution HILIC fractionation. *Proteomics*, 11(11), 2341–2346. <https://doi.org/10.1002/pmic.201000752>
- Pagès, H., Carlson, M., Falcon, S., & Li, N. (2020). *AnnotationDbi: Manipulation of sqlite-based annotations in bioconductor*.
- Pappireddi, N., Martin, L., & Wühr, M. (2019). A review on quantitative multiplexed proteomics. *Chembiochem*, 20(10), 1210–1224. <https://doi.org/10.1002/cbic.201800650>
- Patel, A., Malinowska, L., Saha, S., Wang, J., Alberti, S., Krishnan, Y., & Hyman, A. A. (2017). ATP as a biological hydrotrope. *Science*, 356(6339), 753–756. <https://doi.org/10.1126/science.aaf6846>
- Peng, J., Schwartz, D., Elias, J. E., Thoreen, C. C., Cheng, D., Marsischky, G., Roelofs, J., Finley, D., & Gygi, S. P. (2003). A proteomics approach to understanding protein

- ubiquitination. *Nature Biotechnology*, *21*(8), 921–926. <https://doi.org/10.1038/nbt849>
- Perrin, J., Werner, T., Kurzawa, N., Rutkowska, A., Childs, D. D., Kalxdorf, M., Poeckel, D., Stonehouse, E., Strohmer, K., Heller, B., Thomson, D. W., Krause, J., Becher, I., Eberl, H. C., Vappiani, J., Sevin, D. C., Rau, C. E., Franken, H., Huber, W., ... Bergamini, G. (2020). Identifying drug targets in tissues and whole blood with thermal-shift profiling. *Nature Biotechnology*, *38*(3), 303–308. <https://doi.org/10.1038/s41587-019-0388-4>
- Pfeiffer, J. R., McAvoy, B. L., Fecteau, R. E., Deleault, K. M., & Brooks, S. A. (2011). CARHSP1 is required for effective tumor necrosis factor alpha mRNA stabilization and localizes to processing bodies and exosomes. *Molecular and Cellular Biology*, *31*(2), 277–286. <https://doi.org/10.1128/MCB.00775-10>
- Phizicky, E. M., & Fields, S. (1995). Protein-protein interactions: Methods for detection and analysis. *Microbiological Reviews*, *59*(1), 94–123. <https://doi.org/10.1128/MMBR.59.1.94-123.1995>
- Piazza, I., Kochanowski, K., Cappelletti, V., Fuhrer, T., Noor, E., Sauer, U., & Picotti, P. (2018). A map of protein-metabolite interactions reveals principles of chemical communication. *Cell*, *172*(1-2), 358–372.e23. <https://doi.org/10.1016/j.cell.2017.12.006>
- Pinkse, M. W. H., Lemeer, S., & Heck, A. J. R. (2011). A protocol on the use of titanium dioxide chromatography for phosphoproteomics. *Methods in Molecular Biology*, *753*, 215–228. https://doi.org/10.1007/978-1-61779-148-2/_14
- Potel, C. M., Kurzawa, N., Becher, I., Typas, A., Mateus, A., & Savitski, M. M. (2021). Impact of phosphorylation on thermal stability of proteins. *Nature Methods*, *accepted*. <https://doi.org/10.1101/2020.01.14.903849>
- Potel, C. M., Lin, M.-H., Heck, A. J. R., & Lemeer, S. (2018). Defeating major con-

- taminants in fe³⁺- immobilized metal ion affinity chromatography (IMAC) phosphopeptide enrichment. *Molecular & Cellular Proteomics*, 17(5), 1028–1034. <https://doi.org/10.1074/mcp.TIR117.000518>
- Pratt, J. M., Petty, J., Riba-Garcia, I., Robertson, D. H. L., Gaskell, S. J., Oliver, S. G., & Beynon, R. J. (2002). Dynamics of protein turnover, a missing dimension in proteomics. *Molecular & Cellular Proteomics*, 1(8), 579–591. <https://doi.org/10.1074/mcp.m200046-mcp200>
- Prunuske, A. J., Liu, J., Elgort, S., Joseph, J., Dasso, M., & Ullman, K. S. (2006). Nuclear envelope breakdown is coordinated by both nup358/RanBP2 and nup153, two nucleoporins with zinc finger modules. *Molecular Biology of the Cell*, 17(2), 760–769. <https://doi.org/10.1091/mbc.E05-06-0485>
- Rai, A. K., Chen, J.-X., Selbach, M., & Pelkmans, L. (2018). Kinase-controlled phase transition of membraneless organelles in mitosis. *Nature*, 559(7713), 211–216. <https://doi.org/10.1038/s41586-018-0279-8>
- R Core Team. (2020). *R: A language and environment for statistical computing*. R Foundation for Statistical Computing. <https://www.R-project.org/>
- Reinhard, F. B. M., Eberhard, D., Werner, T., Franken, H., Childs, D., Doce, C., Savitski, M. F., Huber, W., Bantscheff, M., Savitski, M. M., & Drewes, G. (2015). Thermal proteome profiling monitors ligand interactions with cellular membrane proteins. *Nature Methods*, 12(12), 1129–1131. <https://doi.org/10.1038/nmeth.3652>
- Reinhardt, H. C., Hasskamp, P., Schmedding, I., Morandell, S., Vugt, M. A. T. M. van, Wang, X., Linding, R., Ong, S.-E., Weaver, D., Carr, S. A., & Yaffe, M. B. (2010). DNA damage activates a spatially distinct late cytoplasmic cell-cycle checkpoint network controlled by MK2-mediated RNA stabilization. *Molecular Cell*, 40(1), 34–49. <https://doi.org/10.1016/j.molcel.2010.09.018>
- Reznik, E., Christodoulou, D., Goldford, J. E., Briars, E., Sauer, U., Segrè, D., & Noor, E.

- (2017). Genome-scale architecture of small molecule regulatory networks and the fundamental trade-off between regulation and enzymatic activity. *Cell Reports*, *20*(11), 2666–2677. <https://doi.org/10.1016/j.celrep.2017.08.066>
- Rinschen, M. M., Ivanisevic, J., Giera, M., & Siuzdak, G. (2019). Identification of bioactive metabolites using activity metabolomics. *Nature Reviews. Molecular Cell Biology*, *20*(6), 353–367. <https://doi.org/10.1038/s41580-019-0108-4>
- Ritchie, M. E., Phipson, B., Wu, D., Hu, Y., Law, C. W., Shi, W., & Smyth, G. K. (2015). Limma powers differential expression analyses for RNA-sequencing and microarray studies. *Nucleic Acids Research*, *43*(7), e47. <https://doi.org/10.1093/nar/gkv007>
- Ritz, C., Baty, F., Streibig, J. C., & Gerhard, D. (2015). Dose-response analysis using r. *Plos One*, *10*(12), e0146021. <https://doi.org/10.1371/journal.pone.0146021>
- Robertson, G., Hirst, M., Bainbridge, M., Bilenky, M., Zhao, Y., Zeng, T., Euskirchen, G., Bernier, B., Varhol, R., Delaney, A., Thiessen, N., Griffith, O. L., He, A., Marra, M., Snyder, M., & Jones, S. (2007). Genome-wide profiles of STAT1 DNA association using chromatin immunoprecipitation and massively parallel sequencing. *Nature Methods*, *4*(8), 651–657. <https://doi.org/10.1038/nmeth1068>
- Ross, P. L., Huang, Y. N., Marchese, J. N., Williamson, B., Parker, K., Hattan, S., Khainovski, N., Pillai, S., Dey, S., Daniels, S., Purkayastha, S., Juhasz, P., Martin, S., Bartlet-Jones, M., He, F., Jacobson, A., & Pappin, D. J. (2004). Multiplexed protein quantitation in *saccharomyces cerevisiae* using amine-reactive isobaric tagging reagents. *Molecular & Cellular Proteomics*, *3*(12), 1154–1169. <https://doi.org/10.1074/mcp.M400129-MCP200>
- Rousseau, S., Morrice, N., Peggie, M., Campbell, D. G., Gaestel, M., & Cohen, P. (2002). Inhibition of SAPK2a/p38 prevents hnRNP a0 phosphorylation by MAPKAP-k2 and its interaction with cytokine mRNAs. *The EMBO Journal*, *21*(23), 6505–6514. <https://doi.org/10.1093/emboj/cdf639>

- Roux, K. J., Kim, D. I., Raida, M., & Burke, B. (2012). A promiscuous biotin ligase fusion protein identifies proximal and interacting proteins in mammalian cells. *The Journal of Cell Biology*, *196*(6), 801–810. <https://doi.org/10.1083/jcb.201112098>
- Samwer, M., Schneider, M. W. G., Hoefler, R., Schmalhorst, P. S., Jude, J. G., Zuber, J., & Gerlich, D. W. (2017). DNA cross-bridging shapes a single nucleus from a set of mitotic chromosomes. *Cell*, *170*(5), 956–972.e23. <https://doi.org/10.1016/j.cell.2017.07.038>
- Sanger, F., Nicklen, S., & Coulson, A. R. (1977). DNA sequencing with chain-terminating inhibitors. *Proceedings of the National Academy of Sciences of the United States of America*, *74*(12), 5463–5467. <https://doi.org/10.1073/pnas.74.12.5463>
- Savitski, M. M., Mathieson, T., Zinn, N., Sweetman, G., Doce, C., Becher, I., Pachel, F., Kuster, B., & Bantscheff, M. (2013). Measuring and managing ratio compression for accurate iTRAQ/TMT quantification. *Journal of Proteome Research*, *12*(8), 3586–3598. <https://doi.org/10.1021/pr400098r>
- Savitski, M. M., Reinhard, F. B. M., Franken, H., Werner, T., Savitski, M. F., Eberhard, D., Martinez Molina, D., Jafari, R., Dovega, R. B., Klaeger, S., Kuster, B., Nordlund, P., Bantscheff, M., & Drewes, G. (2014). Tracking cancer drugs in living cells by thermal profiling of the proteome. *Science*, *346*(6205), 1255784. <https://doi.org/10.1126/science.1255784>
- Savitski, M. M., Wilhelm, M., Hahne, H., Kuster, B., & Bantscheff, M. (2015). A scalable approach for protein false discovery rate estimation in large proteomic data sets. *Molecular & Cellular Proteomics*, *14*(9), 2394–2404. <https://doi.org/10.1074/mcp.M114.046995>
- Savitski, M. M., Zinn, N., Faelth-Savitski, M., PoECKel, D., Gade, S., Becher, I., Muelbaier, M., Wagner, A. J., Strohmer, K., Werner, T., Melchert, S., Petretich, M., Rutkowska, A., Vappiani, J., Franken, H., Steidel, M., Sweetman, G. M., Gilan, O., Lam, E. Y. N., ... Bantscheff, M. (2018). Multiplexed proteome dynamics profil-

- ing reveals mechanisms controlling protein homeostasis. *Cell*, 173(1), 260–274.e25. <https://doi.org/10.1016/j.cell.2018.02.030>
- Schena, M., Shalon, D., Davis, R. W., & Brown, P. O. (1995). Quantitative monitoring of gene expression patterns with a complementary DNA microarray. *Science*, 270(5235), 467–470. <https://doi.org/10.1126/science.270.5235.467>
- Schwanhäusser, B., Busse, D., Li, N., Dittmar, G., Schuchhardt, J., Wolf, J., Chen, W., & Selbach, M. (2011). Global quantification of mammalian gene expression control. *Nature*, 473(7347), 337–342. <https://doi.org/10.1038/nature10098>
- Selkig, J., Stanifer, M., Mateus, A., Mitosch, K., Barrio-Hernandez, I., Rettel, M., Kim, H., Voogdt, C., Walch, P., Kee, C., Kurzawa, N., Stein, F., Potel, C., Jarzab, A., Kuster, B., Bartenschlager, R., Boulant, S., Beltrao, P., Typas, A., & Savitski, M. (2020). SARS-CoV-2 infection remodels the host protein thermal stability landscape. *Preprint*. <https://doi.org/10.21203/rs.3.rs-105193/v1>
- Shi, T., Song, E., Nie, S., Rodland, K. D., Liu, T., Qian, W.-J., & Smith, R. D. (2016). Advances in targeted proteomics and applications to biomedical research. *Proteomics*, 16(15-16), 2160–2182. <https://doi.org/10.1002/pmic.201500449>
- Simon, G. M., Niphakis, M. J., & Cravatt, B. F. (2013). Determining target engagement in living systems. *Nature Chemical Biology*, 9(4), 200–205. <https://doi.org/10.1038/nchembio.1211>
- Smith, I. R., Hess, K. N., Bakhtina, A., Valente, A. S., Rodriguez-Mias, R. A., & Villen, J. (2020). Identification of phosphosites that alter protein thermal stability. *BioRxiv*. <https://doi.org/10.1101/2020.01.14.904300>
- Smyth, G. K. (2004). Linear models and empirical bayes methods for assessing differential expression in microarray experiments. *Statistical Applications in Genetics and Molecular Biology*, 3, Article3. <https://doi.org/10.2202/1544-6115.1027>
- Sridharan, S., Kurzawa, N., Werner, T., Günthner, I., Helm, D., Huber, W., Bantscheff,

- M., & Savitski, M. M. (2019). Proteome-wide solubility and thermal stability profiling reveals distinct regulatory roles for ATP. *Nature Communications*, *10*(1), 1155. <https://doi.org/10.1038/s41467-019-09107-y>
- Srivastava, S., Olson, H. E., Cohen, J. S., Gubbels, C. S., Lincoln, S., Davis, B. T., Shahmirzadi, L., Gupta, S., Picker, J., Yu, T. W., Miller, D. T., Soul, J. S., Poretti, A., & Naidu, S. (2016). BRAT1 mutations present with a spectrum of clinical severity. *American Journal of Medical Genetics. Part A*, *170*(9), 2265–2273. <https://doi.org/10.1002/ajmg.a.37783>
- Storey, J. D., Xiao, W., Leek, J. T., Tompkins, R. G., & Davis, R. W. (2005). Significance analysis of time course microarray experiments. *Proceedings of the National Academy of Sciences of the United States of America*, *102*(36), 12837–12842. <https://doi.org/10.1073/pnas.0504609102>
- Szklarczyk, D., Gable, A. L., Lyon, D., Junge, A., Wyder, S., Huerta-Cepas, J., Simonovic, M., Doncheva, N. T., Morris, J. H., Bork, P., Jensen, L. J., & Mering, C. von. (2019). STRING v11: Protein-protein association networks with increased coverage, supporting functional discovery in genome-wide experimental datasets. *Nucleic Acids Research*, *47*(D1), D607–D613. <https://doi.org/10.1093/nar/gky1131>
- Tan, C. S. H., Go, K. D., Bisteau, X., Dai, L., Yong, C. H., Prabhu, N., Ozturk, M. B., Lim, Y. T., Sreekumar, L., Lengqvist, J., Tergaonkar, V., Kaldis, P., Sobota, R. M., & Nordlund, P. (2018). Thermal proximity coaggregation for system-wide profiling of protein complex dynamics in cells. *Science*, *359*(6380), 1170–1177. <https://doi.org/10.1126/science.aan0346>
- Tanenbaum, M. E., Stern-Ginossar, N., Weissman, J. S., & Vale, R. D. (2015). Regulation of mRNA translation during mitosis. *eLife*, *4*. <https://doi.org/10.7554/eLife.07957>
- Thompson, A., Schäfer, J., Kuhn, K., Kienle, S., Schwarz, J., Schmidt, G., Neumann, T., Johnstone, R., Mohammed, A. K. A., & Hamon, C. (2003). Tandem mass tags:

- A novel quantification strategy for comparative analysis of complex protein mixtures by MS/MS. *Analytical Chemistry*, 75(8), 1895–1904. <https://doi.org/10.1021/ac0262560>
- Thomson, J. J. (1913). *Rays of positive electricity and their application to chemical analyses*. Longmans Green & Co.
- Tian, S.-Y., Chen, S.-H., Shao, B.-F., Cai, H.-Y., Zhou, Y., Zhou, Y.-L., & Xu, A.-B. (2014). Expression of leucine aminopeptidase 3 (LAP3) correlates with prognosis and malignant development of human hepatocellular carcinoma (HCC). *International Journal of Clinical and Experimental Pathology*, 7(7), 3752–3762. <https://www.ncbi.nlm.nih.gov/pubmed/25120751>
- Traut, T. W. (1994). Physiological concentrations of purines and pyrimidines. *Molecular and Cellular Biochemistry*, 140(1), 1–22. <https://doi.org/10.1007/BF00928361>
- Tsuura, Y., Fujimoto, S., Kajikawa, M., Ishida, H., & Seino, Y. (1999). Regulation of intracellular ATP concentration under conditions of reduced ATP consumption in pancreatic islets. *Biochemical and Biophysical Research Communications*, 261(2), 439–444. <https://doi.org/10.1006/bbrc.1999.1052>
- Tukey, J. W. (1949). Comparing individual means in the analysis of variance. *Biometrics*, 5(2), 99–114. <https://doi.org/10.2307/3001913>
- Vraneš, M., Panić, J., Tot, A., Gadžurić, S., Podlipnik, Č., & Bešter-Rogač, M. (2020). How the presence of ATP affect caffeine hydration and self-aggregation? *Journal of Molecular Liquids*, 318, 113885. <https://doi.org/10.1016/j.molliq.2020.113885>
- Wang, J., Choi, J.-M., Holehouse, A. S., Lee, H. O., Zhang, X., Jahnel, M., Maharana, S., Lemaitre, R., Pozniakovsky, A., Drechsel, D., Poser, I., Pappu, R. V., Alberti, S., & Hyman, A. A. (2018). A molecular grammar governing the driving forces for phase separation of prion-like RNA binding proteins. *Cell*, 174(3), 688–699.e16. <https://doi.org/10.1016/j.cell.2018.06.006>

- Wang, X., Shi, L., Deng, Y., Qu, M., Mao, S., Xu, L., Xu, W., & Fang, C. (2015). Inhibition of leucine aminopeptidase 3 suppresses invasion of ovarian cancer cells through down-regulation of fascin and MMP-2/9. *European Journal of Pharmacology*, *768*, 116–122. <https://doi.org/10.1016/j.ejphar.2015.10.039>
- Watson, P. J., Fairall, L., Santos, G. M., & Schwabe, J. W. R. (2012). Structure of HDAC3 bound to co-repressor and inositol tetrakisphosphate. *Nature*, *481*(7381), 335–340. <https://doi.org/10.1038/nature10728>
- Welch, B. L. (1947). The generalization of "student's" problem when several different population variances are involved. *Biometrika*, *34*(1-2), 28–35. <https://doi.org/10.1093/biomet/34.1-2.28>
- Werner, T., Becher, I., Sweetman, G., Doce, C., Savitski, M. M., & Bantscheff, M. (2012). High-resolution enabled TMT 8-plexing. *Analytical Chemistry*, *84*(16), 7188–7194. <https://doi.org/10.1021/ac301553x>
- Werner, T., Sweetman, G., Savitski, M. F., Mathieson, T., Bantscheff, M., & Savitski, M. M. (2014). Ion coalescence of neutron encoded TMT 10-plex reporter ions. *Analytical Chemistry*, *86*(7), 3594–3601. <https://doi.org/10.1021/ac500140s>
- West, G. M., Tang, L., & Fitzgerald, M. C. (2008). Thermodynamic analysis of protein stability and ligand binding using a chemical modification- and mass spectrometry-based strategy. *Analytical Chemistry*, *80*(11), 4175–4185. <https://doi.org/10.1021/ac702610a>
- West, G. M., Tucker, C. L., Xu, T., Park, S. K., Han, X., Yates, J. R., & Fitzgerald, M. C. (2010). Quantitative proteomics approach for identifying protein-drug interactions in complex mixtures using protein stability measurements. *Proceedings of the National Academy of Sciences of the United States of America*, *107*(20), 9078–9082. <https://doi.org/10.1073/pnas.1000148107>
- Wickham, H. (2016). *Ggplot2: Elegant graphics for data analysis*. Springer-Verlag New

- York. <https://ggplot2.tidyverse.org>
- Wilke, C. O. (2019). *Cowplot: Streamlined plot theme and plot annotations for 'ggplot2'*. <https://CRAN.R-project.org/package=cowplot>
- Xu, W., Doshi, A., Lei, M., Eck, M. J., & Harrison, S. C. (1999). Crystal structures of c-src reveal features of its autoinhibitory mechanism. *Molecular Cell*, 3(5), 629–638. [https://doi.org/10.1016/s1097-2765\(00\)80356-1](https://doi.org/10.1016/s1097-2765(00)80356-1)
- Yang, G. X., Li, X., & Snyder, M. (2012). Investigating metabolite-protein interactions: An overview of available techniques. *Methods*, 57(4), 459–466. <https://doi.org/10.1016/j.ymeth.2012.06.013>
- Yang, Y., Liu, X., Shen, C., Lin, Y., Yang, P., & Qiao, L. (2020). In silico spectral libraries by deep learning facilitate data-independent acquisition proteomics. *Nature Communications*, 11(1), 146. <https://doi.org/10.1038/s41467-019-13866-z>
- Young, M. A., Gonfloni, S., Superti-Furga, G., Roux, B., & Kuriyan, J. (2001). Dynamic coupling between the SH2 and SH3 domains of c-src and hck underlies their inactivation by c-terminal tyrosine phosphorylation. *Cell*, 105(1), 115–126. [https://doi.org/10.1016/s0092-8674\(01\)00301-4](https://doi.org/10.1016/s0092-8674(01)00301-4)
- Yu, G., Wang, L.-G., Han, Y., & He, Q.-Y. (2012). ClusterProfiler: An r package for comparing biological themes among gene clusters. *OMICS: A Journal of Integrative Biology*, 16(5), 284–287. <https://doi.org/10.1089/omi.2011.0118>
- Zemanová, L., Navrátilová, H., Andrýs, R., Šperková, K., Andrejs, J., Kozáková, K., Meier, M., Möller, G., Novotná, E., Šafr, M., Adamski, J., & Wsól, V. (2019). Initial characterization of human DHRS1 (SDR19C1), a member of the short-chain dehydrogenase/reductase superfamily. *The Journal of Steroid Biochemistry and Molecular Biology*, 185, 80–89. <https://doi.org/10.1016/j.jsbmb.2018.07.013>
- Zinn, N., Werner, T., Doce, C., Mathieson, T., Boecker, C., Sweetman, G., Fufezan, C., & Bantscheff, M. (2021). Improved proteomics-based drug mechanism-of-action

studies using 16-plex isobaric mass tags. *Journal of Proteome Research*. <https://doi.org/10.1021/acs.jproteome.0c00900>

Appendix

Sensitivity analysis of the DLPTP model

To perform a sensitivity analysis of the DLPTP model for 2D-TPP analysis, introduced in Chapter 4, we picked two different 2D thermal profiles: 1) the profile of BRD4 from the JQ1 HL-60 lysate dataset, an example of profile very well explained by the DLPTP model, and 2) the profile of HDAC6 taken from the Panobinostat intact cell dataset, resembling a profile from which the model could not identify HDAC6 as ligand binding, even though it is a known target of Panobinostat.

For our analysis we repeatedly subsampled 90% of the data points of the two profiles and fitted the null and alternative model on the obtained datasets. For BRD4 we observed no dramatic effects on the obtained fits (Figure S1a). Obtained parameter distributions and inter-correlations did also not reveal any surprising relations (Figure S1b). For HDAC6, however, while obtained fits on data point subsamples were broadly consistent (Figure S2a), it became clear that obtained F -statistics for some subsamples were much higher than for the full profile (Figure S2b). This indicates that a few outlier data points lead to the low observed F -statistic of the full profile and thus the inability of DLPTP to pick up HDAC6 as significantly stabilized by Panobinostat.

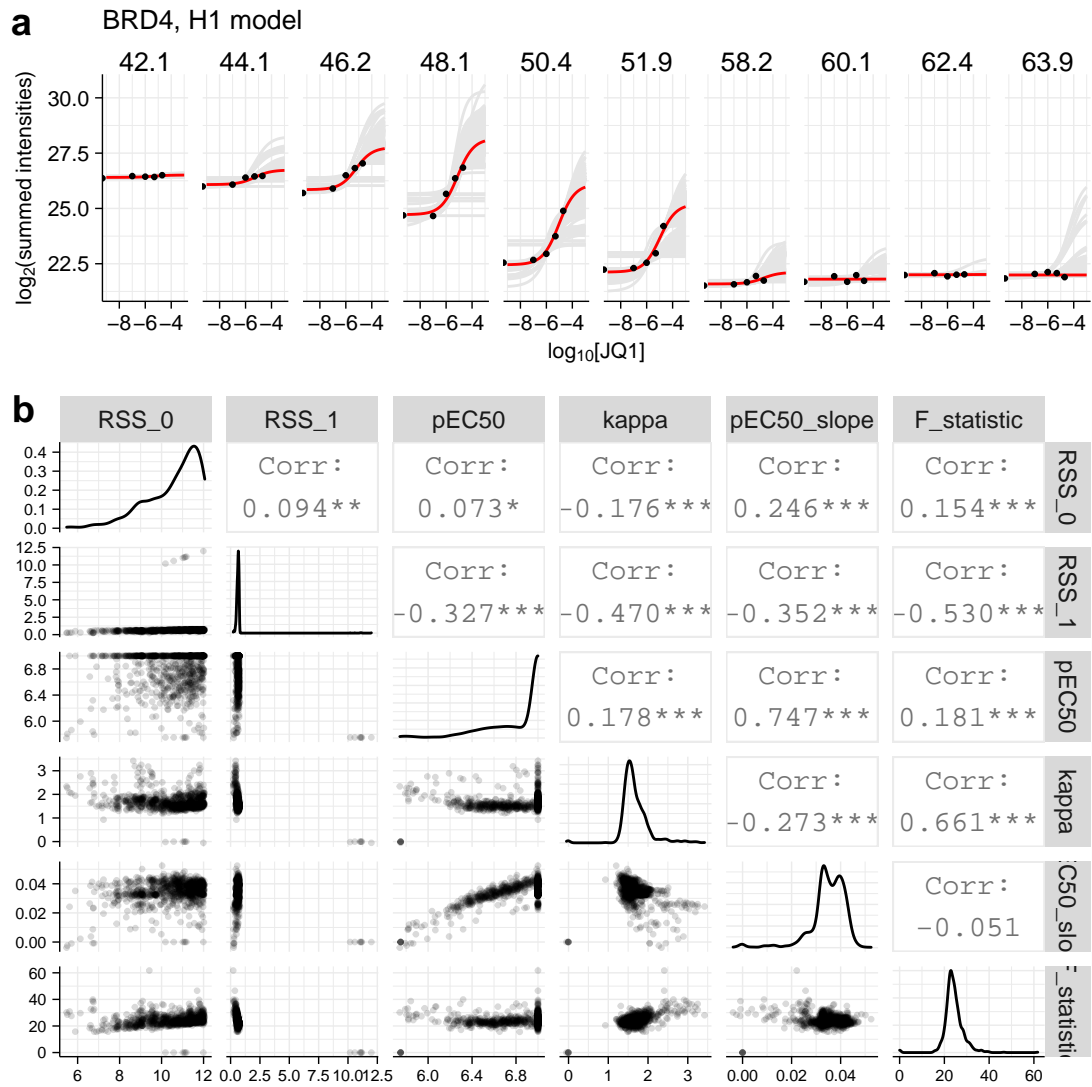


Figure S1: Sensitivity analysis based on the example of BRD4 in the JQ1 lysate dataset. a) Comparison of DLPTP alternative model fits on subsamples and all data points (red). b) Correlation of parameters obtained for different subsamples of data points.

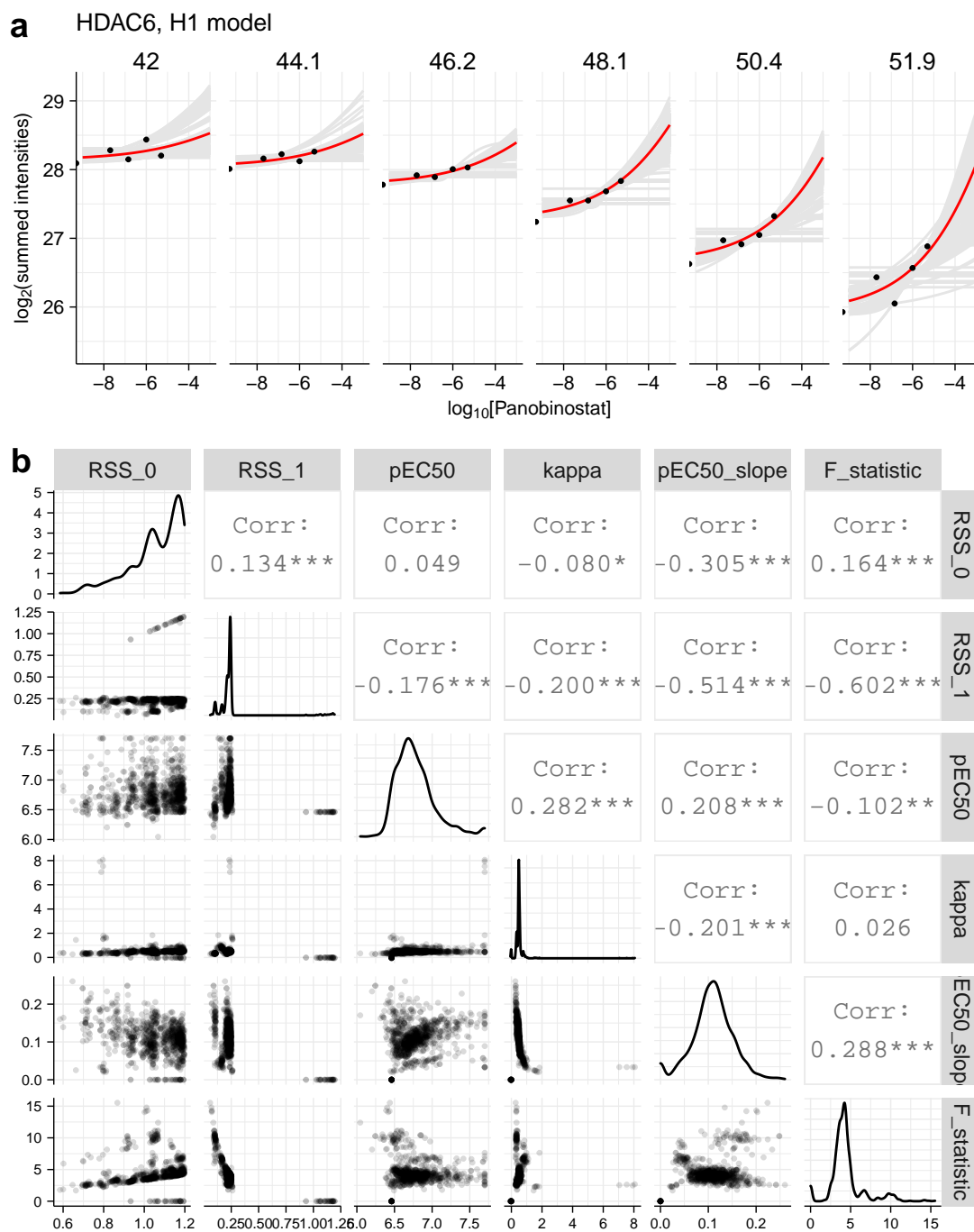


Figure S2: Sensitivity analysis based on the example of the HDAC6 in the Panobinostat in-cell dataset. a) Comparison of DLTP alternative model fits on subsamples and all data points (red). b) Correlation of parameters obtained for different subsamples of data points.

Supplementary Figures

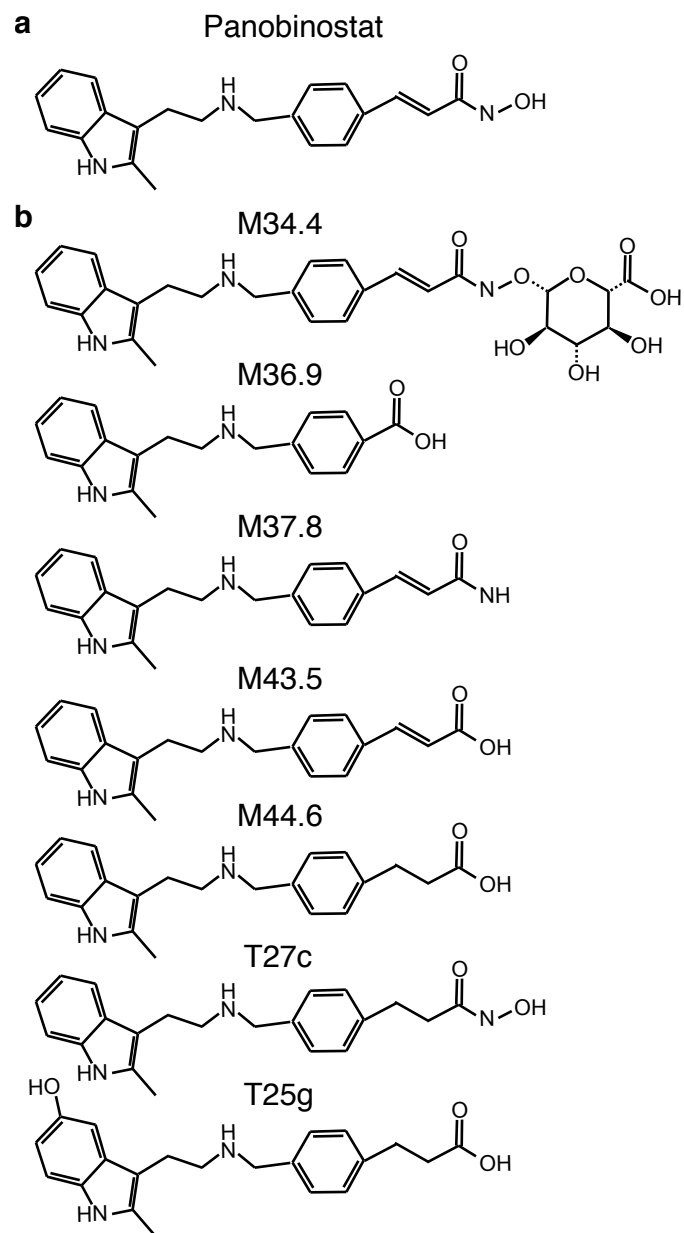


Figure S3: Chemical structures of Panobinostat and some of its metabolized forms. Chemical structures of a) Panobinostat and b) some of its metabolized forms.

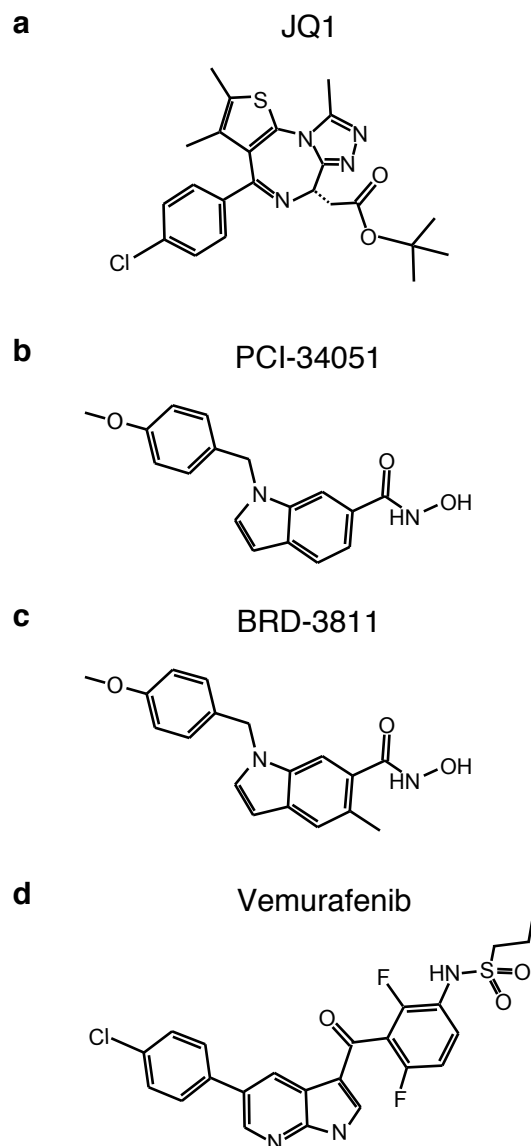


Figure S4: Chemical structures of further small molecules used in this work. Chemical structures of a) JQ1, b) PCI-34051, c) BRD-3811 and d) Vemurafenib.

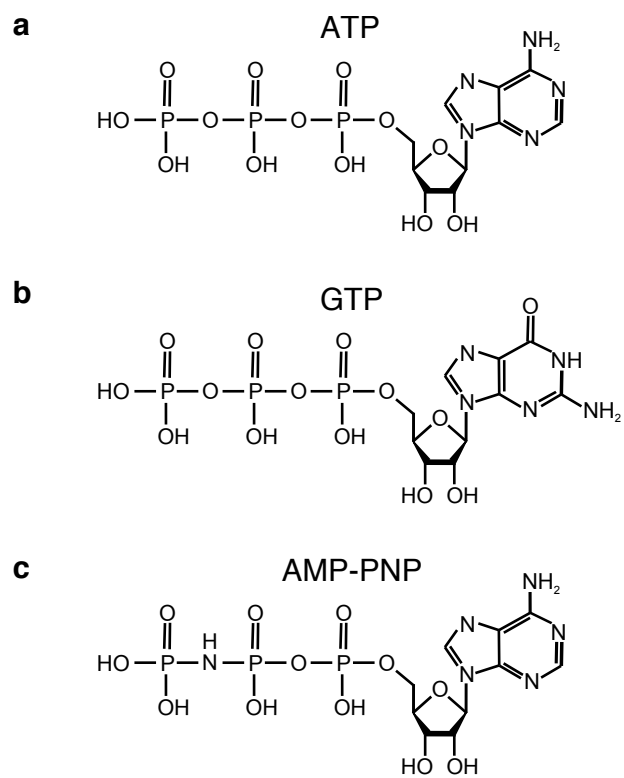


Figure S5: Chemical structures of metabolites and analogs used in this work. Chemical structures of a) ATP, b) GTP and c) AMP-PNP.

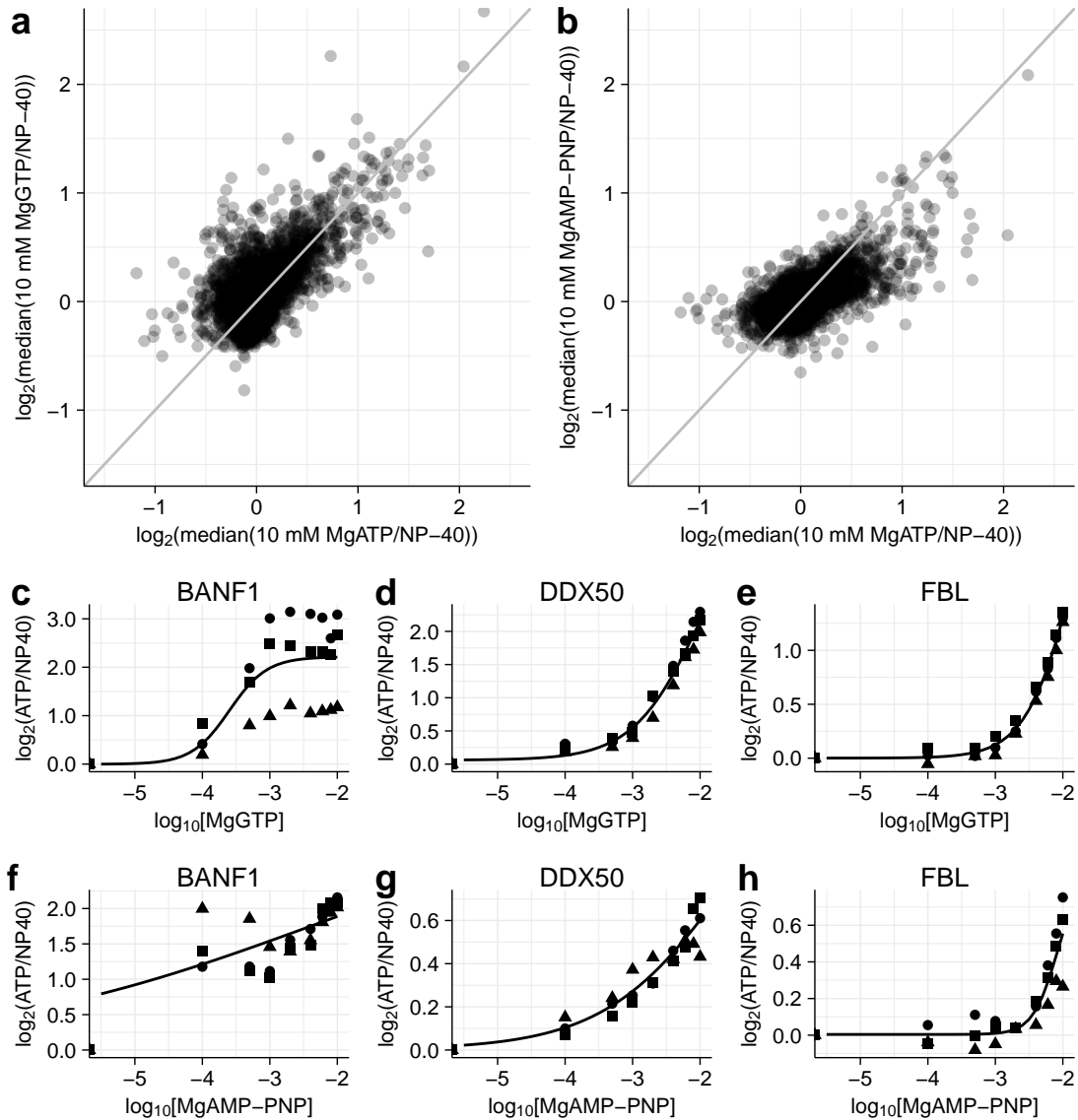


Figure S6: Controls experiments to confirm ATP's effect on insoluble proteins is not driven by ATP hydrolysis. Scatterplots of median fold changes at maximal compound concentration of a) MgGTP vs. MgATP and b) MgAMP-PNP vs. MgATP. Solubility profiles of representative proteins in the presence of different concentrations of MgGTP (c-e) and MgAMP-PNP (f-h).

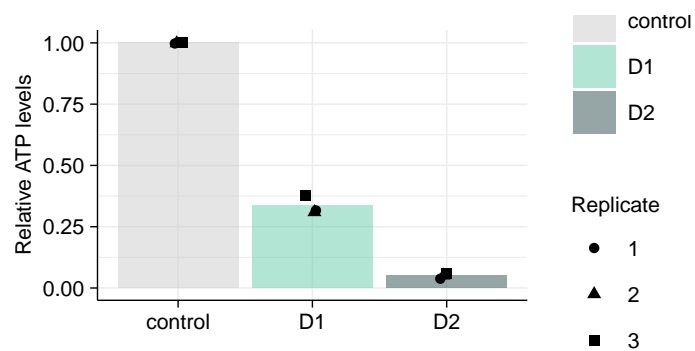


Figure S7: Intracellular ATP levels after depletion with D1 and D2. Measurements were performed with the Cell-Titer Glow assay. D1: 0.1 nM AA and 1 mM 2DG, D2: 1 nM AA and 10 mM 2DG.

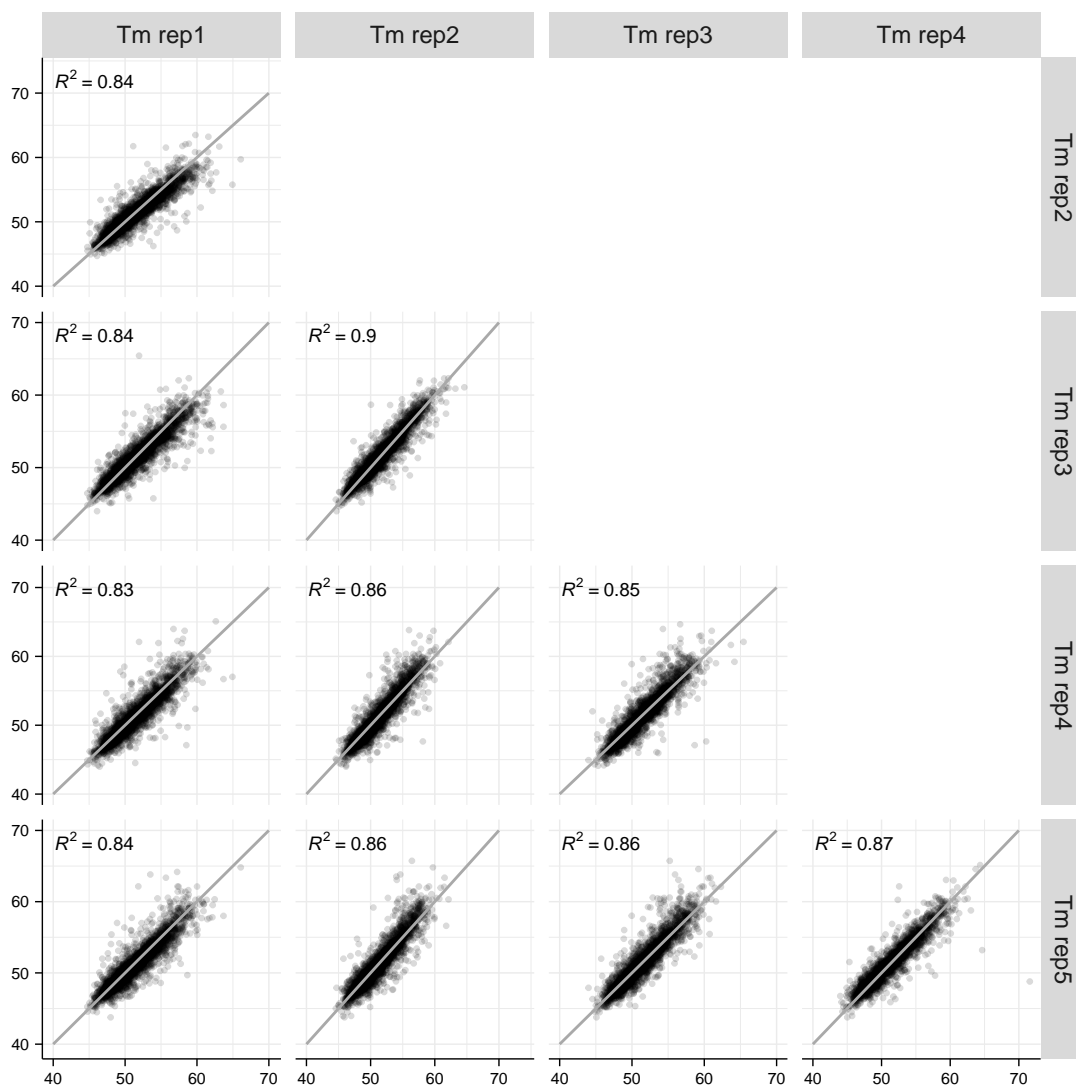


Figure S8: Comparison of melting point estimates obtained from different replicates of unmodified proteins.

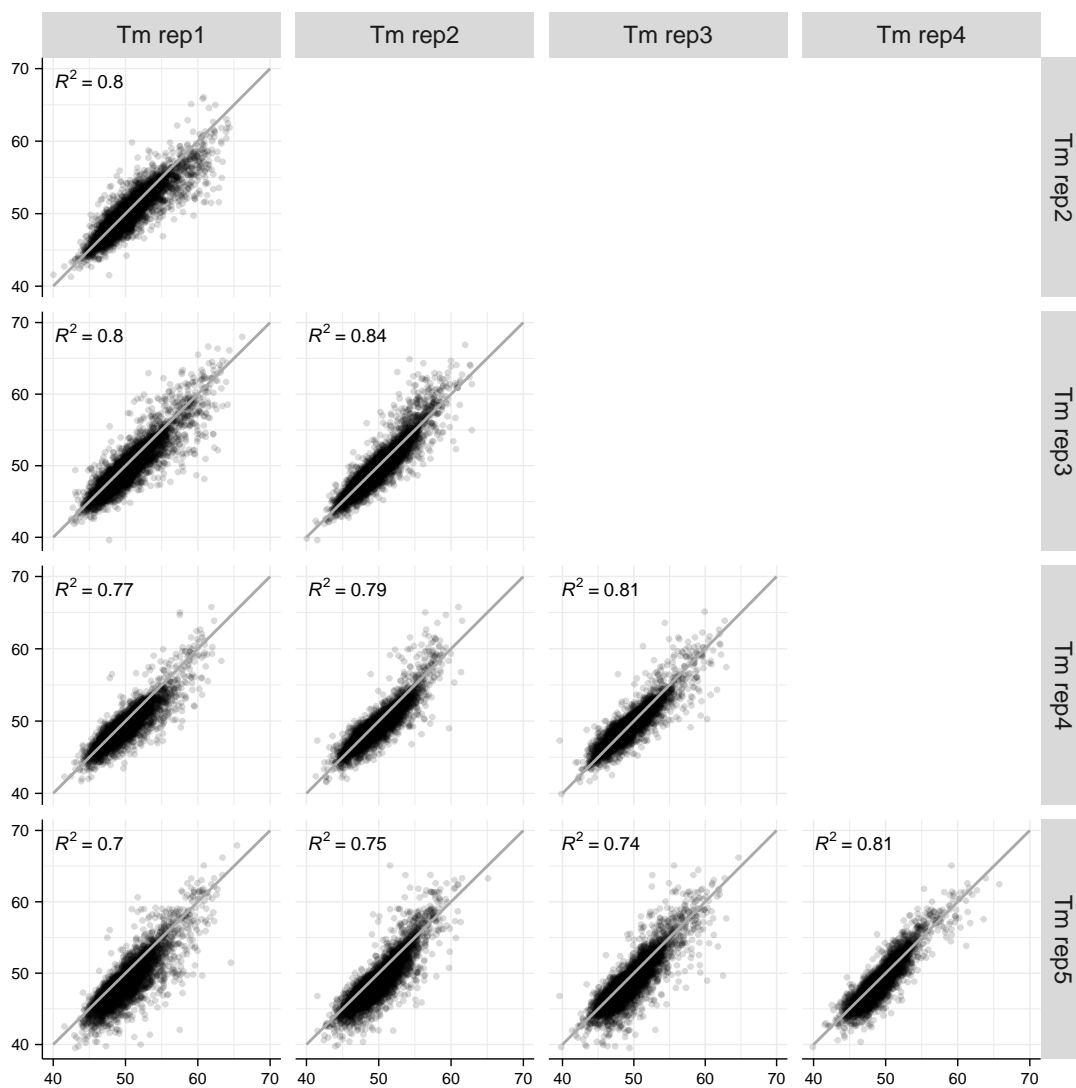


Figure S9: Comparison of melting point estimates obtained from different replicates of phosphopeptides.

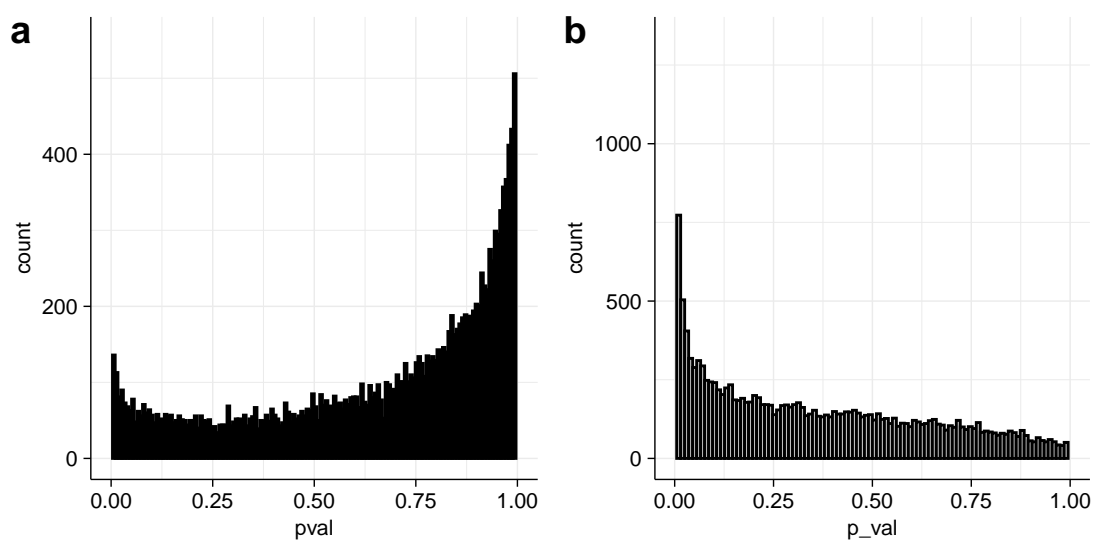


Figure S10: Calibration of obtained NPARC-GP results of phospho-TPP data. Histogram of p -values a) before and b) after empirical calibration.